UNIVERSITY OF ALBERTA
LIBRARY RELEASE FORM

NAME OF AUTHOR:	Norm James Buchanan
TITLE OF THESIS:	Study of a Readout System for a Liquid Argon Calorimeter at ATLAS
DEGREE:	Master of Science
YEAR THE DEGREE GRANTED:	1999

Norm James Buchanan
Department of Physics
University of Alberta
Edmonton, Alberta
T6G 2J1

Date:

University of Alberta

Study of a Readout System for a Liquid Argon Calorimeter at ATLAS

By

Norm James Buchanan

A dissertation

presented to the Faculty of Graduate Studies and Research

in partial fulfilment of the requirements for the degree

of

Master of Science

Department of Physics

Edmonton, Alberta

Spring 1999

UNIVERSITY OF ALBERTA

FACULTY OF GRADUATE STUDIES AND RESEARCH

The undersigned certify that they have read, and recommend to the Faculty of Graduate Studies and Research for acceptance, a thesis entitled "Study of a Read-out System for a Liquid Argon Calorimeter at ATLAS " submitted by Norm James Buchanan in partial fulfilment of the requirements for the degree of Master of Science.

Associate Professor D.M. Gingrich , Supervisor

Professor N. Rodning

Associate Professor D.R. Schmitt

Date:

Assistant Professor D. Elliott

Abstract

A readout system for the liquid argon calorimeter of the ATLAS detector was built and tested at CERN in 1996. This system contained an analog pipeline and was designed to operate in a dual gain mode as well as a single gain mode. Noise, linearity, dynamic range, and electron energy resolution of the system were measured. The total noise introduced by the electronics was found to be approximately 100 MeV to 120 MeV per channel. The nonlinearity of the system was less than 0.3% over a dynamic range of 11.2 bits. The measured electron energy resolution was less than 1.9% for the 100 GeV, 150 GeV, and 200 GeV electrons. The effects of different operating parameters were studied.

Acknowledgements

I would like to foremost thank Dr. Doug Gingrich for his guidance during this research. His comments, suggestions, and encouragement were of invaluable importance.

The enormous tasks of design and construction of the readout boards were carried out by the technicians at the Centre for Subatomic Research at the University of Alberta. I would like to thank Bill Burris, John Hewlett, Lars Holm, and Jan Schaapman for their contributions.

I would especially like to thank Lars Holm for his assistance during data gathering and for his infinite patience in answering all of my detailed hardware questions.

For his efforts during the test period I would like to thank Dr. Jim Pinfold.

I would like to thank the members of my thesis committee, Dr. Doug Gingrich, Dr. Nate Rodning, Dr. Doug Schmitt, and Dr. Duncan Elliott, for their useful comments.

In addition I would like to thank my colleagues for their entertainment and insightful discussions during this research: Philip Kayal, Anthony Faust, Bryan Caron, Rob Davis, Dan MacQueen, and Dawn MacDonald.

Lastly, I would like to thank my parents, Norman and Patricia, for their love and support which to a great degree made this work possible.

Contents

List of Figures

List of Tables

CHAPTER 1

Introduction

In June 1996 the University of Alberta tested an analog readout system for a liquid argon calorimeter at CERN, Geneva. The readout system was a prototype of that planned for use with the ATLAS detector at the Large Hadron Collider in the year 2005, and consisted of 5 readout boards containing analog pipeline storage and an additional board which contained the control circuitry.

The test consisted of two parts: a study of the operation of the electronics, and the measurement of the energy resolution for electrons of 100 GeV, 150 GeV, 200 GeV, and 300 GeV energy. The study of the system involved measuring the electronic noise, both incoherent and coherent. The cross-talk across the system was also approximated. The study also involved measuring the linearity and gain of the system. The energy resolution for electrons was measured and three different methods of estimating the electronics noise term of the energy resolution expansion are presented.

This thesis gives the background to the ATLAS project and describes the prototype calorimeter. The electronics system is described in detail. The results of the test are presented and recommendations for improvements are given.

1.1 Personal Contribution

My personal contribution to the experiment can be categorized into three areas: writing of data acquisition software, supervision of data gathering, and analysis. I wrote a significant portion of the data acquisition software at the University of Alberta prior to the test period, as well as, some during the test as required. I was present and involved for roughly 50% - 60% of the data gathering. Finally, with the exception the histogramming code and one fitting routine, all of the code was written by myself[†].

[†]Some routines used in the analysis were based on the ideas of D.M. Gingrich.

CHAPTER 2

Physics Motivation and Experiment Background

2.1 Physics Motivation

Since the early foundations of science, and physics in particular, the matter that makes up the world in which we live has been one of the primary interests of scientists. Scientific thought on the topic of particle physics has come a long way from that of the ancient Greeks. The ancients realized that matter was divisible down to an extremely small size. It wasn't until this century that scientists began to understand the nature of matter. At the beginning of this century theoretical physicists were developing special relativity and quantum mechanics. The relationship between these two theories as well as some surprising discoveries like the muon led to a theoretical understanding of particle physics. With the development of particle theories has come a myriad of experiments to test these theories. These experiments have either verified the theories or motivated alternative theories. In the year 2005 an accelerator, the Large Hadron Collider (LHC), will provide energies an order of magnitude higher than anything before it and should provide the opportunity to determine whether the current particle theories are accurate descriptions matter, or whether alterations to the theories are required.

2.1.1 The Standard Model

During the 1970's particle physicists began developing a theoretical model, based on quantum fields and symmetries, which described the interactions between the particles which make up our universe. This Standard Model (SM) [1] describes matter in terms of three families of lepton-neutrino pairs (the electron and electron neutrino, muon and muon neutrino, tau and tau neutrino) and similarly three families of quark pairs (up and down, charm and strange, bottom and top). There are three colours of quarks, which combine in colourless groupings to form mesons and hadrons. Each type of lepton, neutrino, and quark is referred to as a "flavour". Along with these fundamental particles exist three force fields and their corresponding mediating particles. The electromagnetic force is an interaction between the charged particles. The electromagnetic interactions are mediated by the photon. The interactions between quarks of different flavours are mediated by three vector (spin 1) bosons, the $W^{\pm}$ and Z^0. These interactions are referred to as "weak" interactions. The third of the force fields is the "strong" field, which mediates the interactions between different quark "colours". Different valence quarks, or quarks which are not quark-antiquark pairs, must combine in such a way as to be colourless. A proton, for example, contains two up quarks and a down quark. Mesons must be in combinations of twos such that any coloured quark is balanced with an "anticolour" quark. The mediator of the strong force is a spin-1 object called the gluon. There is a gluon for each colour combination.

The Large Hadron Collider will provide enough energy to measure the parameters of the SM such as the Higgs boson mass. The high luminosity will provide the opportunity to measure parameters, such as the masses of the $W^{\pm}$ and Z^0 bosons, to greater accuracy. In addition, the LHC will provide the opportunity to study top and bottom quark physics, search for super-symmetric particles, and search for possible

substructure of quarks and leptons. Either evidence of supersymmetry or substructure of quarks and leptons could require modifications to our current understanding.

2.1.2 Higgs Boson

The standard model gives a description of the interactions between matter, but it gives no explanation of the origin of the masses of the particles it describes. The Higgs boson was a theoretical addition to the SM which provides a mechanism to account for these masses. Since the SM provides no particular value for the Higgs mass, it is important to have a detector which can identify the Higgs over a wide range of potential masses and decay channels. The Higgs mass range which will be searched is between 80 GeV, the current upper range of the Large Electron Positron Collider (LEP) [4], and 1 TeV. The following processes will be of interest, as they can be used to examine various Higgs mass sectors [4]:

- $H \rightarrow b\bar{b}$, mass range $80 < m_H < 100$ GeV,
- $H \rightarrow \gamma\gamma$, mass range $90 < m_H < 150$ GeV,
- $H \rightarrow ZZ^* \rightarrow 4\ell^{\pm}$, mass range 130 GeV $< m_H < 2m_Z$,
- $H \rightarrow ZZ \rightarrow 4\ell^{\pm}$ or $2\ell^{\pm}2\nu$, mass range $m_H > 2m_Z$,
- $H \rightarrow WW, ZZ \rightarrow \ell^{\pm}\nu$ 2 j or $2\ell^{\pm}$ 2 j, mass range $m_Z < m_H < 1$ TeV,

where ℓ can be either e or μ, j is a jet, m_Z is the mass of the Z boson (91.2 GeV), b is a bottom quark, ν is a neutrino, and m_H is the predicted mass of the Higgs.

2.1.3 Top Quark Physics

The observation of the top quark at both the CDF (Collider Detector at Fermilab) and D0 experiments at Fermilab National Laboratory [5] have generated great interest in the ability of the LHC to act as a "top factory". The LHC will initially produce more than 6000 $t\bar{t}$ pairs per day [4] (for $m_t = 170$ GeV), even at the luminosity* of 10^{32} $cm^{-2}s^{-1}$. The primary top quark study at the LHC will be the determination the top quark mass, m_t. This will be done by examining various decay channels such as $t \rightarrow jjb$. The large production rate will give approximately 100 decays of the form, $t\bar{t} \rightarrow (\ell\nu b)(jjb)$, per day. Searches for rare top quark decays will also be performed.

2.1.4 B Physics

The B physics studies will include a search for CP-violation through decays such as $B_d^0 \rightarrow J/\psi K_S^0$ and $B_d^0 \rightarrow \mu^+\mu^-$. The experimentally easiest B physics studies will be done when the LHC runs at its initial luminosity of 10^{33} $cm^{-2}s^{-1}$. At this luminosity pile-up effects* will be minimized and the vertex detectors close to the beam-pipe are expected to survive in the intense radioactive environment.

Measurement of $B^0\overline{B^0}$ mixing, searches for rare B decays, and studies of rare B hadrons will also be undertaken. Emphasis will be put on the precise measurement of CP-violation and the determination of the angles in the Cabibbo-Kobayashi-Maskawa unitarity triangle.

*Luminosity is a measure of the number of particles passing a point per second. In a collider where there are N particles per bunch, the bunch interaction point has a cross-sectional area A, and f is the frequency of bunches passing the interaction point, the luminosity is given as $L = N^2f/A$ and has the units of $s^{-1}cm^{-2}$.

*Pile-up refers to signals left by secondary processes during the time that measurements of the primary event are being made.

2.1.5 Beyond the Standard Model

The experimental verification of SM predictions indicate that it is an accurate model at the energies examined (the Tevatron at Fermilab collides protons and anti-protons with a centre-of-mass energy of 2 TeV). There are theoretical speculations however that the SM may be a low energy approximation to a more complete theory. One such theory is symmetry linking the half-integer spin matter fields with the integer spin boson gauge fields [2]. Proposed models fitting this description are the super-symmetric extensions to the standard model [3]. The energy of the Large Hadron Collider will provide the opportunity to look for "heavy" particles such as new massive bosons (Z' and W') which are not predicted by the standard model. Leptoquarks, particles which mediate the transitions between leptons and quarks, could also be discovered, if their mass is within the kinematic limit of the Large Hadron Collider. The discoveries of such particles could confirm theories which provide a more complete description of matter.

Since the SM describes quarks and leptons as point fundamental particles, any non-point-like nature of either particle should manifest itself in terms of deviations from the parameters of the model. The Large Hadron Collider could well provide energies high enough to show these deviations.

2.2 Large Hadron Collider (LHC)

In the year 2005 the LHC will go online producing high luminosity (10^{33} $cm^{-2}s^{-1}$ to 10^{34} $cm^{-2}s^{-1}$) proton on proton collisions with a centre of mass energy of 14 TeV.

The collider will initially operate at the lower luminosity providing an opportunity to study complex signatures such as tau-lepton interactions and heavy flavour

tags from secondary vertices. At the lower luminosity the pile-up noise will be minimal and the vertex detectors close to the beam-pipe will function. The LHC will then be run at the higher luminosity to provide a greater number of signatures of interesting events using electron, muon, jet, missing transverse energy measurements and b-tagging.

The LHC will use the current LEP accelerator tunnel and will contain 4 detectors (Figure 2.1). Two beams of protons in side-by-side rings will be accelerated to 7 TeV in opposite directions and will collide at the four interaction points with a centre of mass energy of 14 TeV. To reach the maximum luminosity of 10^{34} $cm^{-2}s^{-1}$, each of the rings will be filled with 2835 "bunches", or groupings, of 10^{11} protons [6]. The injection system used for the LHC will be an upgraded version of the currently existing accelerator chain. The chain will accelerate the protons to 1.4 GeV, for injection into the LHC [7]. The LHC circumference is 27 km, making it the largest hadron collider ever constructed.

The bunch crossing rate will be one crossing every 25 ns, or 40 MHz, giving a bunch separation of 7.5 m, and a resulting beam current of 0.54 A. At the LHC it is expected that there will be a collision rate of 10-20 collisions per bunch crossing.

A magnetic field of 8.36 T will be required to direct the 7 TeV proton beams around the ring. To achieve this high magnetic field super-conducting magnets will be used.

2.3 A Toroidal LHC Apparatus (ATLAS)

The ATLAS detector (Figure 2.2) is a multi-purpose detector design which will provide data for good event reconstruction at high luminosities. ATLAS will be required

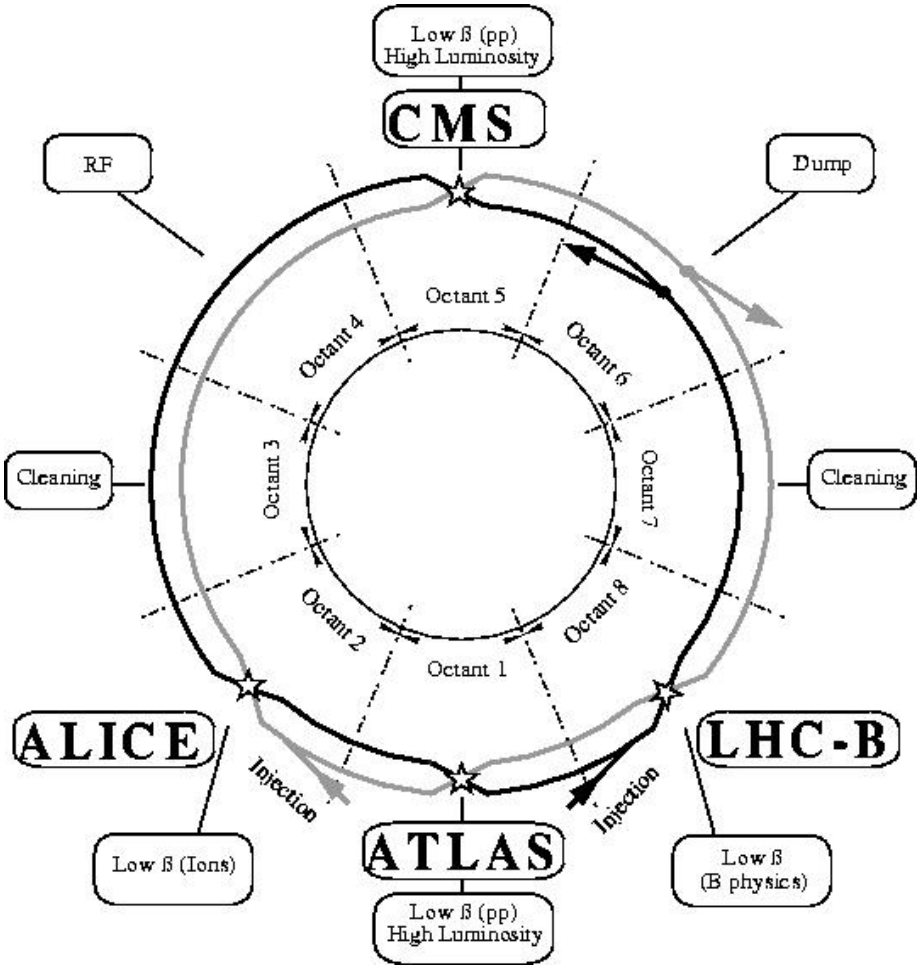

Figure 2.1: Layout of Large Hadron Collider and corresponding detectors.

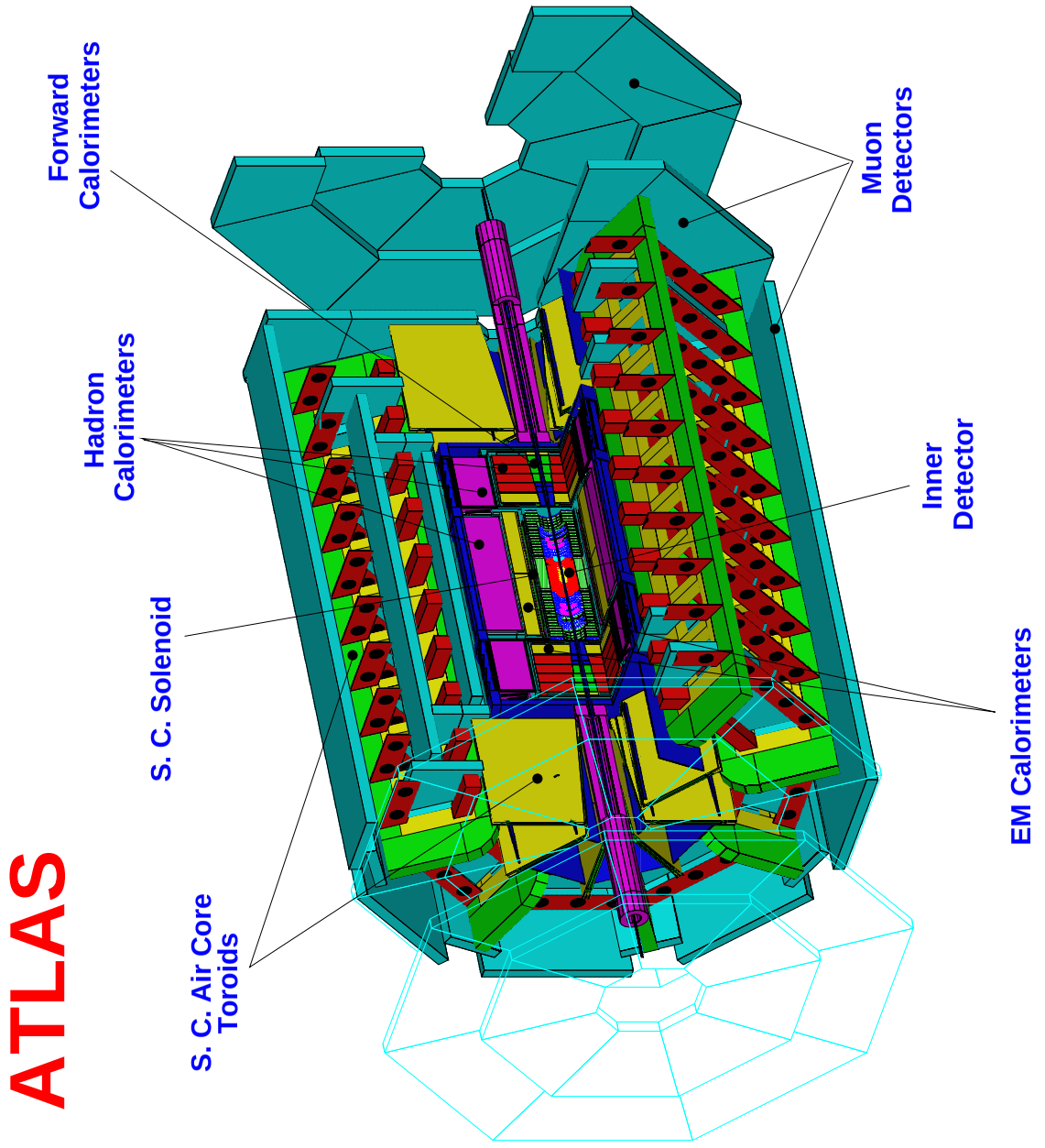

Figure 2.2: The ATLAS detector (taken from the ATLAS Technical Proposal, 1994).

to provide the following [4]: very good electromagnetic calorimetry, which will permit detection of photons and electrons; high multiplicity tracking, with good efficiency for lepton identification and tracking, as well as b-tagging, and heavy-flavour vertex reconstruction; and precise muon momentum measurements. While these requirements are typical of general purpose detectors at collider facilities, ATLAS will have the additional problems associated with the high luminosity and high track multiplicity characteristic of high energy hadron colliders. To achieve the measurement objectives described above, there will be three sub-detector systems: an inner detector containing a Transition Radiation Tracker (TRT), and semiconductor detectors; a calorimeter system made up of electromagnetic and hadronic components; and a muon spectrometer.

2.3.1 Inner Detector

The first portion of the detector that particles will pass through is the inner detector. It is surrounded by a solenoid which provides a magnetic field of 2 T in a direction parallel to the beam pipe, giving curvature in the r-ϕ plane* to charged particles. Because of the high luminosity, and thus high track multiplicity, the inner detector has to have high spatial resolution and survive for 10 years in the high radiation environment near the beam-pipe. The radiation of concern includes neutrons, protons, anti-protons, as well as any long lived particles [8]. The inner detector is comprised of three sub-detector systems, pixel detectors, strip detectors, and the TRT. The pixel and strip detectors make up the precision tracking portion of the detector and extend from the beam pipe ($r = 0.025$ m) to a radius of 60 cm, while the TRT completes the

*The coordinate system used in describing the detector is a typical cylindrical system with the z-axis along the beam-pipe, r-axis pointing radially outward from the beam crossing point, and the ϕ dimension accounting for rotations about the beam-pipe. When events are discussed, the coordinate system which most naturally fits the event geometry is a spherical system in r, θ, and ϕ.

inner detector out to a radius of 80 cm. The coverage in the $r-\eta$ plane is from $\eta = 0$ to $\eta = 2.5$[†]. This region of the inner detector is made up of concentric cylinders for radial measurements, and disks perpendicular to the beam pipe for measurements in the forward directions. The types of materials used for the precision tracking region are determined by cost effectiveness and radiation tolerance. The pixels and strips make up the Semi-Conductor Tracker (SCT), which is designed to resolve tracks at high luminosity and within jets. The TRT is the outermost part of the inner detector and makes many measurements of the track trajectory, and thus gives good track identification. The inner detector was also designed to keep the dead material (non-detecting matter which absorbs the energy of particles) in front of the calorimeter to a minimum.

2.3.2 Calorimetry

The calorimetry in ATLAS (Figure 2.3) needs to survive in an environment of high radiation, as described in the previous section, and be fast enough for first level triggering [4] (described in section 2.3.4). The innermost layer of the calorimeter (electromagnetic barrel, electromagnetic and hadronic endcaps, and forward calorimeters illustrated in Figure 2.3), which extends out to a radius of 2.2 m, will receive radiation in the following amounts: 0.5 kGy/yr (1 Gy = 100 Rad) and 10^{13} n cm^{-2} yr^{-1} in the barrel and 20 kGy/yr and 10^{14} neutrons cm^{-2} yr^{-1} in the endcaps [9]. In order to use calorimetry in this environment, this portion of the calorimeter will use liquid argon (LAr) as active material. The dose rate in the hadronic tile calorimeter is expected

[†]Pseudorapidity, η, is given by the following expression:

$$\eta = -\ln\left(\tan\left(\frac{\theta}{2}\right)\right), \tag{2.1}$$

where θ is the polar angle between the particle direction and the beam-pipe.

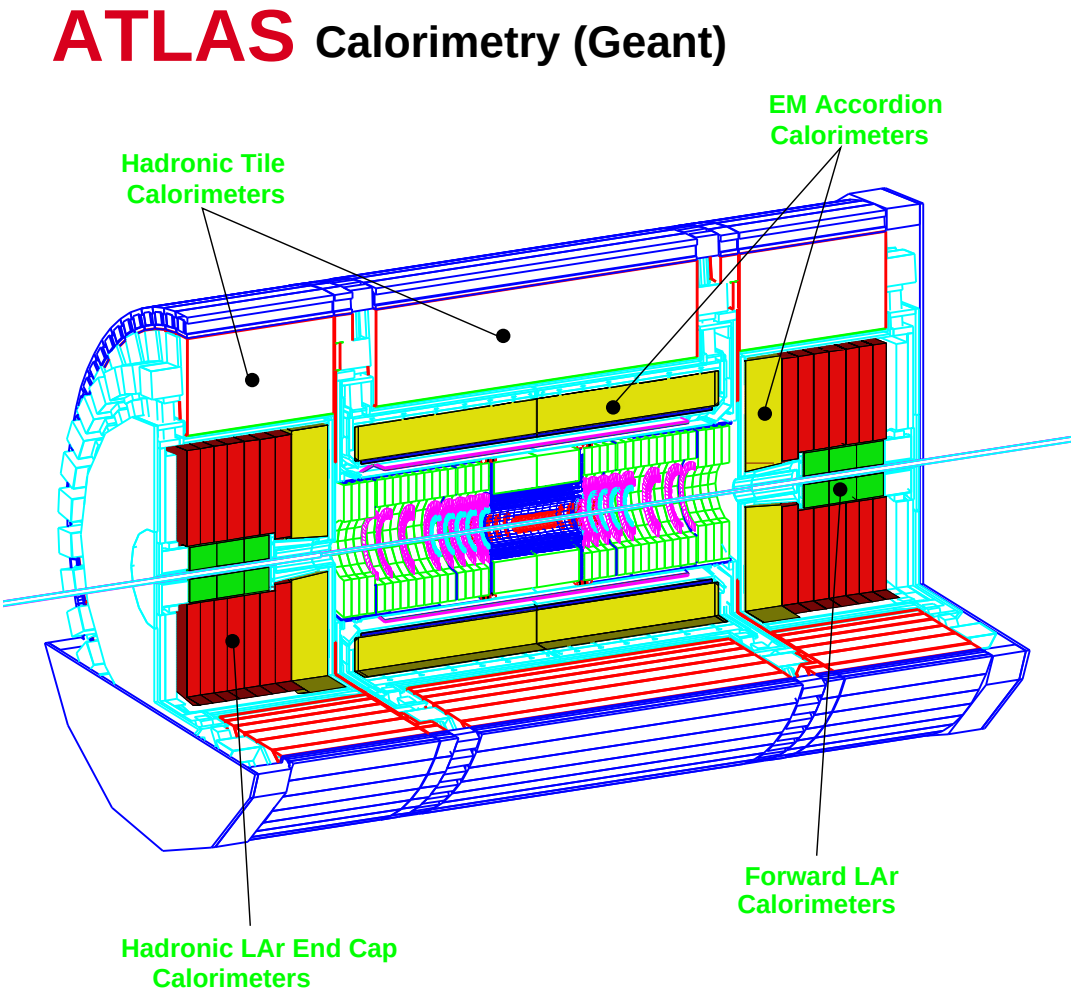

Figure 2.3: ATLAS Calorimetry (taken from the ATLAS Liquid Argon Calorimeter Technical Design Report, 1996). The parenthesized "Geant" refers to the package which rendered the detector.

to be only a maximum of 38 Gy/yr and thus scintillating tiles with steel absorbers and optical fibre link readout will be used.

There will be the potential for pile-up noise due to the long drift time of the ionization electrons in the LAr. The ionization current in LAr has a rise time of the order of 1 ns (as described in section 2.3.5). This rise time will be exploited to counter the slow drift time of approximately 400 ns [10].

The electromagnetic calorimeters will be built using an accordion geometry, as shown in Figure 2.5. The "waves" of the accordion will lie outward from the interaction point along the paths of particles. This will allow towers to be naturally summed along longitudinal slices of the calorimeter, thus limiting the amount of trigger electronics used.

The LAr calorimeter completely surrounds the inner detector and is divided into three main components: an electromagnetic calorimeter (barrel and endcap), a hadronic endcap calorimeter, and a forward calorimeter (Figure 2.3). The electromagnetic calorimeter allows precise energy measurement of radially expanding showers in the barrel (Figure 2.6), and showers expanding in a forward direction in the endcap (Figure 2.7). A presampler is situated on the inside radius of the barrel and in front of the endcap to correct for energy lost before the calorimeter. The hadronic endcap (HEC) consists of two independent wheels (Figure 2.7) at each end of the detector. The first wheel is constructed of 25 mm copper absorbers while the second is made up of 50 mm absorbers. Electrodes in the HEC sit in 8.5 mm gaps between the plates. Each wheel is divided into sections of $\pi/32$ radians in azimuthal angle ϕ. All calorimeters reside in cryostats to maintain the desired operating temperature of 89.3 K [9] for the liquid argon.

The forward calorimeter (FCAL) is designed to work in the high radiation

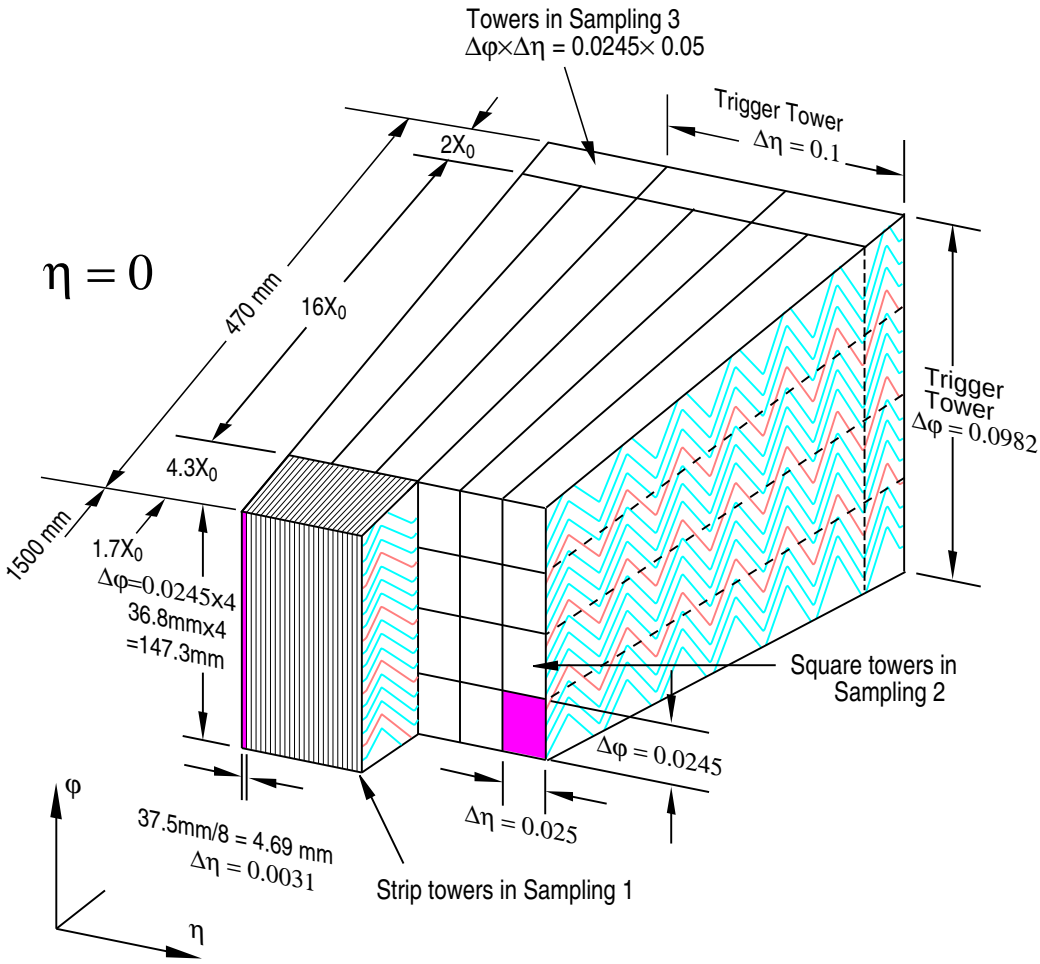

Figure 2.4: Trigger tower of the electromagnetic barrel calorimeter (taken from the ATLAS Calorimeter Performance Technical Design Report, 1996).

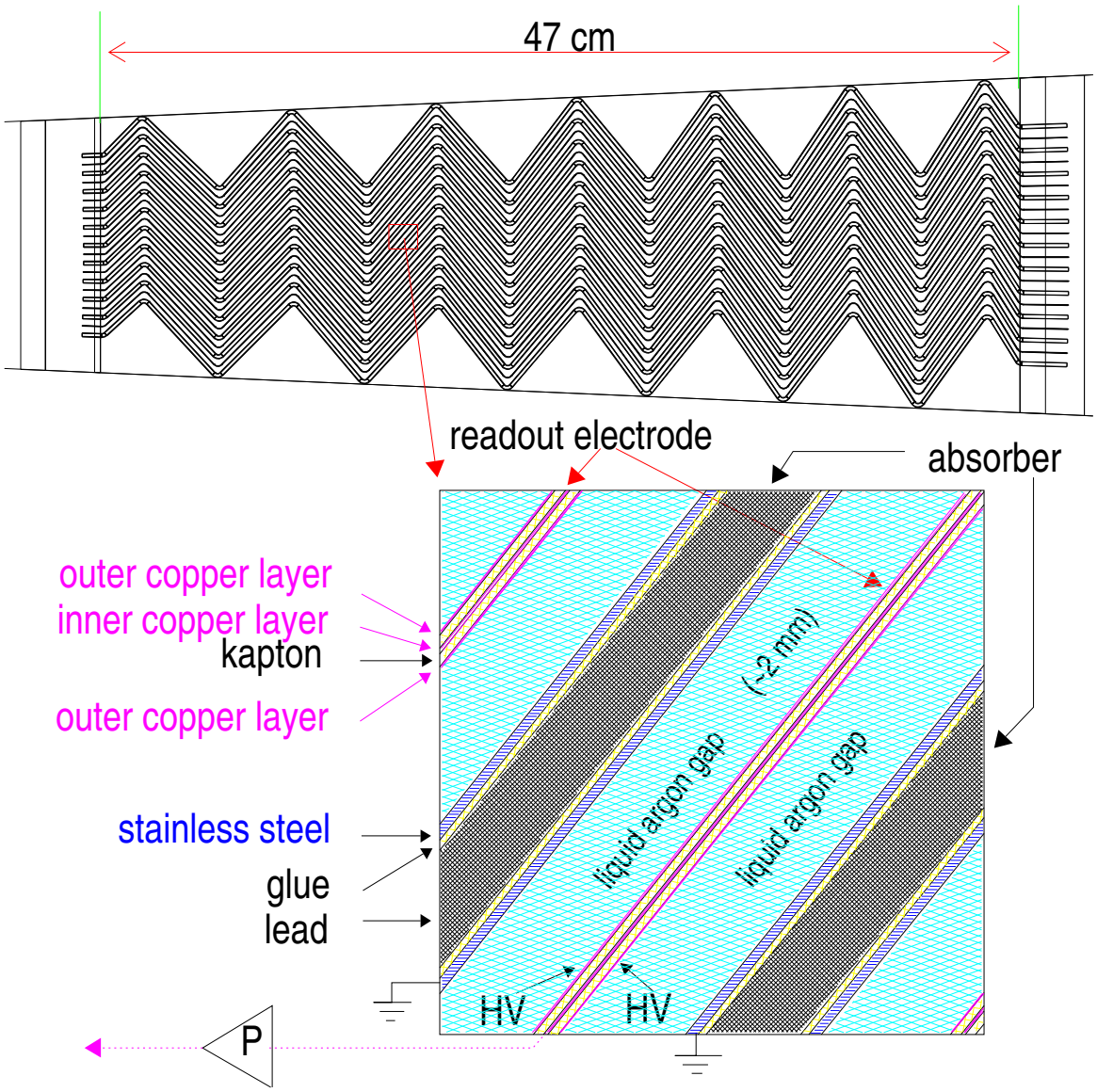

Figure 2.5: The accordion electrode structure (taken from the ATLAS Calorimeter Performance Technical Design Report, 1996).

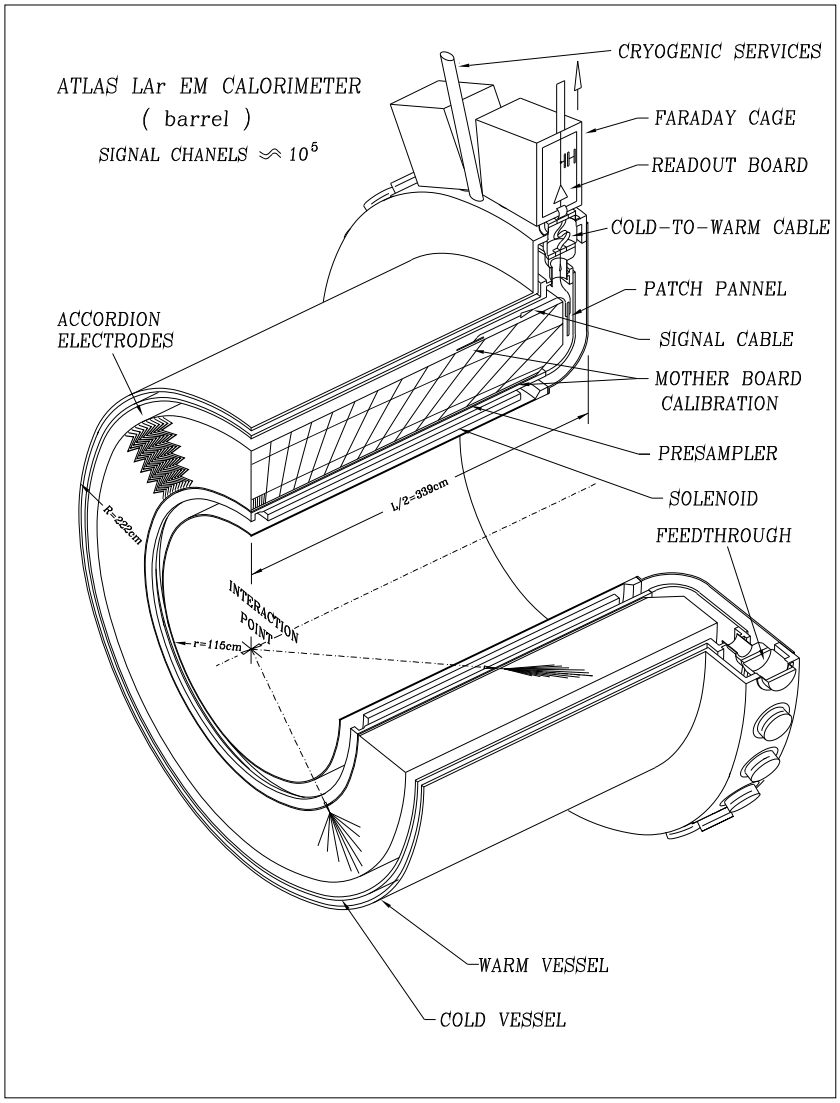

Figure 2.6: Electromagnetic barrel calorimeter (taken from the ATLAS Liquid Argon Calorimeter Technical Design Report, 1996).

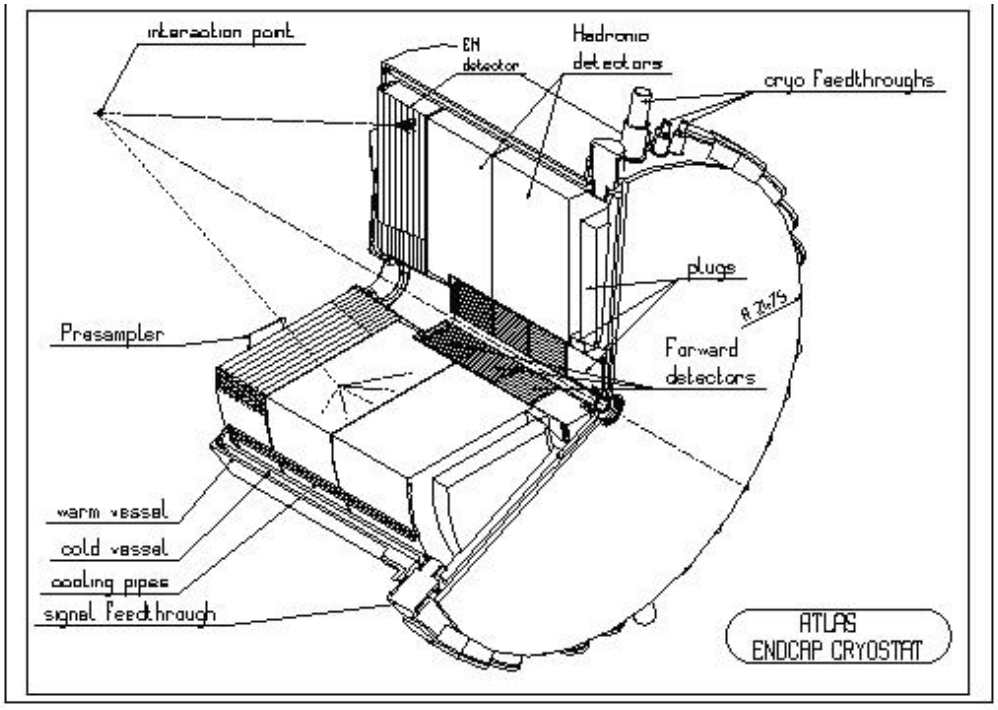

Figure 2.7: Endcap calorimeter (taken from the ATLAS Liquid Argon Calorimeter Technical Design Report, 1996).

region closest to the beam (Figure 2.7). Its front face lies about 4.7 m from the interaction point [9]. The FCAL consists of three sections at each end of the detector, the first made of copper absorber with the remaining two made up of tungsten absorber. Unlike the accordion-shaped electrodes of the electromagnetic calorimeters or the electrodes between layers in the HEC, the FCAL uses rods surrounded by thin tubes placed in a matrix parallel to the beam pipe (Figure 2.8). This geometry prevents positive argon ions from building up in the gap and distorting the signals [4]. This matrix of electrode tubes has a gap size of 250 μm in the first section and 375 μm in the other two.

Outside of the LAr calorimeters (and cryostats) sit the hadronic tile calorimeters (Figure 2.3). These calorimeters are situated such that one hadronic tile barrel lies radially out from the electromagnetic barrel calorimeter and two more hadronic tile barrels (one at each end) lie outside of the endcap calorimeters. The tile calorimeter extends in radius from 2.28 m to 4.23 m. The readout optical fibres run radially, allowing light to be gathered from both open edges of the tiles [11].

2.3.3 Muon Spectrometer

One of the primary requirements of the ATLAS detector is high quality muon momentum measurement [4]. This requirement is because many decay channels, such as $Z' \rightarrow \mu\mu$, need to be searched for above the expected large background. The muon spectrometer is made up of two basic regions, the barrel and the endcap. These surround three super-conducting air core-toroid magnets, one around the barrel and one in each endcap region. These magnets are designed to give a field perpendicular to the r-ϕ plane to allow for momentum measurement.

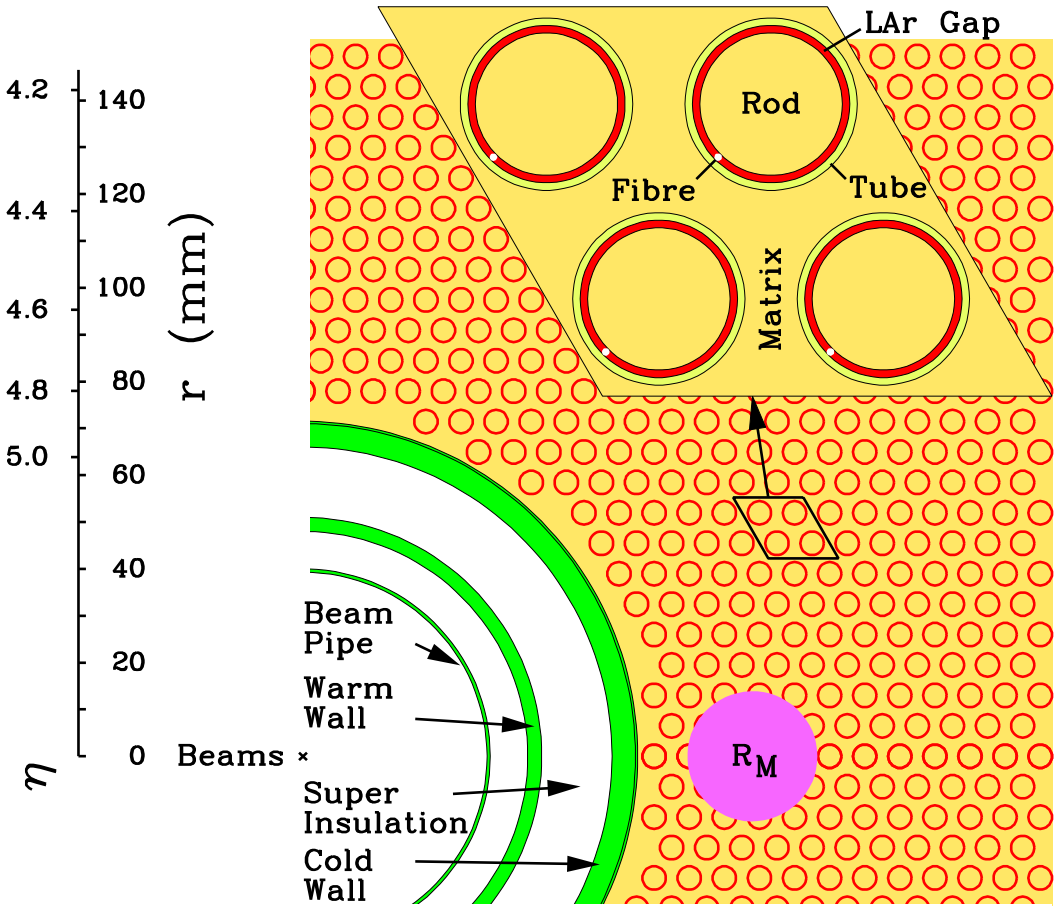

Figure 2.8: FCAL electrode matrix. The circle labelled R_M indicates the Moliere radius for electromagnetic showers (taken from the ATLAS Liquid Argon Calorimeter Technical Design Report, 1996).

The barrel consists of three layers (or stations) of Monitored Drift Tube chambers (MDTs). These stations lie at radii of 4.5 m, 7 m, and 10 m. To ensure continuity in tracking, there is a 200 mm overlap between chambers.

The remaining muon detection system consists of vertical chambers in the endcap and at the transition points where the individual barrel chambers end. Both type of chambers utilize the above mentioned monitored drift tube chambers as well as Cathode Strip Chambers. The combination of the barrel chambers and the vertical chambers ensure precision tracking over the pseudorapidity range of $\eta < 3.0$.

2.3.4 Trigger

An important element of the ATLAS detector is the trigger. A trigger is a device which uses a subset of the event information to determine whether to use further resources for recording the event or reject the event. A trigger usually uses a small separate sub-detector or a portion of the total detector to make this decision. This minimizes the resources required and keeps the trigger time to a minimum. An example of a trigger could be a pair of thin scintillating paddles situated in the beam line several metres in front of a fixed target experiment. The trigger might consist of a coincidence between the tiles within a fixed time which would then initiate readout by the detector. Typically, the trigger can reduce the amount of information stored for off-line analysis. The trigger for ATLAS will be a three level system shown in Figure 2.9. The level 1 (LVL1) trigger acts on a subset of each detection system, with the exception of the inner detector (i.e. calorimeter and muon detector), where the hit multiplicity will be too high to provide useful information for the initial trigger decisions. The LVL1 will be used to locate regions of the detector containing potentially interesting features, such as electromagnetic clusters with high transverse momentum [4]. It

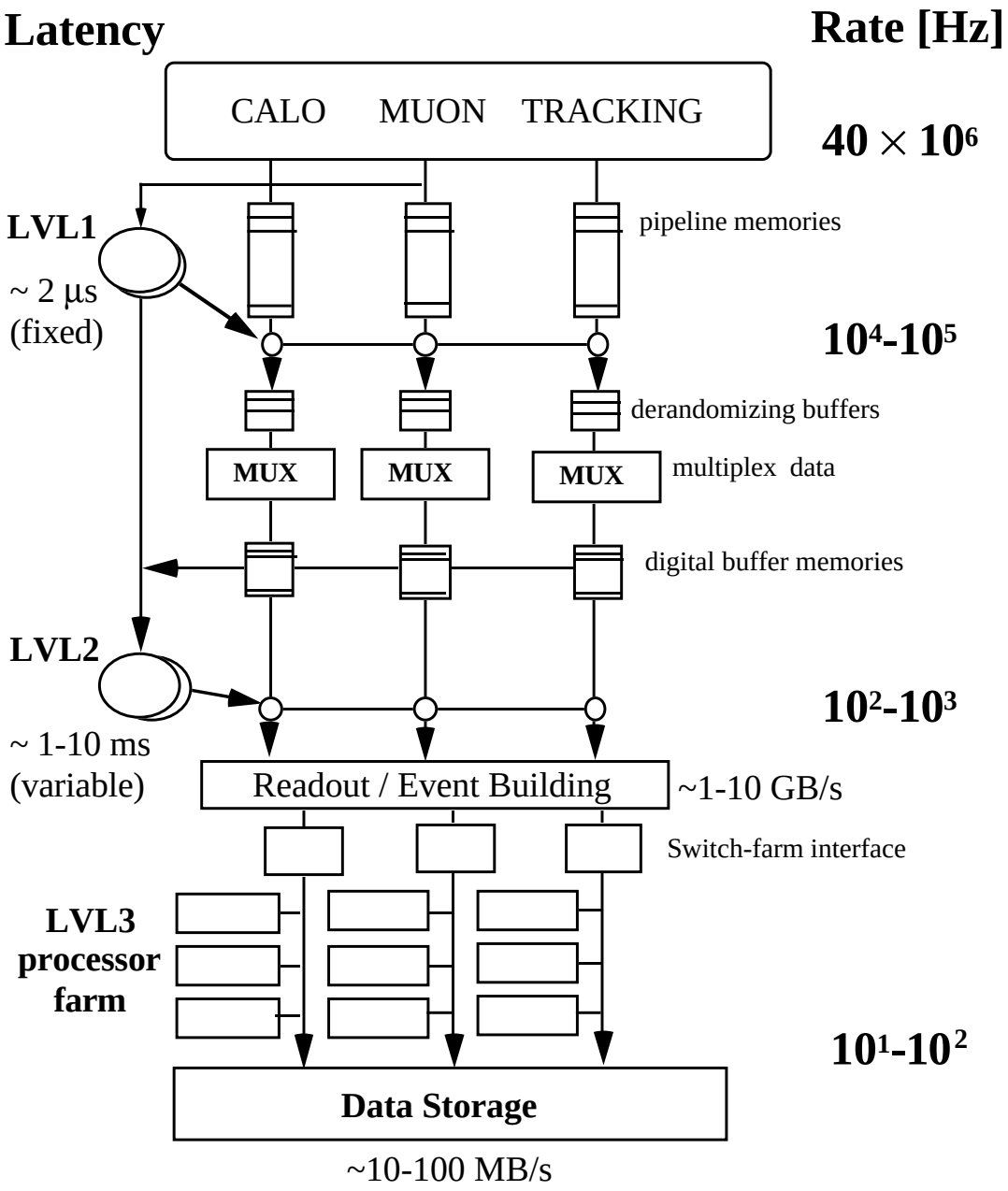

Figure 2.9: ATLAS trigger architecture (taken from the ATLAS Liquid Argon Calorimeter Technical Design Report, 1996).

will process data which comes from segments of the detector which are groupings of smaller segments (i.e. coarse granularity). The LVL1 trigger will accept data at the LHC bunch-crossing rate of 40 MHz, and have a trigger decision time of 2.5 μs. This is the time taken to form the decision using data from the sub-detectors as well as signal transmission time [10]. The calorimeter data is held in analog memories during this period. The output of the LVL1 trigger has a maximum mean rate of 75 kHz. The event acceptance rate of the LVL2 trigger is between 0.1 kHz and 1 kHz with a variable latency of 1 ms to 10 ms. All detector subsystems, including the inner detector, will be used in the LVL2 trigger decisions (using finer granularity data), which is also made on tracking and p_T measurements. Events selected by the LVL2 trigger are sent through an event builder to a farm of processors. These processors make up the level three trigger (LVL3) which reconstructs events at a rate of 1 s to 10 s. The LVL3 trigger will use more complicated reconstruction algorithms, similar to those used off-line, to make selection decisions. After events are selected by the LVL3 trigger, they will be recorded for further detailed analysis.

2.3.5 Liquid Argon Calorimeter Electronics

The LAr calorimeter of ATLAS requires the careful time synchronization of approximately 190,000 high speed readout channels of large dynamic range. There will be 110,208 channels for the electromagnetic barrel, 63,744 for the electromagnetic endcap, 4,416 for the hadronic endcap, and 11,288 for the forward calorimeter, for 189,656 total read-out channels. The energy deposited in a particular calorimeter cell can be as high as approximately 3 TeV [13]. At low energy (just above pile-up and electronic noise – which is estimated to be 50 MeV), energy measurements need to be made. Since 3 TeV divided by 50 MeV is 60,000, a dynamic range of at least 16 bit (65,536)

is required to cover the range. The readout system will sample the analog signals at the beam crossing rate of 40 MHz.

The read-out electronics for the LAr calorimeters can be grouped into two main categories, on-detector and off-detector, which can be seen in Figure 2.10. The off-detector calorimeter electronics consists of the trigger electronics as well as electronics for processing the data after it has been selected by the trigger and digitized. The off-detector electronics is not relevant to these studies and will not be discussed further. The on-detector electronics consists of the calibration electronics, front-end boards, the tower builder (a circuit for summing the data for a trigger tower), and the control hardware described below.

2.3.6 Calibration System

To take full advantage of the stable and uniform ionization signal of the LAr [9], the electronics chain must be precisely calibrated. The constant term in the energy resolution expansion (described in section 5.1), is partly due to the non-ideal calibration of the electronics, such as the nonuniformity of the calibration pulse shape, and thus the calibration must be as precise as possible. The proposed ATLAS LAr calorimeter system requires uniformity to 0.25% in a slice of $\Delta\eta = 0.2$ [9].

The calibration pulses, which closely resemble the actual ionization pulses, are driven onto the actual electrodes, through a current injection resistor*†. As the impedance of the cables can cause non-uniform calibration pulses, the pulsers are located near to the cryostat feedthroughs‡.

*The exception to this is the FCAL where radiation levels are too high to permit the procedure. For the FCAL, the calibration pulses are injected just prior to the preamplifiers.

†A current injector resistor is a resistor across which a potential is placed to induce a current in a circuit.

‡Cryostat feedthroughs are places in the cryostat wall which allow the passage of cables from

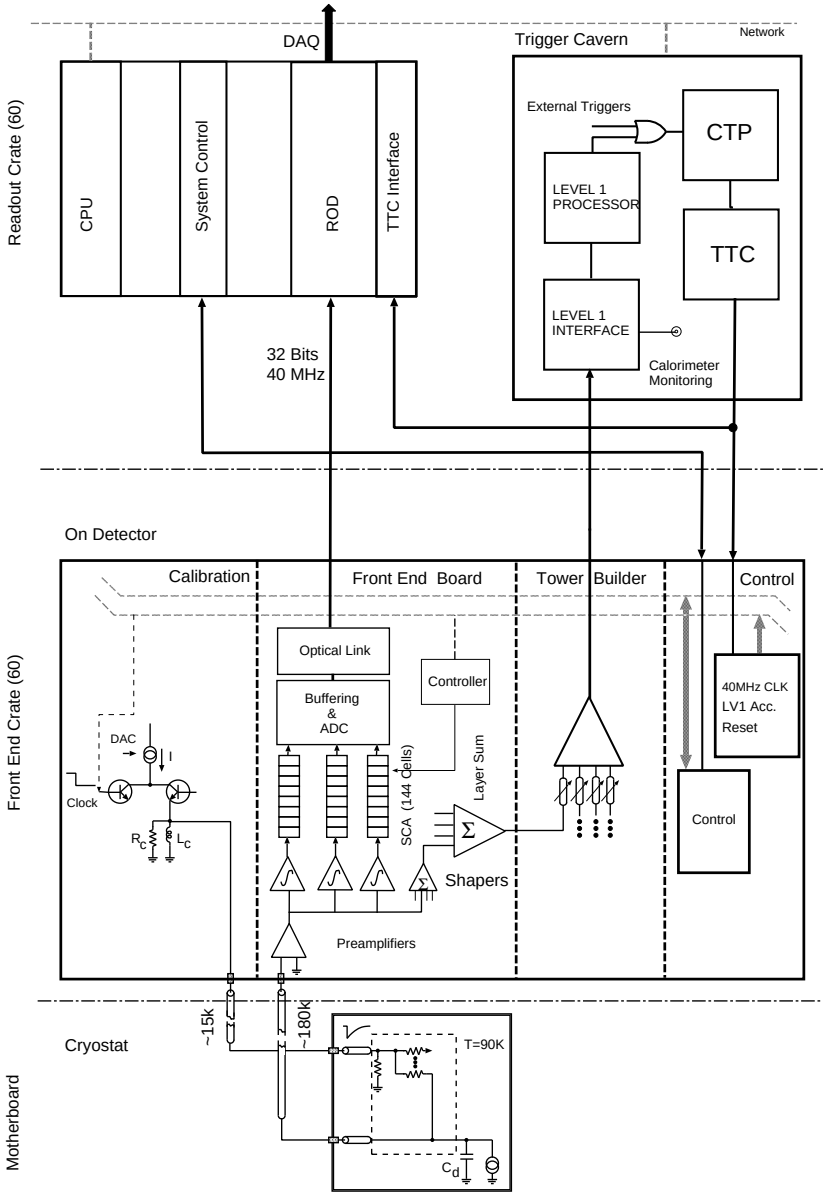

Figure 2.10: Block diagram of the read-out electronics (taken from the ATLAS Liquid Argon Calorimeter Technical Design Report, 1996).

There are four types of calibration procedures for the LAr calorimeter at ATLAS. The first is a pedestal stage, with no signal, allowing the noise to be estimated. The second is a debugging stage for detecting non-responding cells using the pulser. Pulse shape calibration is the third procedure where the shape of the pulse is occasionally examined (this will likely be done prior to the running of the LHC). Finally is a standard calibration procedure where the gain and linearity of the electronics chain is monitored. The calibration procedures will take approximately one minute to complete and will be carried out a few times per day [9].

2.3.7 Front-End Electronics System

The front-end electronics system will amplify, shape, store, and digitize the signals. This electronics chain is shown in Figure 2.11 and explained below.

Preamplifiers

The first stage of the analog signal processing is the preamplification. There will be two types of preamplifier technologies used in the LAr calorimeters, gallium arsenide (GaAs FET - Field Effect Transistor) preamplifiers operating in the cold and preamplifiers using bipolar transistors operating outside of the cryostat. The GaAs preamplifiers will be used for the hadronic endcap. The silicon preamplifiers will be located outside of the cryostat in the crate containing the front-end electronics, for the electromagnetic barrel, electromagnetic endcap, and forward calorimeters. Since the cold preamplifiers will be located right at the electrodes, the signal will not be noticibly degraded prior to amplification. The warm preamplifiers located on the front-end boards will be connected to the calorimeter electronics by transmission

warm to cold or cold to warm.

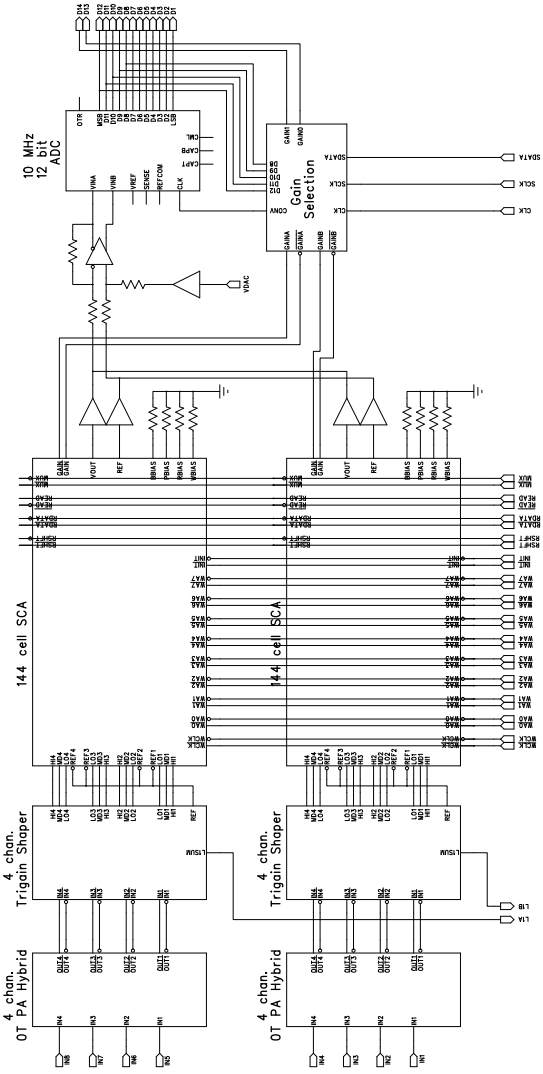

Figure 2.11: Depiction of 8 channels of the analog read-out chain (taken from the ATLAS Liquid Argon Calorimeter Technical Design Report, 1996). Note that the devices immediately following the SCA chips are implied tri-state devices.

lines that maintain signal integrity (shape) before the first stage of amplification [14]. The choice for warm preamplifiers located off of the detector was motivated by the fact that the space on the detector will be limited as well as limitations on the amount of heat which can be generated on the detector. For the hadronic endcap, where mechanical structure forced the mounting of preamplifiers on the outer radial edge of the wheel, the radiation levels will be manageable. Because the electronics will be located in crates in the crack between the barrel and endcap tile calorimeter, there will be minimal dead material introduced in front of the calorimeter.

Shapers

Once a signal is produced within the calorimeter it is favourable to reshape this signal into a form which is better to work with. The calorimeter of ATLAS will have ionization pulses, from a particle traversing the active liquid argon material, with a rise time of approximately 1 ns. The pulse is a triangle which decays linearly to zero (Figure 2.12). These "triangle" pulses will require shaping.

The total measured noise of the system is the quadratic sum of the electronics noise and the pile-up noise. The function of the shaping amplifiers is to reduce the pile-up contribution to the noise. The electronics noise decreases with slower shaping time while the pile-up noise increases with slower shaping time [15] as shown in Figure 2.13 for the electromagnetic barrel and endcap calorimeters. The intersection of the electronics noise and pile-up noise curves gives the shaping time for the minimum of the total noise. The shaping time (shaper internal time constant τ=RC of the shaping amplifier), corresponding to this minimum is around 15 ns for the electromagnetic barrel. This corresponds to a peaking time of 30 ns to 45 ns depending on the calorimeter depth [9]. The shaper uses a CR$(RC)^2$ filter to shape the pulse,

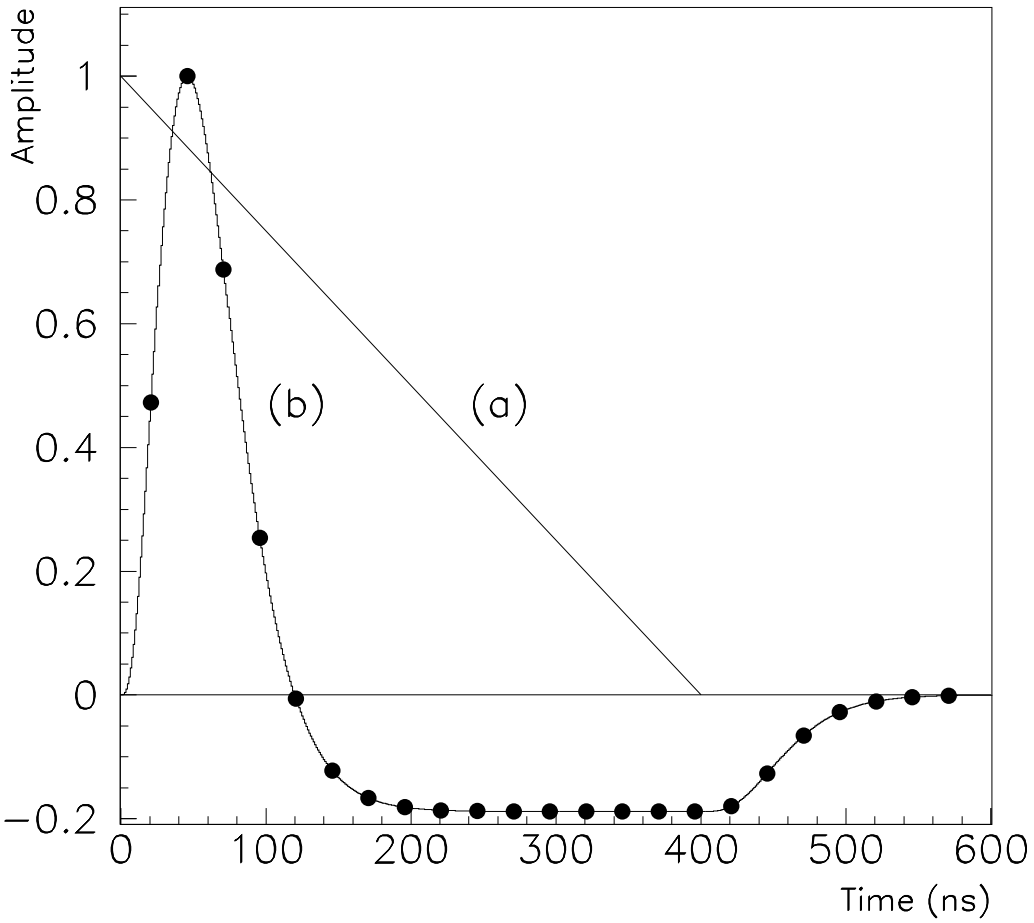

Figure 2.12: The drift current of the calorimeter (a) and the bi-polar shaper response (b) to this current. The dots represent beam crossings (taken from the ATLAS Technical Proposal, 1994).

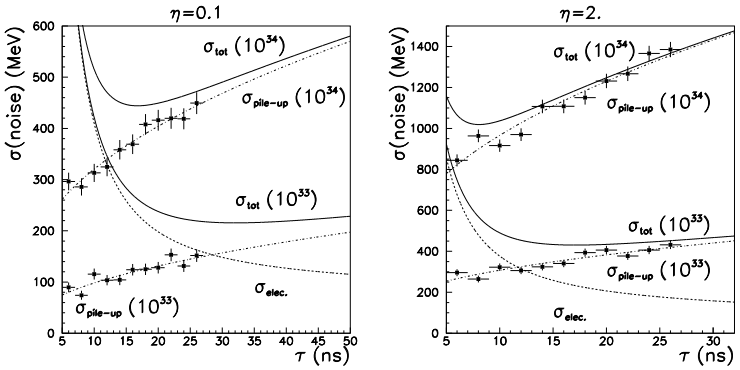

Figure 2.13: The quadratic sum of electronics noise and pile-up noise for the electromagnetic barrel ($\eta = 0.1$) and endcap ($\eta = 2.0$) as a function of shaping time. The luminosity is given in brackets (taken from the ATLAS Liquid Argon Calorimeter Technical Design Report, 1996).

which is two stages of integration (RC) and one stage of differentiation (CR). The result of the shaping is shown in Figure 2.12 along with the triangle pulse of the LAr ionization. There will be roughly 20 beam crossings in the time it takes to shape the ionization pulse, which demonstrates the reason for an increase in pile-up noise with slower shaping.

The other function of the shaper amplifiers is to apply three gains to the signal prior to sending it to the analog pipeline, as illustrated in Figure 2.11. The reason for multiple gains, is that the entire 16-bit dynamic range can be digitized using 12-bit ADCs. The amplifications will be 1, 10, and 100, where the gain selected will be determined after digitization. Each shaper chip will contain 4 shapers and process 4 calorimeter channels, as will the preamplifiers. The analog memories, will now be described.

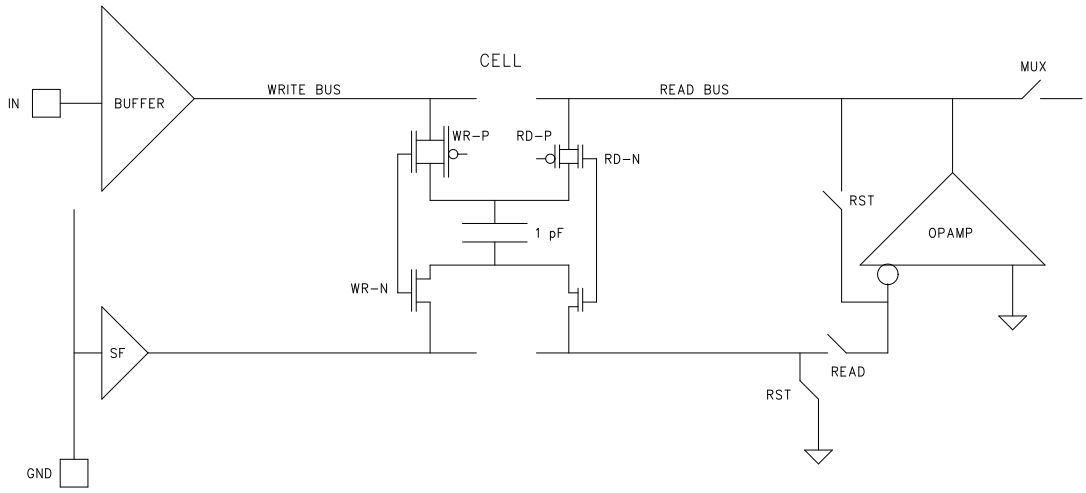

Figure 2.14: Schematic of one analog memory cell (taken from the ATLAS Liquid Argon Calorimeter Technical Design Report, 1996).

Analog Pipeline Memories

The most interesting feature of the front-end readout electronics chain is the analog pipeline memories based on a Switched Capacitor Array (SCA) design [12]. Each pipeline (one for every readout channel) will contain 144 cells where a cell is shown in Figure 2.14. Each cell consists of a 1 pF capacitor and two switches. The write switches (WR-P,WR-N) connect the input signal across the capacitor during charging (writing) and the read switches (RD-P,RD-N) connect the capacitor across the operational amplifier during discharging (reading). The SCA is a random access memory since the read and write busses are separate (a write is independent of a read) and thus access time for any address* is equivalent. The read and write addresses will be generated by a separate SCA controller chip. This controller chip will also interface

*An address is any capacitor, with switches, in the analog pipeline, i.e. there will be 144 addresses.

with the LVL1 trigger. Once the data has been stored in the analog pipelines the capacitors containing the event will either be discharged and recharged with new data or read for digitization if the event is selected by the trigger.

Analog to Digital Conversion and Gain Selection

The gain selection will be made prior to digitization of all of the samples, thus reducing the amount of data to be digitized. The gain selection algorithm will work as follows. The peak voltage of the middle gain setting is digitized. A gain selection chip (as shown in Figure 2.11) then examines 5-bits of the ADC and determines the optimal gain selection for that channel. While this algorithm requires the digitization of the event as well as the original pulse maximum, it avoids analog comparators [9]. The ADCs will have a dynamic (voltage) range of at least 12-bits and multiplexing will be used to reduce cost. The time required to read out an event will be 9.45 μs, giving a maximum digitization rate of 105.8 kHz which is above the allowable LVL1 average trigger rate of 75 kHz. Considering these rates and an analog pipeline buffer size of 7 events, the dead-time will be approximately 0.5% [9]. The signals will be sent, via optical links, to the readout drivers (RODs), some distance away.

2.3.8 Additional On-Detector Electronics

The on-detector front-end crate will house, in addition to the front-end boards previously described, the calibration boards, the tower builder boards, and the control hardware. The front-end crate will act as a Faraday cage, to shield against electromagnetic radiation and reduce coherent noise. These crates will be mounted on pedestals connected to the cryostat as shown in Figure 2.15.

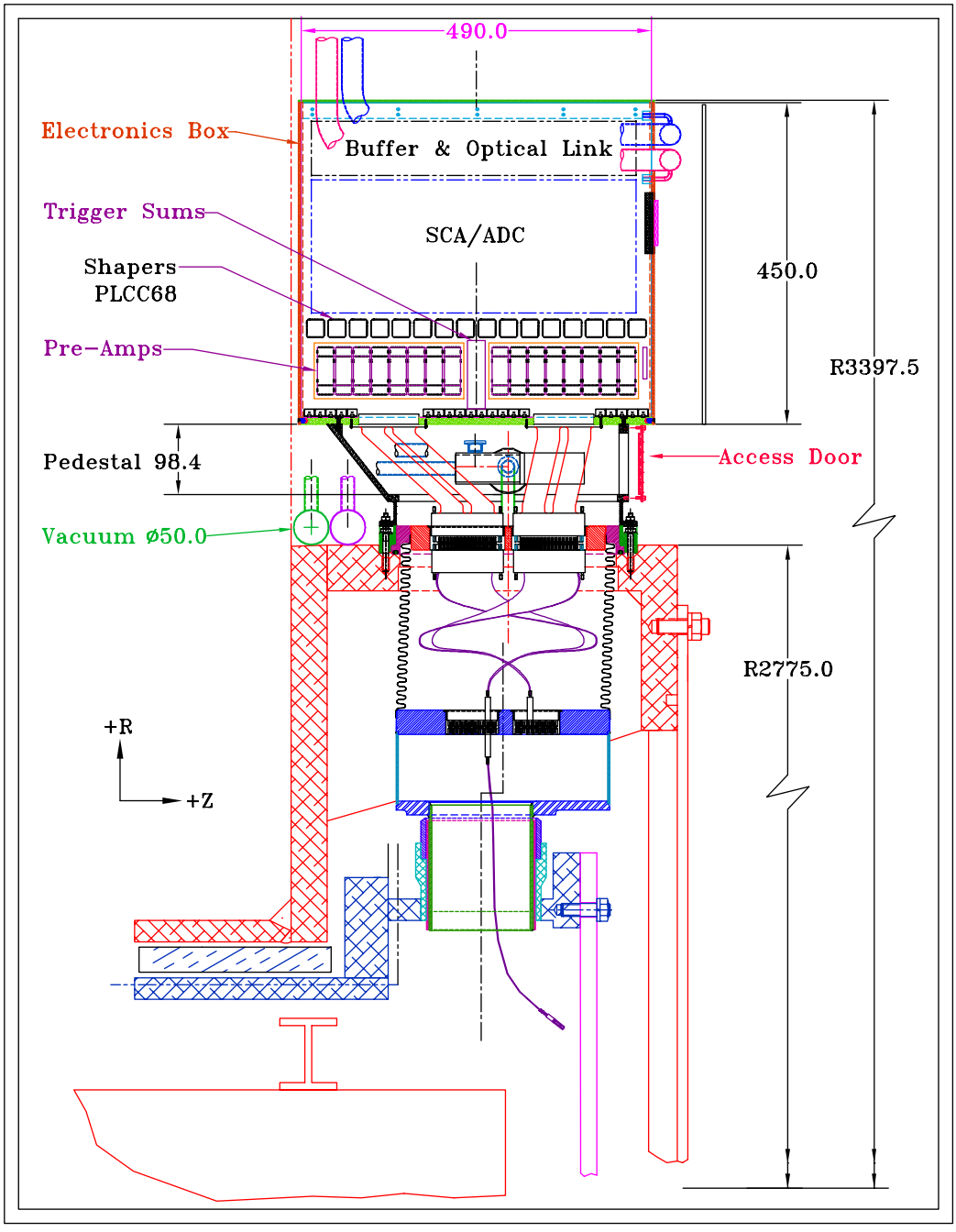

Figure 2.15: Side view of an electronics crate mounted on the pedestal connecting the crate to the cryostat (taken from the ATLAS Liquid Argon Calorimeter Technical Design Report, 1996).

CHAPTER 3

Description of the 1996 Alberta Readout System

3.1 Introduction

In June of 1996, the University of Alberta tested a prototype readout system. The system consisted of front-end boards (FEBs) containing switched capacitor array (SCA) chips developed at LBL [12]. The system was tested on a calorimeter in the H8 beam line of the CERN Super Proton Synchrotron. Five readout boards and one controller board* were tested. Each readout board contained two SCA chips and analog to digital conversion circuitry. The beam consisted of electrons with energies ranging from 100 to 300 GeV with runs taken at 100, 150, 200, and 300 GeV†. The goals of the test were to measure the noise, dynamic range, linearity, and energy resolution of the readout system.

3.2 RD3 Calorimeter

The RD3 calorimeter, a prototype of the ATLAS electromagnetic barrel, was used for the test (Figure 3.1). It was a LAr sampling calorimeter utilizing an "accordion" geometry. The calorimeter consisted of 73 stacked accordion-shaped converter plates

*For the actual ATLAS detector, the controller hardware will be on chips on the FEB.

†Originally, it was planned to take data at 50 GeV, but due to operational error the actual beam energy was not changed during periods where this data was taken. 100 GeV data was taken in place of the 50 GeV data.

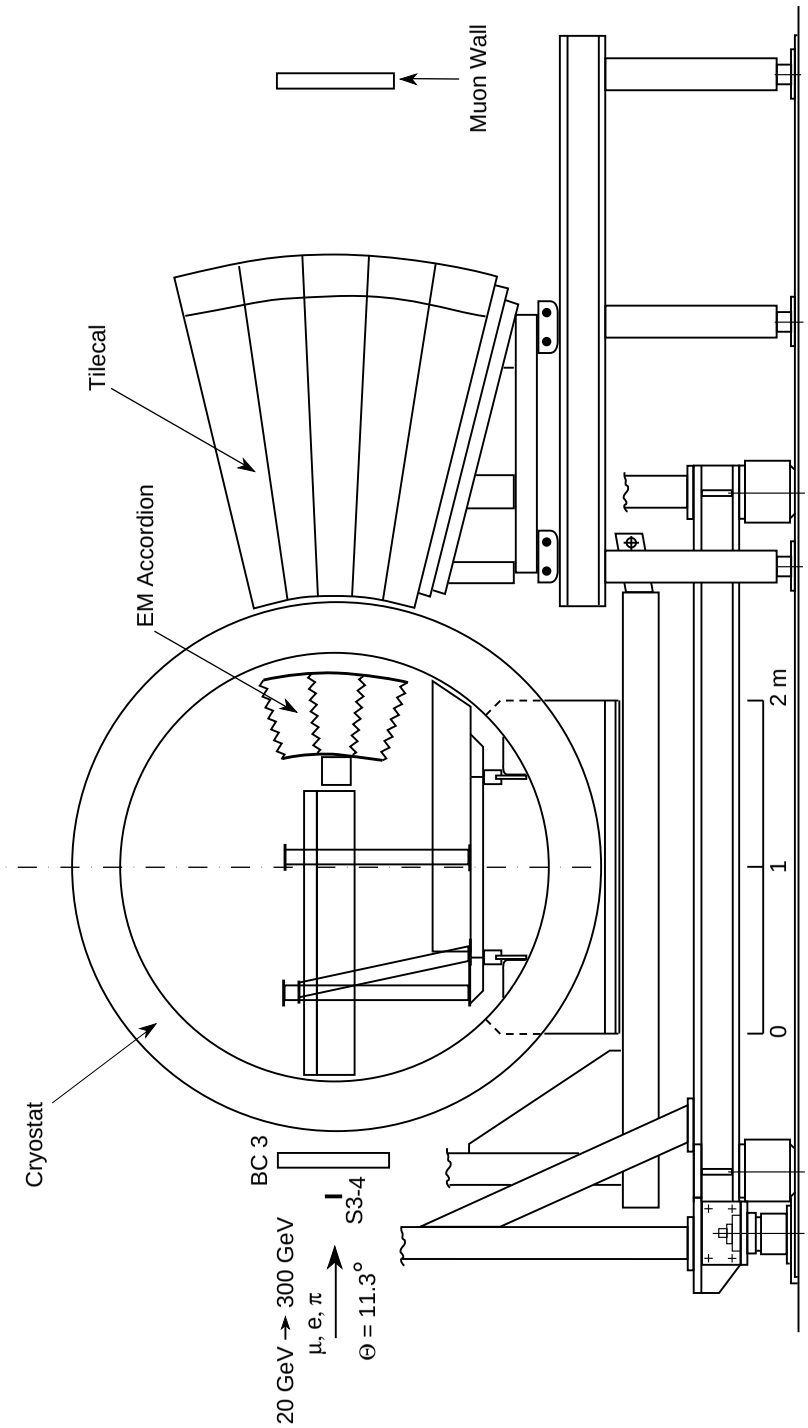

Figure 3.1: RD3 calorimeter set-up for the 1996 tests.

interleaved with 72 readout electrodes of the same geometry [9]. The absorbers were 1.8 mm thick lead plates for pseudo-rapidity less than 0.7 and 1.2 mm thick plates for pseudo-rapidity greater than 0.7. These were sandwiched between 0.2 mm thick sheets of stainless steel. The electrodes were made up of 0.3 mm multilayer copper-kapton boards, which were separated from the absorber plates by a 1.9 mm liquid argon gap. The calorimeter was a cylindrical sector with an acceptance of roughly 3% of the planned electromagnetic barrel calorimeter for the ATLAS detector [16]. The prototype calorimeter extended 2 m along the z axis, covering a pseudo-rapidity range from 0 to 1.08, and 27 degrees in ϕ.

The calorimeter was divided into three radial regions, front, middle, and back, which had thicknesses of 9, 9, and 7 radiation lengths* respectively. The granularity of the front and middle regions were $\Delta\phi \times \Delta\eta = 0.020 \times 0.018$ while the back region was twice as coarse in η with $\Delta\eta = 0.036$. The entire calorimeter was then immersed in a cryostat which was filled with liquid argon and had feedthroughs for the signal wires.

The calorimeter electrodes were operated at a high voltage of 2 kV which produced an electric field of 10 kV/cm across the gap [9]. The electronics noise from inside the calorimeter (mainly from the preamplifiers) was measured to be between 40 MeV and 70 MeV per channel depending on the radial layer and pseudo-rapidity [16].

The trigger used in the RD3 test consisted of scintillating paddles in the beam line in front of the calorimeter. A coincidence between these paddles would signify an event.

*A radiation length is the mean distance over which a high-energy electron loses all but 1/e of its energy by bremsstrahlung.

3.2.1 Calorimeter Electronics

The preamplifiers used on the calorimeter were GaAs based FETs located on motherboards attached to the cryostat electrodes. After passing through the preamplifiers, the signals were sent through bi-gain shaping amplifiers ($CRRC^2$) which filtered them to obtain the desired bi-polar pulse [16]. The peaking time (the time for the pulse to rise from 10% to 90%) of the shaping amplifier was approximately 35 ns for the triangle pulse coming from the calorimeter. The preamplifiers were connected to the shapers by a 50 Ω transmission line. A track and hold circuit followed the shapers and was used in conjunction with the trigger to ensure the signals were sampled as close to the peak as possible.

There were two regions of the calorimeter used for the tests. Each region was equipped with different shaping amplifiers. In one region (bi-gain), used for the majority of the data taking, the signal was split in two and a gain of 10 applied to one of the branches. For the other region (mono-gain) used during the test period no splitting of the signal or additional gain was applied at the shaping stage. For the bi-gain system 60 calorimeter cells were used, 24 in the front layer, 24 in the middle layer, and 12 in the back. Each calorimeter cell was "mapped" to, or connected to, one of the two electronics branches of different gain. For the mono-gain system, 120 cells in a different region of the calorimeter with different preamplifiers and shapers, were used. Each layer contained twice as may cells relative to the bi-gain system. For this system each calorimeter cell corresponded to a single electronics channel.

A voltage driven calibration system was used to simulate the detector signal. The pulses were then distributed onto the preamplifiers, through 2 kΩ injection resistors, which resided on motherboards attached to the calorimeter [17]. With the fast shaping, and the fact that the detector capacitance was quite high ($C_d \simeq 400$ pF),

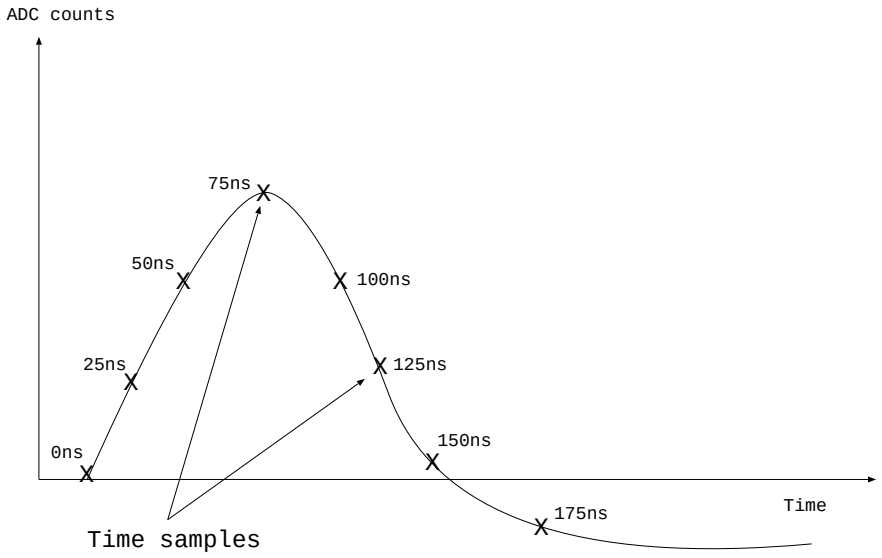

Figure 3.2: Pulse sampling (taken every 25ns).

the parallel noise from the calibration signals passing through the resistors onto the calorimeter was less than 5% of the series noise from the preamplifiers [18]. The pulse (up to 5 V) from the calibration pulsers was designed such that it could drive up to 50 Ω load with a rise time of less than 1 ns and an exponential decay of 400 ns, thus simulating the pulses coming from the calorimeter.

3.3 Analog Pipeline Structure

The decision was made to use an analog pipeline (refer to section 2.3.5) , based on switched capacitor technology, to store the data awaiting a first level trigger decision. After the data was passed from the shaper amplifiers it was written to the SCAs. The data pulses were continuously time sampled and stored in the pipeline. Each pulse consisted of 8 time samples as illustrated in Figure 3.2. The determination of

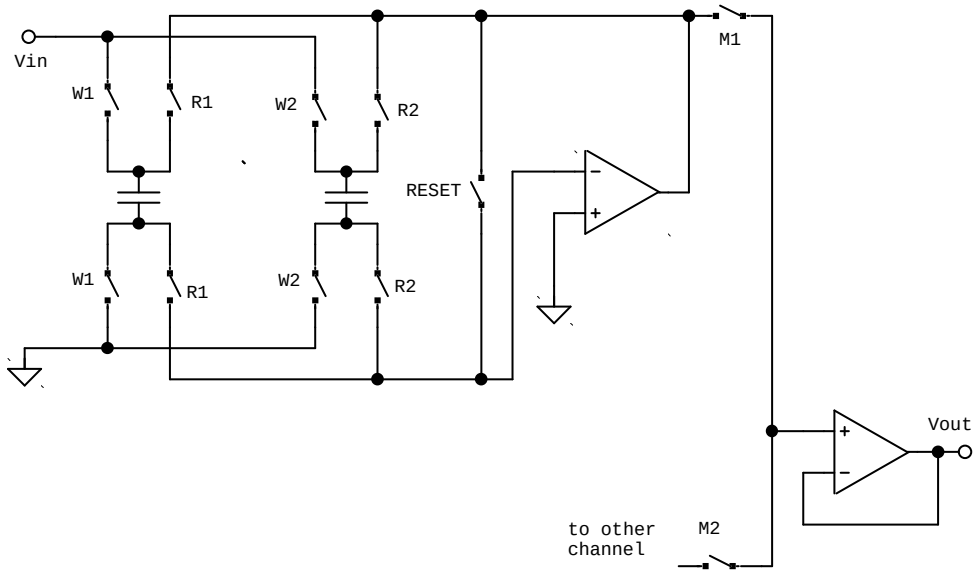

Figure 3.3: Block diagram of an SCA pipeline segment. This diagram shows two cells of same type as in figure 2.14.

the beginning of a pulse was made using a trigger in the beam-line. The trigger is described in section 3.4.

An SCA pipeline, consisted of an array of 256 cells, each of which included a capacitor and a read and write switch (Figure 3.3). The pipeline could hold 32 events (Figure 3.4). Data was continuously written to the pipeline in a circular manner, i.e. after the last cell, the 256th, was charged up, the 1st would be charged again. The exception to this was that if an address was in a state awaiting reading (after a trigger decision) it would be skipped over rather than overwritten.

Each SCA chip contained 16 pipelines (channels), where 12 were used for data and 4 were used for reference subtraction. All of the channels received data simultaneously, in the same address, or capacitor, in each channel. For example, an event written in capacitors 100 to 107 would be written in all sixty channels (12

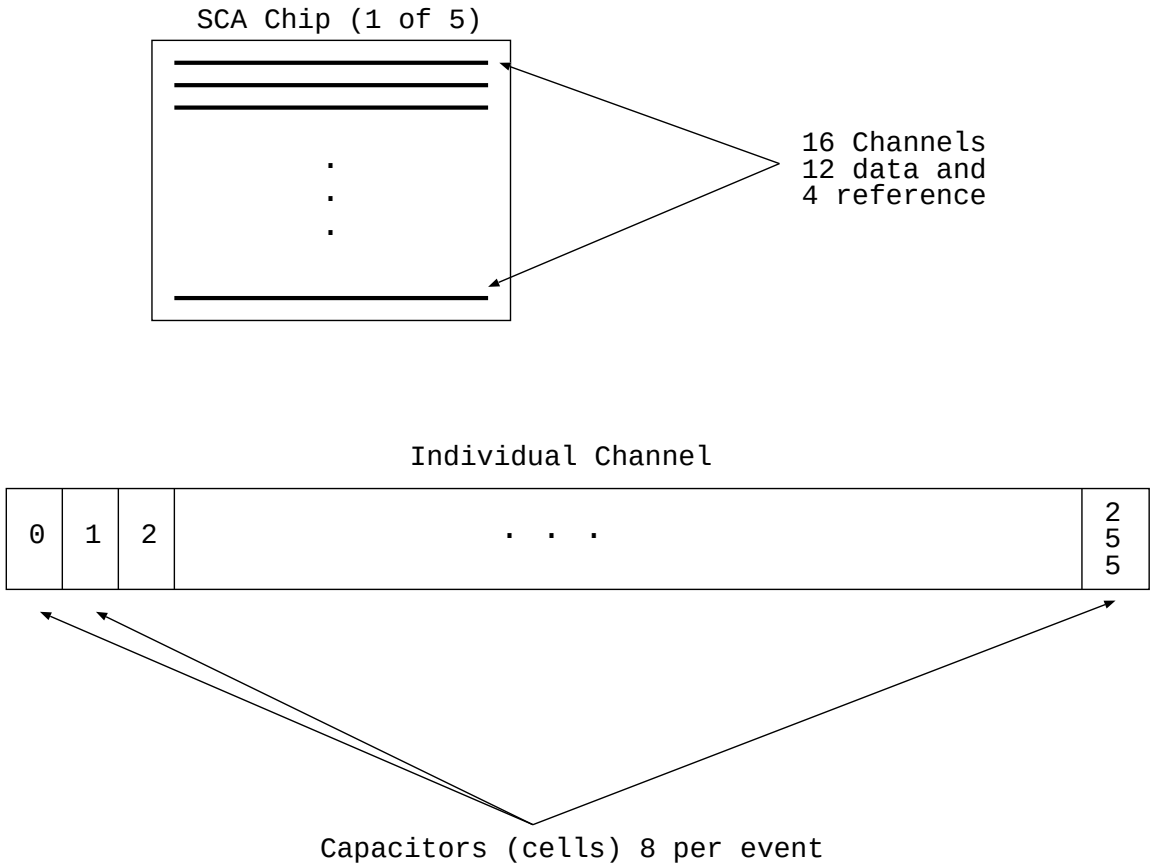

Figure 3.4: SCA chip and channel structure.

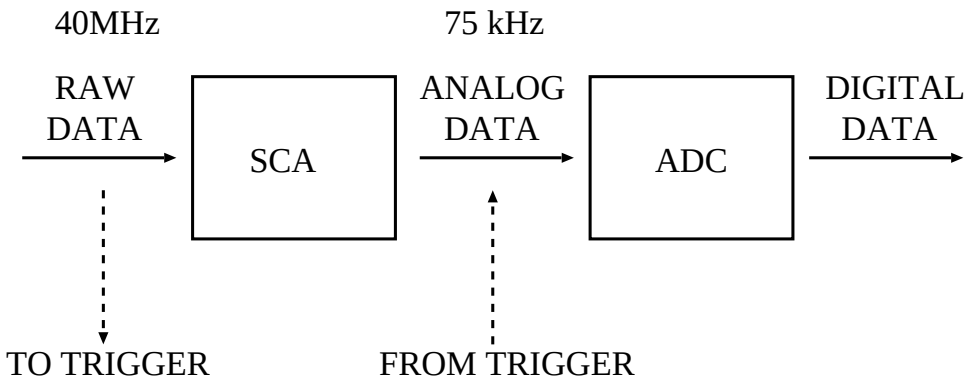

Figure 3.5: Block diagram of the data pipeline (75 kHz is the mean transfer rate).

for each board). For future reference, the channels were labelled 0 through 59, the capacitors 0 through 255, the time samples 0 through 7, and the boards 0 through 4. When an event was selected by the trigger it would be read out one sample at a time, with each capacitor being reset (i.e. shorted) as shown in Figure 3.3. During the readout of a capacitor, switch R2 was closed between the capacitor and an operational amplifier allowing the amplifier output to reach the voltage across the capacitor. After the readout time (2 μs or 4 μs) switch M1 was closed and the signal was read out at V_{out}.

3.4 Front-end Board Description

The purposes of the front-end board were to "hold" the data in an analog pipeline to await a decision from the trigger and then to digitize the selected data for transfer to mass storage (shown in Figure 3.5).

The readout electronics chain also contained the preamplifiers and shapers, although they were not located on the FEB. A block diagram showing the front-end

electronics chain is shown in Figure 3.6.

3.4.1 Pipeline Signal Preparation

The SCA required input signals with polarity and range different from that of the shaper amplifier output. The circuitry which provided the appropriate treatment of the signals from the shapers is shown in Figure 3.7. The signals coming from the shaper were bipolar, but inverted. The output range of the shaper signals was -2.0 V to 0.2 V. The first stage of the circuit was to invert the signals to the correct polarity and apply a gain of 1.25 to them. After this, the signals were shifted up by 1.25 V for input into the SCA. No gain was applied during this stage. The reason for the shift was to allow the measurement of the undershoot, the portion of the pulse which dipped below the baseline (1.25 V in this case).

3.4.2 Multiplexing and Gain Switching

Unlike the system described in section 2.3.5 a two gain system (rather than 3) was tested. This system used analog gain comparisons. With each trigger the samples were digitized and then multiplexed to minimize the number of ADCs required. The correct gain had to be selected as well. As shown in Figure 3.10, two channels coming from the output of the SCAs were multiplexed to a single input of an ADC. Figure 3.8 shows the block diagram of the circuitry from the SCA to the ADC. As the signals passed from the SCAs they were held in a sample and hold (S/H). A certain amount of time, referred to as the readout time, was allowed for the amplifier in the S/H to reach the desired voltage (within 0.01% of the voltage across the capacitor being read). After the readout time had elapsed, the S/H held the signal and the switch at

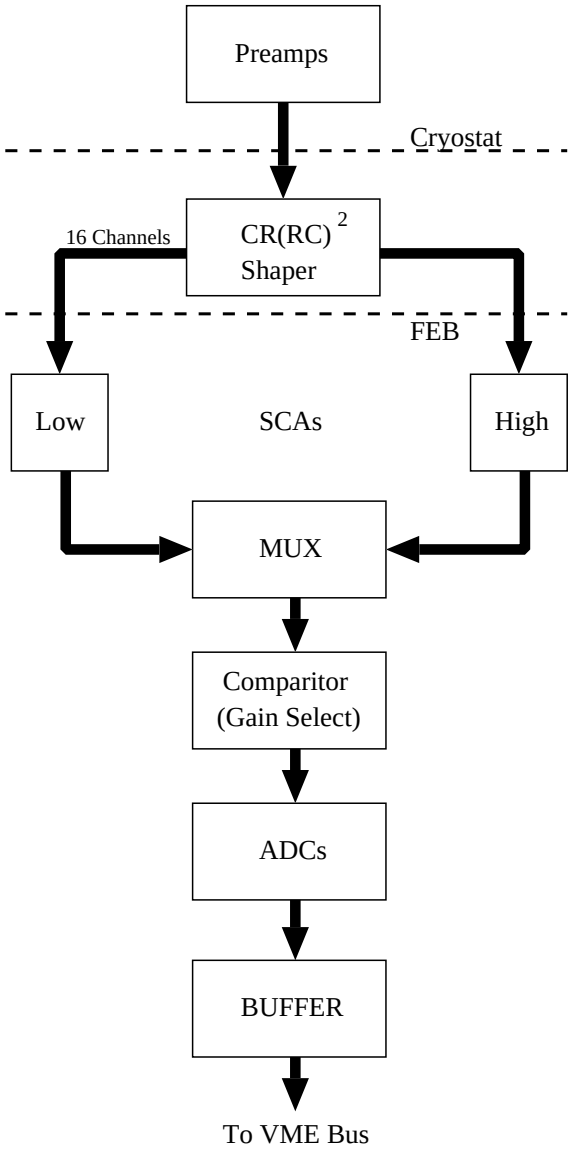

Figure 3.6: Block diagram of the front-end electronics chain.

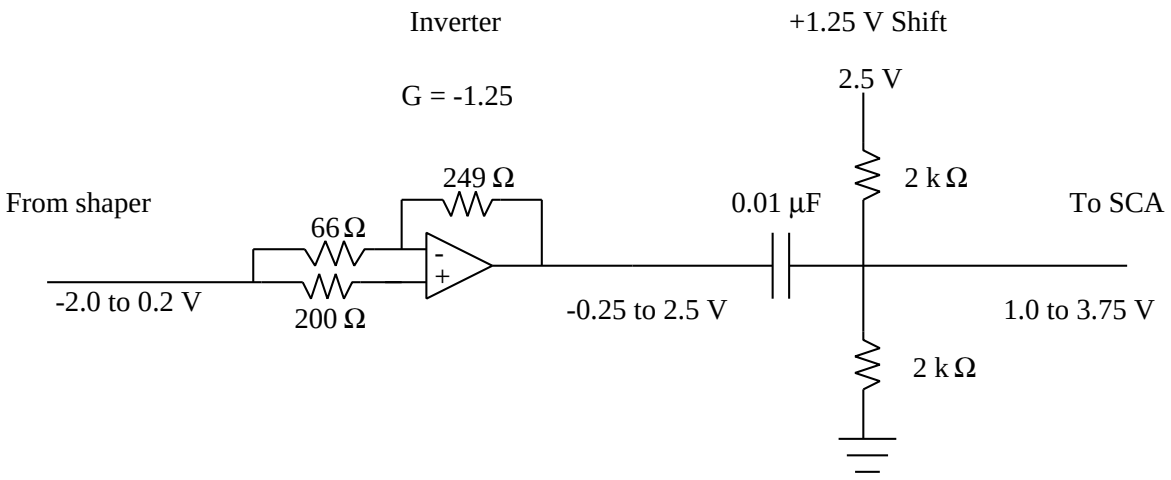

Figure 3.7: Circuitry used to prepare the output signals from the shapers to the desired polarity and range of the SCAs. The maximum signal ranges are given beneath the circuit.

A toggled to allow the passage of the signal. While one S/H was holding the signal, the other was sampling. This procedure was used as it took the same amount of time for the signal to pass through the circuitry to next S/H as it did to charge up the amplifier in the first S/H. If the pair of S/Hs following the SCA were not used, the additional readout time would be introduced due to multiplexing.

As both channels (N and N+1 in Figure 3.8) were being passed to the same ADC, the switch at **B** was used to alternate between the two channels. When the selected signal reached **C** in the diagram, a difference amplifier was used to subtract the reference voltage coming from the reference subtraction circuit (described in section 3.4.3). For the circuit corresponding to the high gain signals the S/Hs following this amplifier held the signals (one for each channel) while a comparator compared the signals to a fixed voltage (4.0 V) for the purpose of gain selection. If the signal was below the preset threshold voltage, the high gain channel was selected. If this

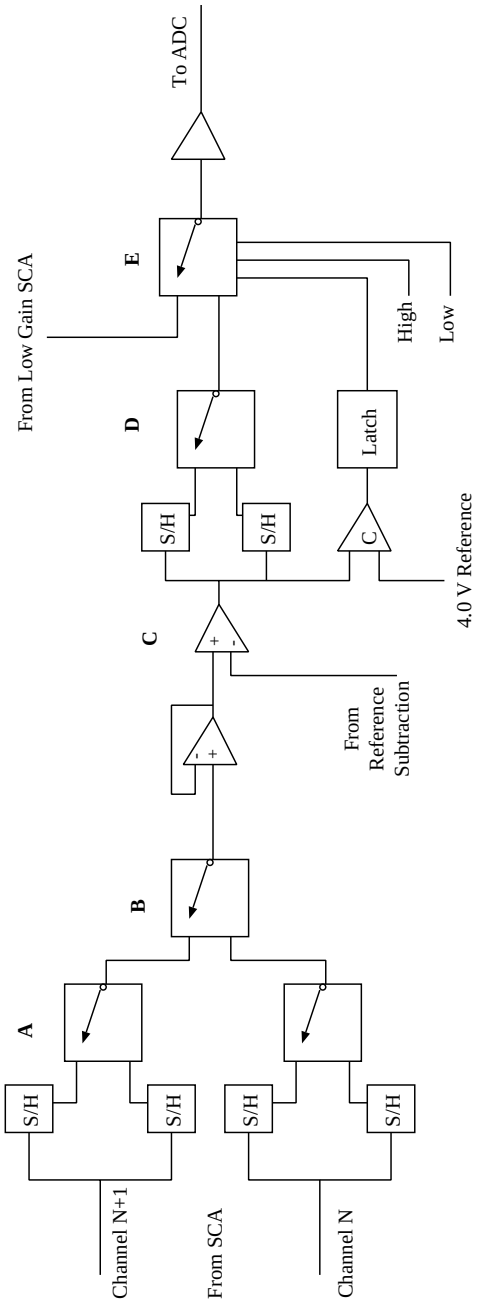

Figure 3.8: Schematic of the circuitry used to carry the data from the SCA to the ADC. The schematic shows two high gain channels (N and N+1). The low gain circuitry would not include the comparator. Full details are given in the text.

threshold amplitude was surpassed the low gain channel (from the other SCA) was selected. If the comparator produced a signal, due to the signal surpassing the 4.0 V threshold, the latch at **D** would hold the comparator output until the end of the event. If automatic gain switching was enabled, the gain switching described was done. Either gain could also be forced, at **E**, for digitization. The low gain circuit did not contain the gain comparison as only one of the gains was required for the gain selection process for a two gain system. The switch at **E** was used to select the appropriate gain from either SCA, corresponding either to the high gain or low gain signals.

3.4.3 Reference Subtraction Circuit

The reference subtraction circuit was used to allow noise subtraction. This was done so that the voltage level in the reference channel could "float" and thus any cross-talk from close channels or calorimeter cells, or other systematic noise, would be subtracted off of the data pulse. The level of coherent noise across channels should be reduced. The reference subtraction circuit (Figure 3.9) used channels which were not used for data, but were still susceptible to systematic noise across the system (channels). These channels had different impedances than the data channels as they were not connected to the shapers. The subtractions came from the 4 channels in each SCA chip (Figure 3.10). For channels 0 through 7, the even channels were subtracted with channel 2 and the odd channels with channel 3. For channels 8 through 15 the even channels were subtracted with channel 10 while the odd channels were subtracted with channel 11 (Figure 3.10). When the circuit was disabled, a fixed voltage was used as the reference voltage. The numbering of channels used in this thesis was purely arbitrary and hence sequential for simplicity. It did not correspond to the

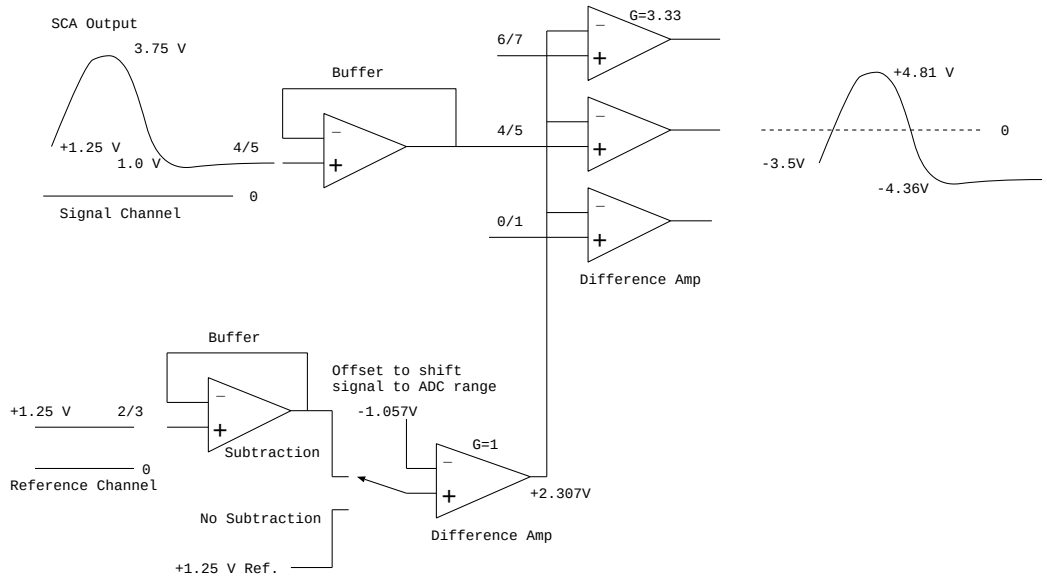

Figure 3.9: Schematic of the reference-subtraction circuit. The 4/5 and 2/3 refer to two channels sharing the same line. The zero lines refer to ground for both the signal and reference channels.

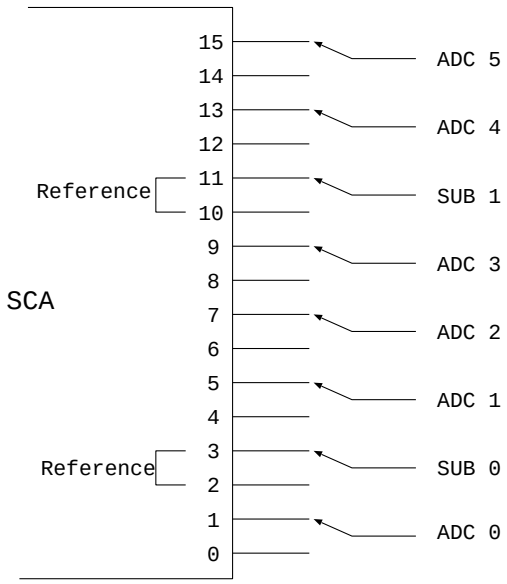

Figure 3.10: Channel layout on SCA chip.

layout in Figure 3.10.

3.4.4 Event Building

An event which was selected for storage consisted of more than the ADC counts of each sample. Each event also contained extra event-related information, such as the gain selected, the event number, the readout time, etcetera. The event building procedure took place in digital circuitry between the ADCs and the VME bus. The bus was used to transfer the data to a SUN SPARC workstation which was used for data acquisition (Figure 3.11). The circuit shows the signal lines from three ADCs corresponding to 8 SCA channels. Two of the SCA channels were used for reference subtraction and required no analog to digital conversion. The 14-bit ADC data words were fed into a 16-bit latch where a gain bit, signifying which gain branch the signal originated from, was added to the data word. The events were then built by packing additional digital information, in the form of column and header words, in front of the data words in a 16-bit (4096 deep) First In First Out (FIFO) memory. The column and header words contained information such as the time of event, event number, capacitor address, readout time, as well as other relevant information which would be used in the data analysis. The events were then passed to a VME bus which carried them to a SUN Sparcstation for writing to tape, and on-line monitoring.

3.5 Description of the Controller Board

In order to keep the pipeline readout system from contributing dead-time, the system allowed simultaneous read and write operations as well as the ability to write to non-sequential addresses in the SCA. If the data was stored sequentially, dead-time

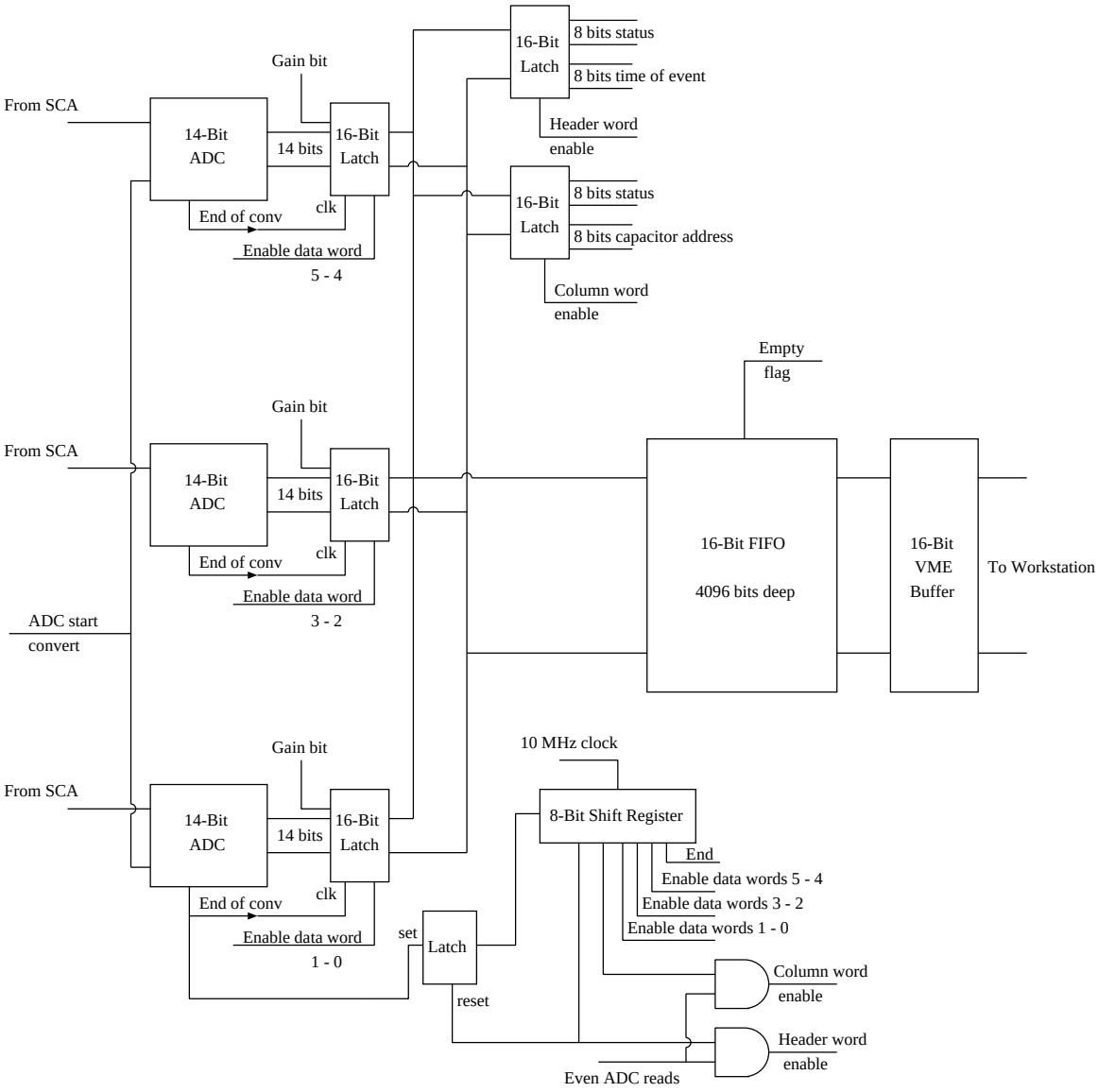

Figure 3.11: Schematic of the event building circuitry for 8 ADC channels.

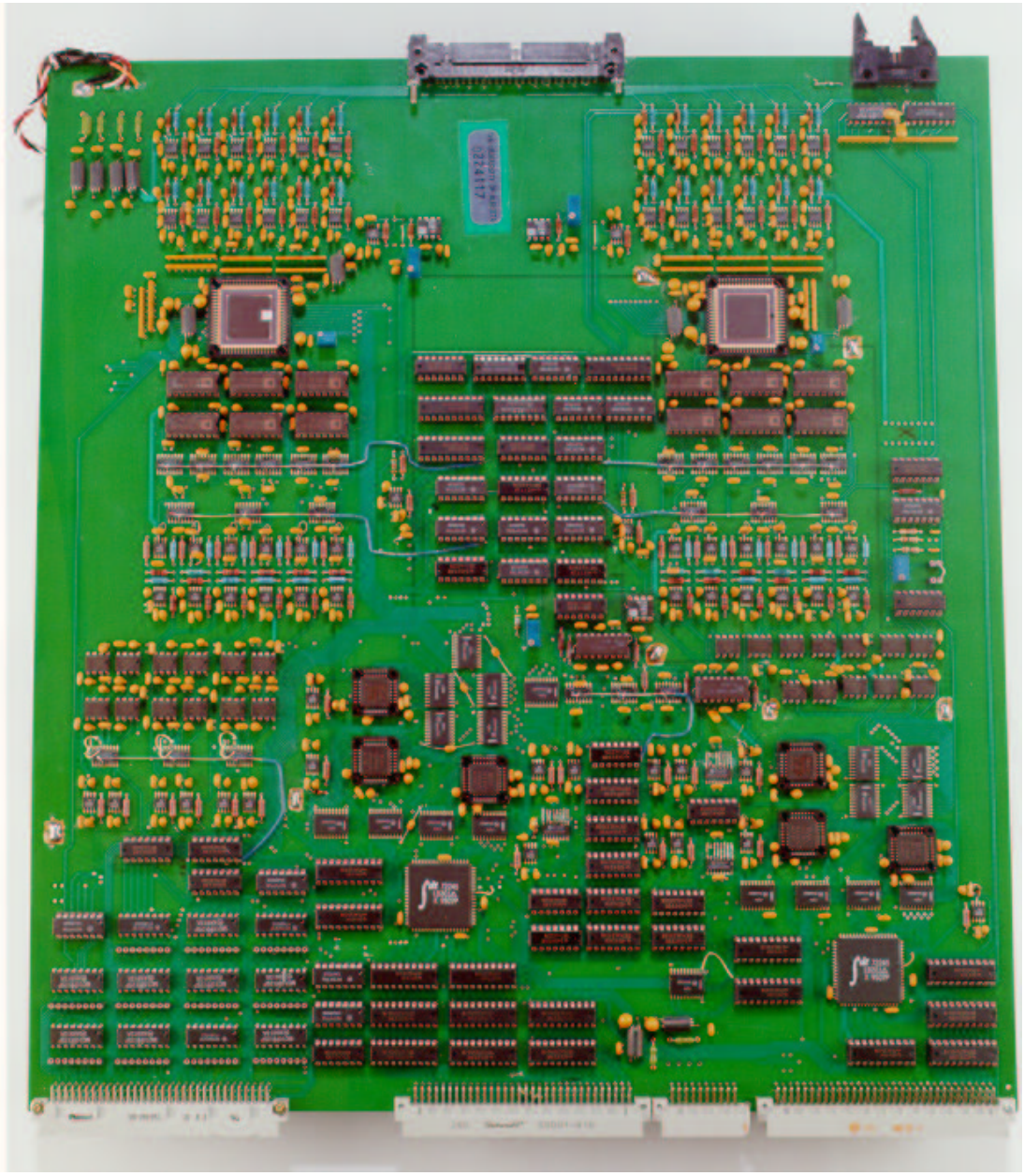

Figure 3.12: Photograph of a front-end board similar to those used in the test. The power, control, and signal input connectors are shown at the top. The 9U VME and JAUX connectors are shown at the bottom. The two large chips on the top third of the board are the SCAs.

would be introduced, as a function of the number of storage cells per channel and the time required to read out each sample [19]. A design was chosen such that the SCA addresses could be kept track of and read and write operations could be done to non-sequential addresses. The device that managed the address storage was the Address List Processor (ALP) circuit. The the purpose of the pipeline controller board was to contain and service this circuitry. A simplified block diagram of the ALP circuit is shown in figure 3.13.

The ALP circuit worked by digitally simulating the flow of information which occurred in the analog SCA pipeline. While in the SCA, an address was in a particular "mode". The ALP would place that address into a FIFO corresponding to that mode. If for example, an SCA address contained data which was awaiting a trigger decision, that address would sit in the READ-DELAY FIFO of the ALP. The WRITE FIFO contained addresses which were available for writing. As a write was required, once per cycle, the next address was removed from this FIFO and the corresponding address written to in the SCA. The address was then placed into the READ-DELAY FIFO to await a trigger decision from the first level trigger. If the address was not selected for reading in the SCA, it was returned to the WRITE FIFO. If the address was selected by the trigger it was moved into the READ FIFO until it had been read on the SCA. Once read out, the addresses were placed in the READ-COMPLETE FIFO until they were passed back into the WRITE FIFO for future writes. The entire process was synchronized by the pipeline clock. As each FIFO was the same size as the SCA pipeline (256 addresses) there was no danger of overflow. If the WRITE FIFO became full, indicating an error, a reset signal was used to clear all of the FIFOs. All addresses were then loaded into the WRITE FIFO and the process resumed.

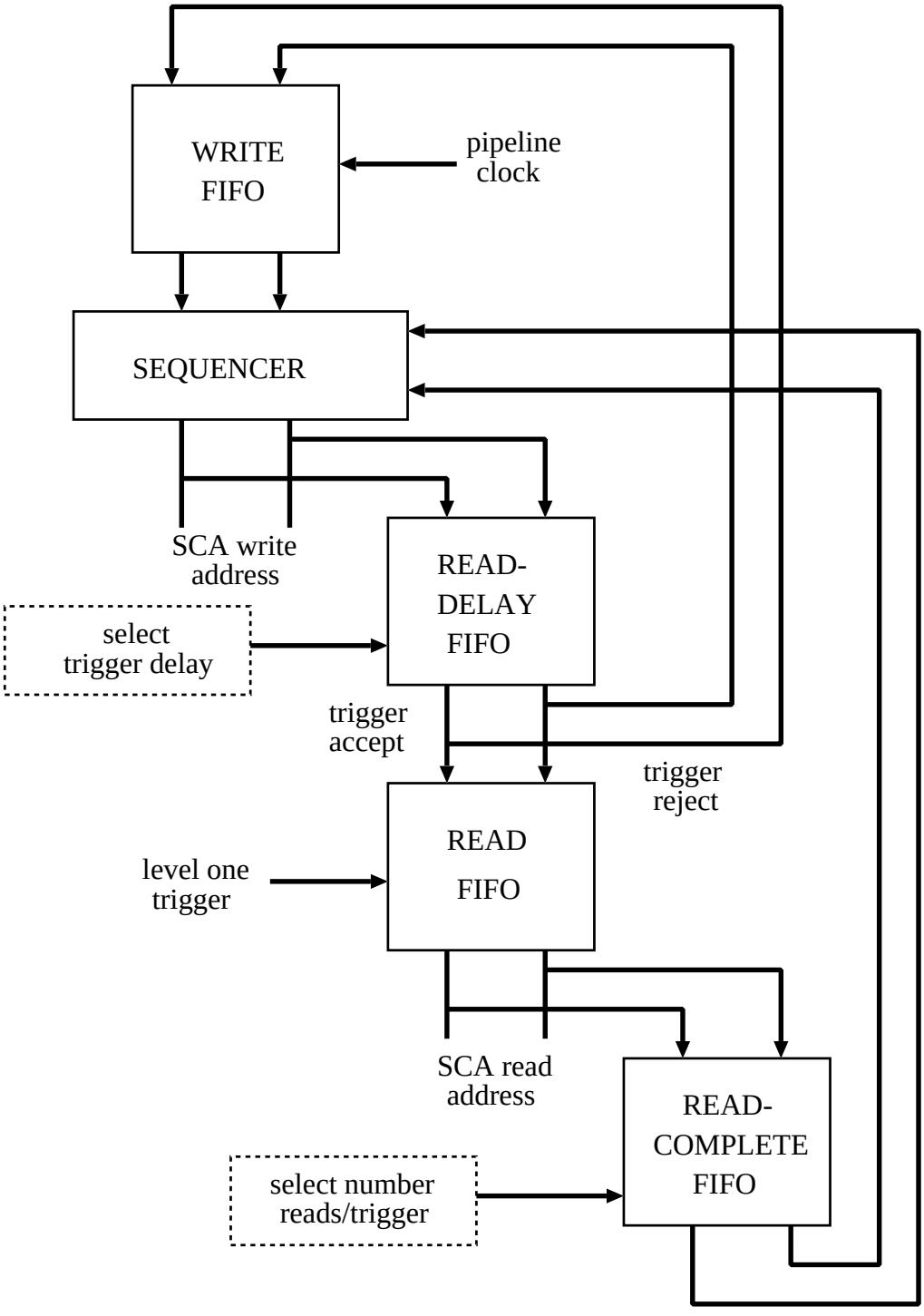

Figure 3.13: Block diagram of the address list processor design.

CHAPTER 4

Readout System Studies

4.1 Introduction

The systematic studies of the front-end system were of two types: static noise studies, where the system was not driven by any type of pulses, and calibration studies, where the system was driven by well defined signals. The noise studies provided the opportunity to measure the noise, both incoherent (random fluctuations) and coherent (systematic across channels). It was also possible to observe the effect of changing certain run-time parameters, such as the amount of time taken to read out a capacitor from the SCA. Calibration studies were used to determine the dynamic range and linearity of the system, as well as, the automatic gain switch voltage. The calibration data was also used to measure the cross-talk between channels.

A total of 28 noise runs* were taken. Each of these runs consisted of approximately 30000 events. This number was chosen to ensure that sufficient statistics were achieved (i.e. each capacitor was charged roughly 100 times (Figure 4.1)). There were 24 calibration runs taken for the gain, linearity and cross-talk measurements. Tables containing information about the data can be found in Appendix A.

There was a system malfunction during one run where the reference subtraction circuit was disabled and the low gain readout was forced (run 32880). In this run

*A run was a fixed amount of continuous data reading.

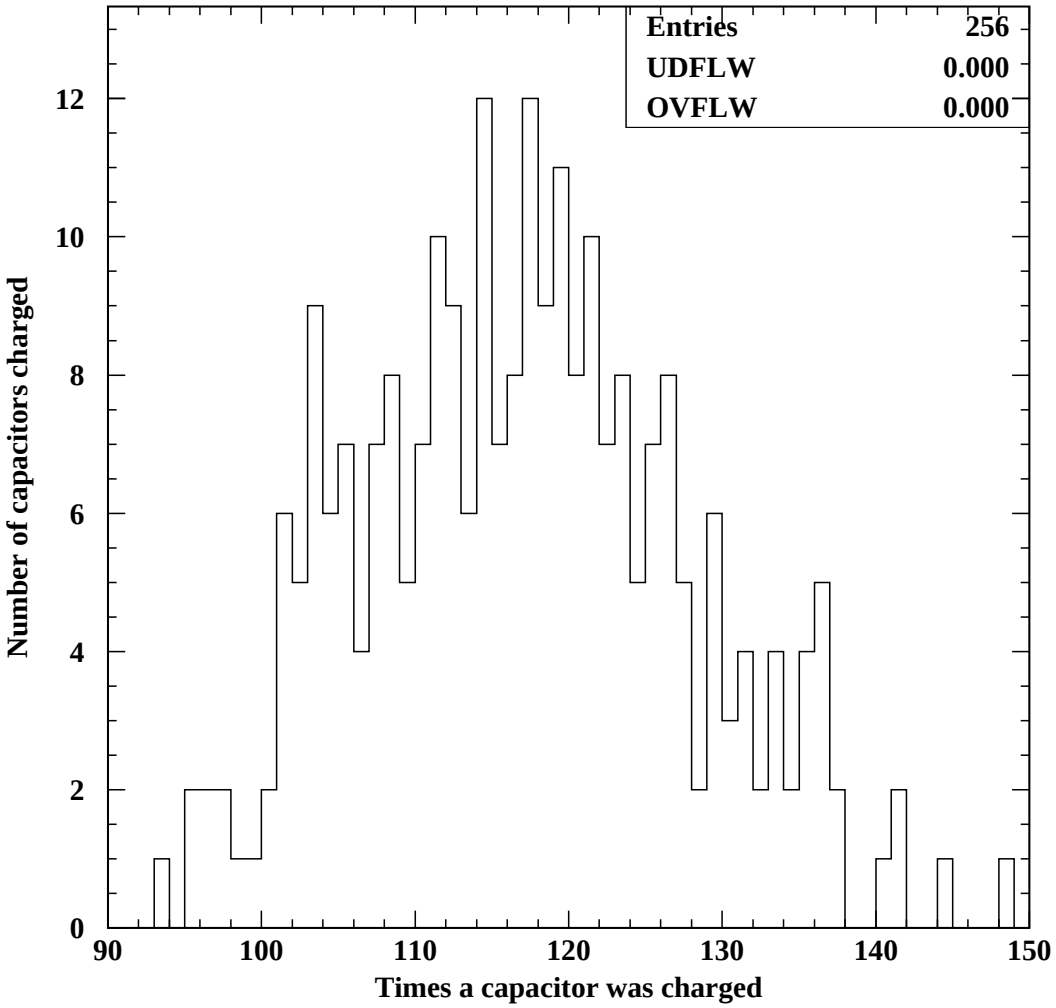

Figure 4.1: Distribution of times each capacitor was charged for a run where high gain readout was forced (Run 32689).

there were 402 events (from 18721 to 19123) which were discarded due to an error in the data format†. The source of the error was not known but as it was the only run with a unique operating condition, the run was used.

4.2 Amplitude Measurements

The data consisted of amplitude values, measured in ADC counts*, which were a function of four variables: time (event number), channel, capacitor, and sample. While both event number and sample were measures of time, they were considerably different independent variables. The event number was a measure of the time over the period of a run, while sample was a measure of the time evolution of a pulse. The channel and capacitor variables were illustrated in Figure 3.4. Using the measured ADC counts it was possible to observe any strange behaviour in the system, such as "dead" channels, where no ADC counts were observed. Figure 4.2 shows that, for the high gain† system, three cells (31, 73, and 178) behaved in an anomalous manner. For these cells an offset of the amplitude values was observed. Upon closer examination it was determined that the cells fluctuated for all 60 channels, and over all similar runs. For the low gain system, there was one cell which behaved in an anomalous manner (cell 84), again affecting all channels. When the ADC counts were plotted against the other variables (event number, channel, and sample) no anomalous data was apparent. The reasons for the anomaly are discussed in section 4.7.

When the reference subtraction circuit (described in section 3.4.3) was disabled, two channels (34 and 35) registered no ADC counts for the high gain system

†The data format refers to manner in which the additional event information (described in section 3.4.4).

*An ADC count refers to the least significant bit coming from the ADC.

†The use of the term gain is quite informal here. It refers to the corresponding electronics chain. The term will be used throughout the remainder of this thesis in the same manner.

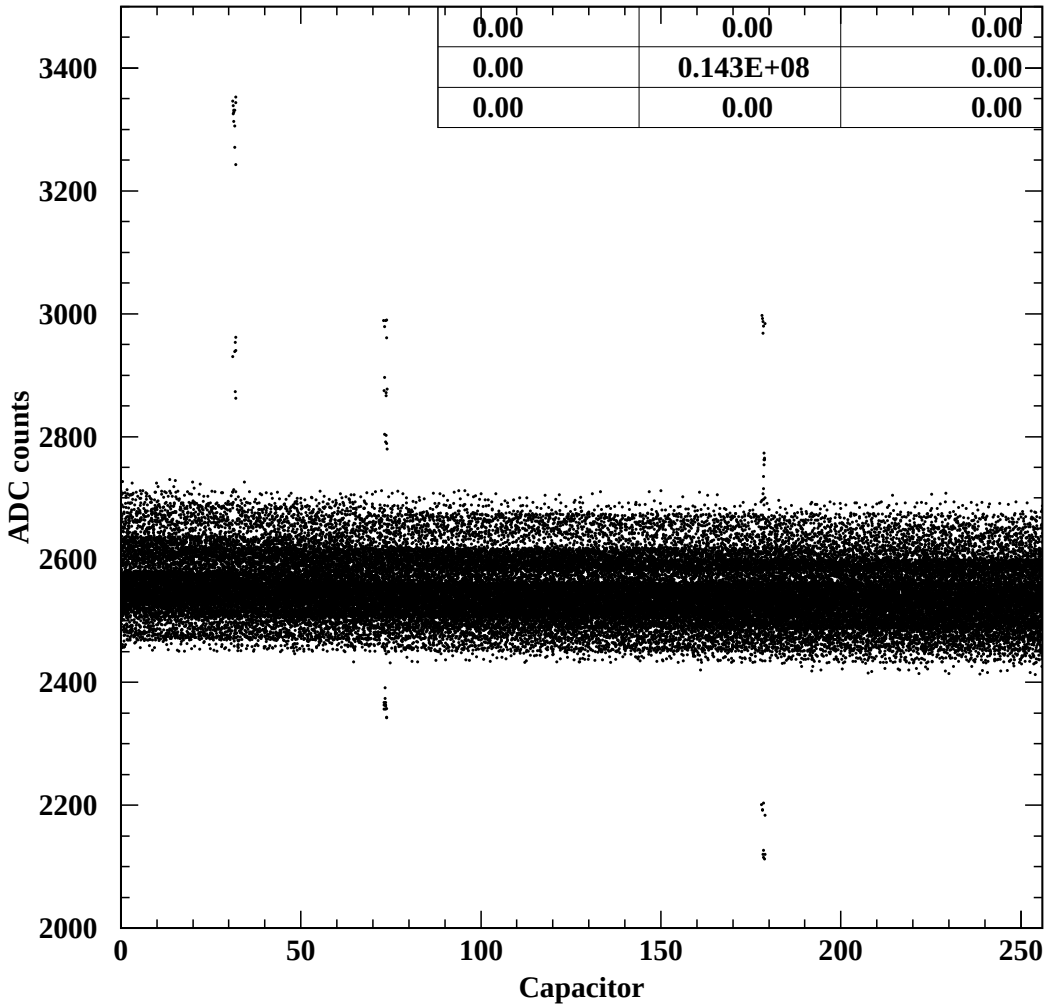

Figure 4.2: Amplitude (in ADC counts) vs cell number. The data was taken from a run with forced high gain readout. Note that "Capacitor", plotted on the X-axis, refers to "Capacitor number".

in one run (32760). These channels corresponded to the last two channels on the first board, and the two right bottom cells of the second layer of the calorimeter (Appendix C). Two electron runs were taken immediately following the noise run and while the first of these exhibited the same dead channels, the second did not. As the dead channels were the last two on the board, hence chip, they would have been associated with the same ADC. The signals from that particular ADC would have shared a line from the ADC to the VME bus and any temporary problem with that line could have caused the effect. No similar problems were encountered with the remainder of the data.

It was expected that there would be amplitude fluctuations above the Root Mean Squared (RMS) noise, in the measured ADC counts, from capacitor to capacitor and channel to channel, but it was not expected that there would be such fluctuations between time samples. Figure 4.3 shows that for four different channel and capacitor pairs there was no fluctuation above the RMS. The top two plots in Figure 4.3 (a and b) illustrate the amplitudes for channels and capacitors which did not exhibit excessive noise. The capacitor in the bottom left plot was noisy as was the channel in the bottom right plot. Each capacitor and cell pair appeared to have average amplitude values which oscillated slightly from sample to sample. As these oscillations were less than RMS no correction was made.

The amplitude was averaged over two of the three variables and examined as a function of the third. The average amplitude for a single variable i was given by:

$$ADC_i = \frac{\sum_{j,k} ADC_{i,j,k}}{N_{j,k}}, \tag{4.1}$$

where $N_{j,k}$ is the number of terms in the sum. The results are plotted in Figure 4.4. In Figure 4.4 (a) it can be seen that there was up to 200 ADC counts of fluctuation between the channels across the system. The two points in the plot of average

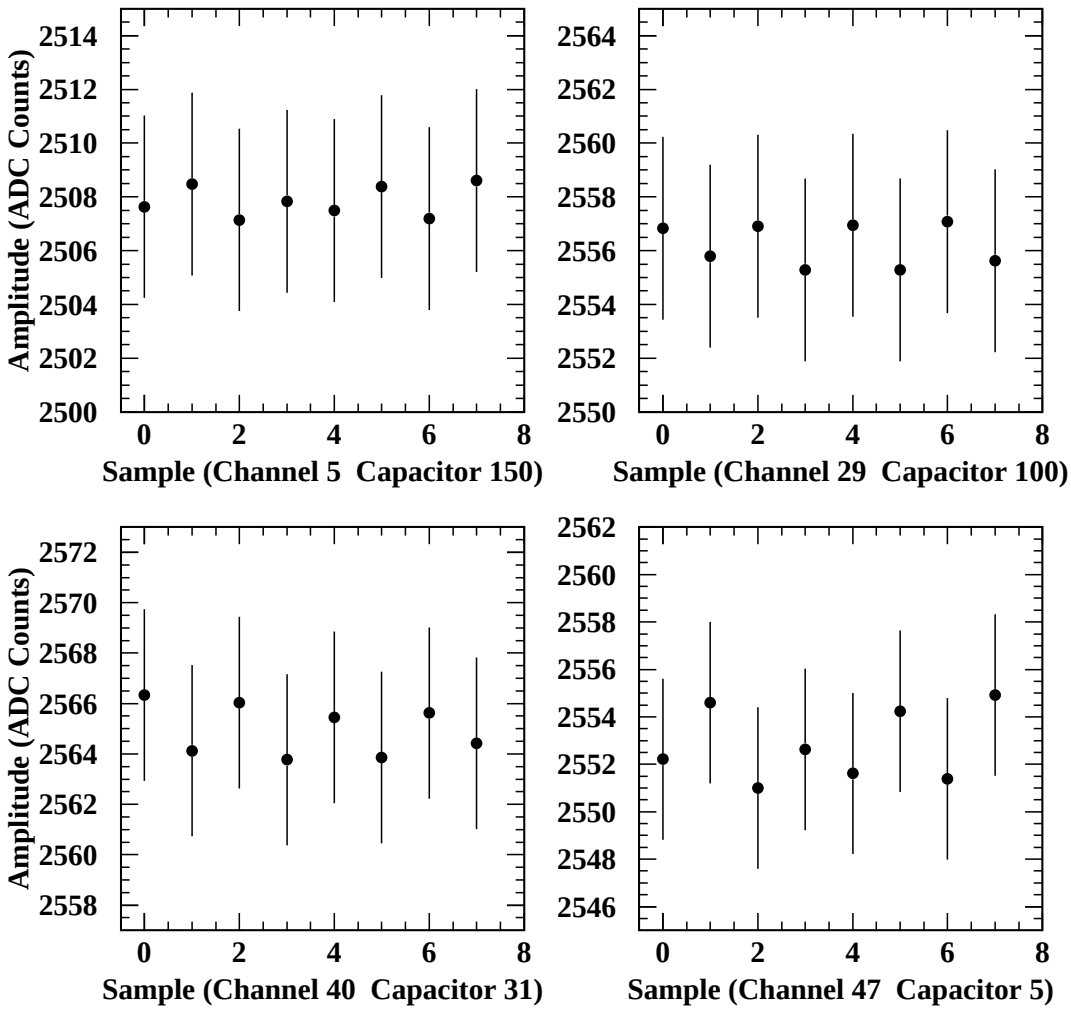

Figure 4.3: Mean amplitude for four particular capacitors and channels plotted as a function of time sample. The a and b used data with non-noisy channels and capacitors while the capacitor in plot c was noisy, as was the channel in plot d. The data was taken from a run with forced high gain readout (Run 32689).

amplitude as a function of capacitor (Figure 4.4 (b)) which were significantly higher than the rest corresponded to capacitors 31 and 73, which were found to give anomalous amplitude readings (illustrated in Figure 4.2). The trend of decreasing average amplitude as a function of capacitor number could be attributed to bus capacitance which is explained further in section 4.7. The trend (a drop of approximately 35 ADC counts) was observed for each channel. Figure 4.4 (c) illustrated that the average amplitudes oscillated from one sample to the next. This oscillation was observed for the average total noise. A possible explanation for the behaviour is given in section 4.7.

It was important to determine if there was a fluctuation in system performance over time. There were two aspects of the performance, which may have fluctuated over time: the immediate performance over the duration of a run and the performance over the duration of the test period (5:54PM June 16 1996 to 4:57PM June 20 1996). The latter was important as there were changes being made to the run parameters and as well the calorimeter was physically moved for a short time to allow the testing of the mono-gain shapers and then returned to its original position. The amplitudes were compared for runs with the same operating parameters at the beginning and end of the test period. No fluctuations were apparent as can be seen in the data summary contained in Appendix B. In addition, there was no significant fluctuation in amplitude over the duration of a run. Thus the stability of the system was good.

4.3 Incoherent Noise Measurements

The noise, or measured amplitude fluctuations, of the system places a limit on the precision of the measurements which can be made. This reduces the effective dynamic

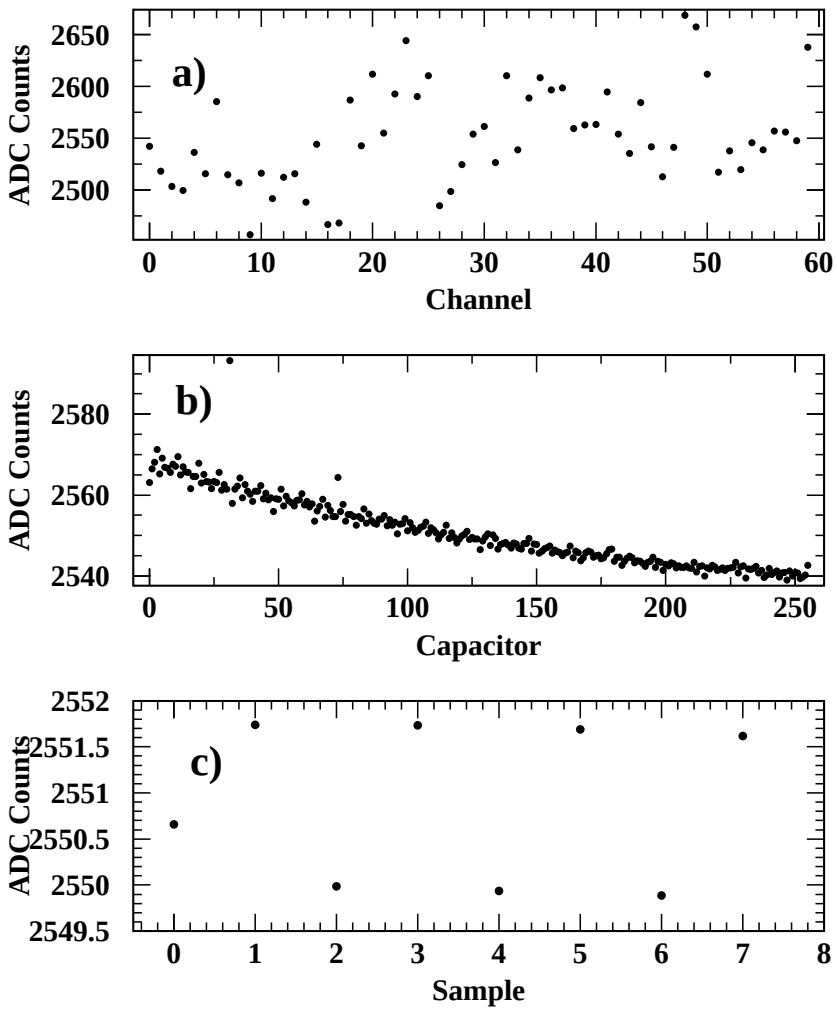

Figure 4.4: Average amplitude plotted against the three independent variables, channel (a), capacitor (b), and sample (c). The data was taken from a run with forced high gain readout (Run 32689).

range of the system. The RMS noise was measured using the expression:

$$\sigma_{i,j,k} = \sqrt{\frac{1}{N-1}\sum_{N}(ADC_{i,j,k} - \overline{ADC_{i,j,k}})}, \tag{4.2}$$

where N was the number of amplitude measurements and $ADC_{i,j,k}$ was an amplitude measurement for a particular channel (i), address (j), and sample (k), and $\overline{ADC_{i,j,k}}$ is the average amplitude measurement.

An equivalent measure of the incoherent (or random) noise of the system is the width of the ADC count distribution shown in Figure 4.5. The dispersion, which was defined as

$$d_{i,j,k} = ADC_{i,j,k} - \overline{ADC_{i,j,k}} \tag{4.3}$$

gave a measure of the random fluctuation of the amplitude measurements. The distribution had a Gaussian shape. The width of this distribution was taken to be the incoherent noise of the system.

The RMS noise* was examined as a function of each of the three variables. This was done by first plotting $\sigma_{i,j,k}$ against each of the three variables (Figure 4.6). It can be seen that the last channels on each board contributed additional noise which manifested itself as the tail in the noise distribution. There appeared to be no other variables which experienced such an effect. The same noise pattern was exhibited in the forced low gain readout data and persisted throughout the test period. Fortunately, the five channels corresponded to outer regions of the calorimeter, away from the beam impact point (Appendix C).

The averaged noise, for channel, capacitor, and sample, of the system was examined as a function of each of the three variables, as shown in Figure 4.7. The

*Both the RMS fluctuations and incoherent noise refer to the random noise of the system and will be used interchangeably.

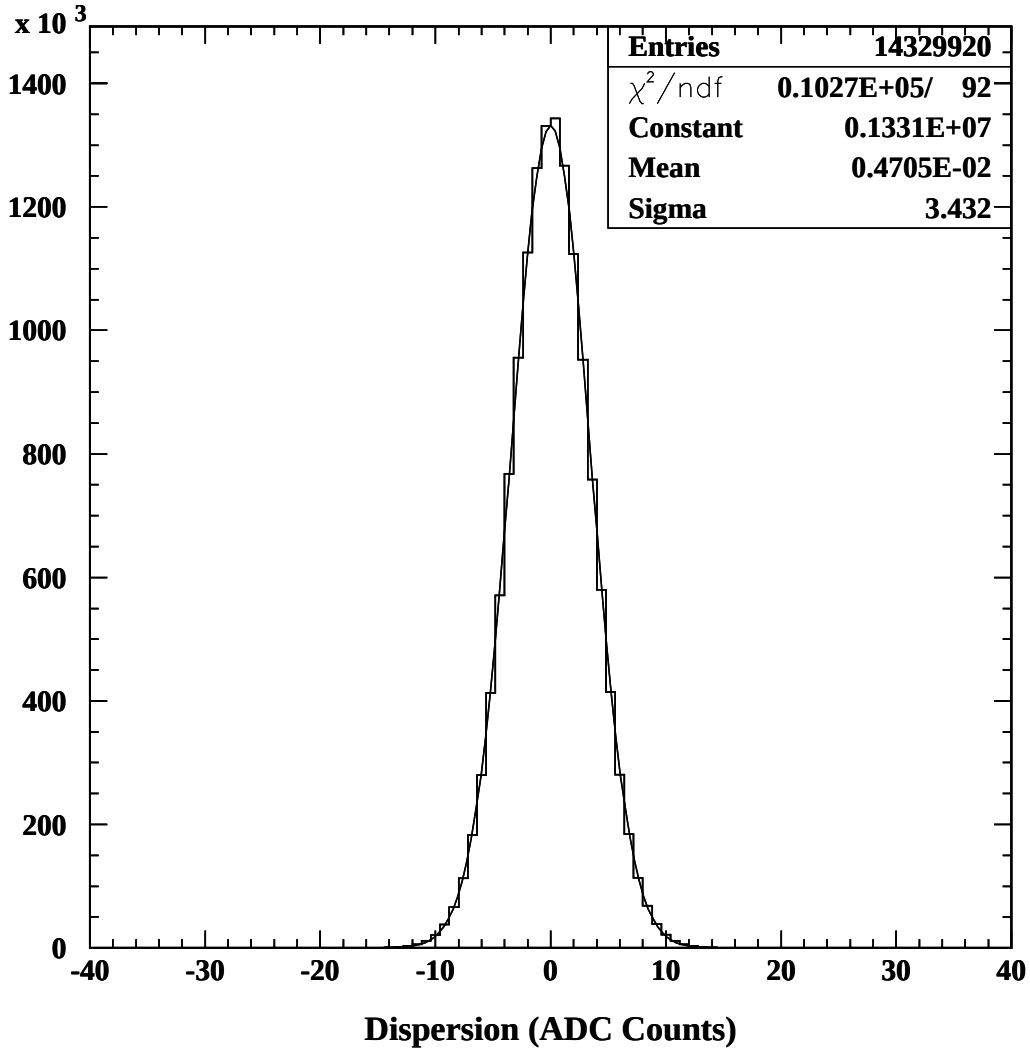

Figure 4.5: Dispersion in ADC counts for high gain run for each channel, capacitor, and sample. The fit was Gaussian.

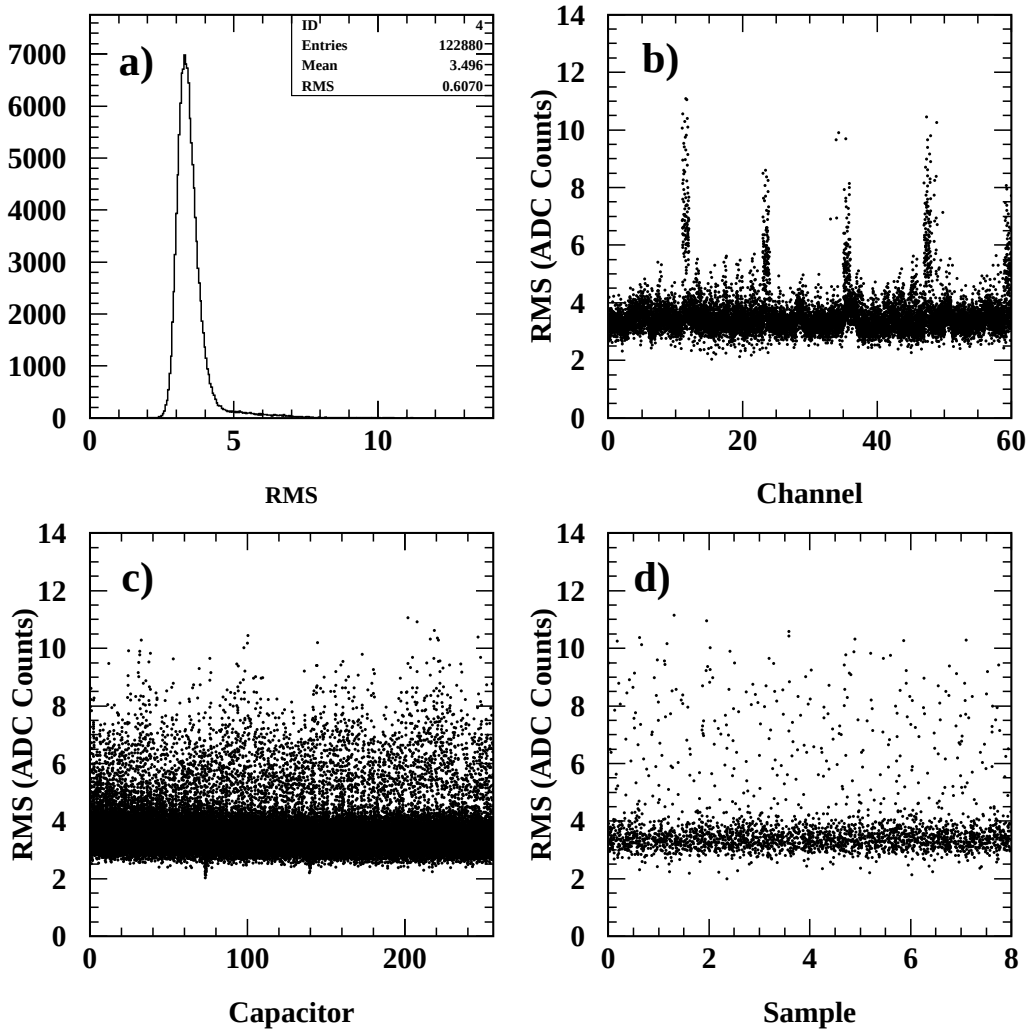

Figure 4.6: RMS noise (with no averaging) plotted against the three independent variables, channel (b), capacitor (c), and sample (d). Plot (a) contains all RMS measurements to demonstrate the total noise distribution. The data was taken from a run with forced high gain readout (Run 32689).

average noise for a single variable i was given by:

$$\sigma_i = \frac{\sum_{j,k} \sigma_{i,j,k}}{N_{j,k}}, \tag{4.4}$$

where $N_{j,k}$ is the number of terms in the sum.

The average noise values for each sample (Figure 4.7 (c)) were consistent to within an ADC count. Similarly, the noise as a function of channel and capacitor (Figures 4.7 (a) and (b)) were consistent to within 1 ADC count. The five points which had higher RMS values than the rest on the RMS versus channel plot (Figure 4.7 (a)) corresponded to the last channel on each board. The RMS values in the noise versus capacitor plot (Figure 4.7 (c)) oscillated from capacitor to capacitor, although within the RMS deviation. A summary of the noise estimates (average RMS per run) can be found in Appendix B.

4.4 Coherent Noise Estimate

The total noise of the system is comprised of two parts, coherent and incoherent (previously described), and is described by the following expression:

$$\sigma_{Total} = \sqrt{n\sigma_{incoh}^2 + n(n-1)\sigma_{coh}^2}, \tag{4.5}$$

where σ_{coh} is the average coherent* noise contribution, σ_{incoh} is the average incoherent noise contribution, and n is the number of channels examined. The coherent noise can be estimated using the measured amplitudes†. The idea was that the amplitude dispersions in each channel should, on average, cancel out as they can carry either sign (Figure 4.5). This fact can be exploited to estimate the systematic, or coherent

*Coherent noise used in this context means coherent over channels. The coherent noise described in this thesis is a systematic effect between channels.

†The method used in this thesis was obtained from D.M. Gingrich.

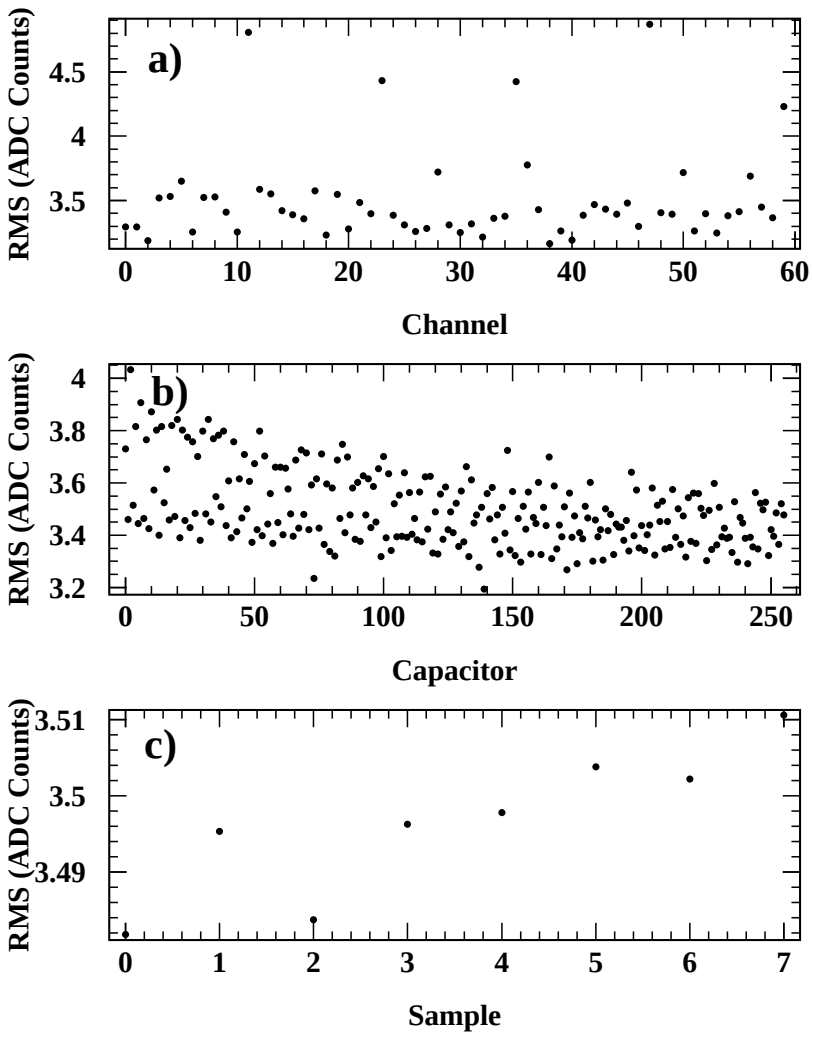

Figure 4.7: Average RMS noise plotted against the three independent variables, channel (a), capacitor (b), and sample (c). The data was taken from a run with forced high gain readout (Run 32689).

noise. The coherent noise estimate is outlined in the following derivation [20]. The quantities S^+_{jkn} and S^-_{jkn} were defined as follows:

$$\begin{aligned} S^+_{jkn} &= A_{0jkn} + A_{1jkn} + A_{2jkn} + \cdots + A_{ijkn} + \cdots + A_{(NChannels-1)jkn}, \\ S^-_{jkn} &= A_{0jkn} - A_{1jkn} + A_{2jkn} - \cdots + A_{ijkn} - \cdots - A_{(NChannels-1)jkn}, \end{aligned} \tag{4.6}$$

where i corresponds to the channel, j the capacitor, k the sample, and n the event number. The A's are the amplitude dispersions, given by:

$$A_{ijkn} = x_{ijkn} - \mu_{ijk}, \tag{4.7}$$

where x_{ijkn} are the amplitudes and μ_{ijk} are the average (over event) amplitudes. If σ^+_{jk} and σ^-_{jk} are defined as:

$$\begin{aligned} (\sigma^+_{jk})^2 &= \frac{1}{N_{events}-1}\sum (S^+_{jkn})^2, \\ (\sigma^-_{jk})^2 &= \frac{1}{N_{events}-1}\sum (S^-_{jkn})^2, \end{aligned} \tag{4.8}$$

the coherent noise across the system (channels) is:

$$\sigma^{coh}_{jk} = \frac{\sqrt{(\sigma^+_{jk})^2 - (\sigma^-_{jk})^2}}{N_{chan}}. \tag{4.9}$$

A distribution of coherent noise for each capacitor and sample across the system is shown in Figure 4.8. The coherent noise was examined not only across the system but also for each board (Figure 4.9) (SCAs in mono-gain operation) as well. By examining individual boards, it was thought that any systematic noise introduced on a single board could be discovered. The fourth board exhibited more coherent noise* than the others which manifested itself in a secondary peak in the coherent

*The term coherent noise refers to the corresponding mean of the relevant coherent noise distribution.

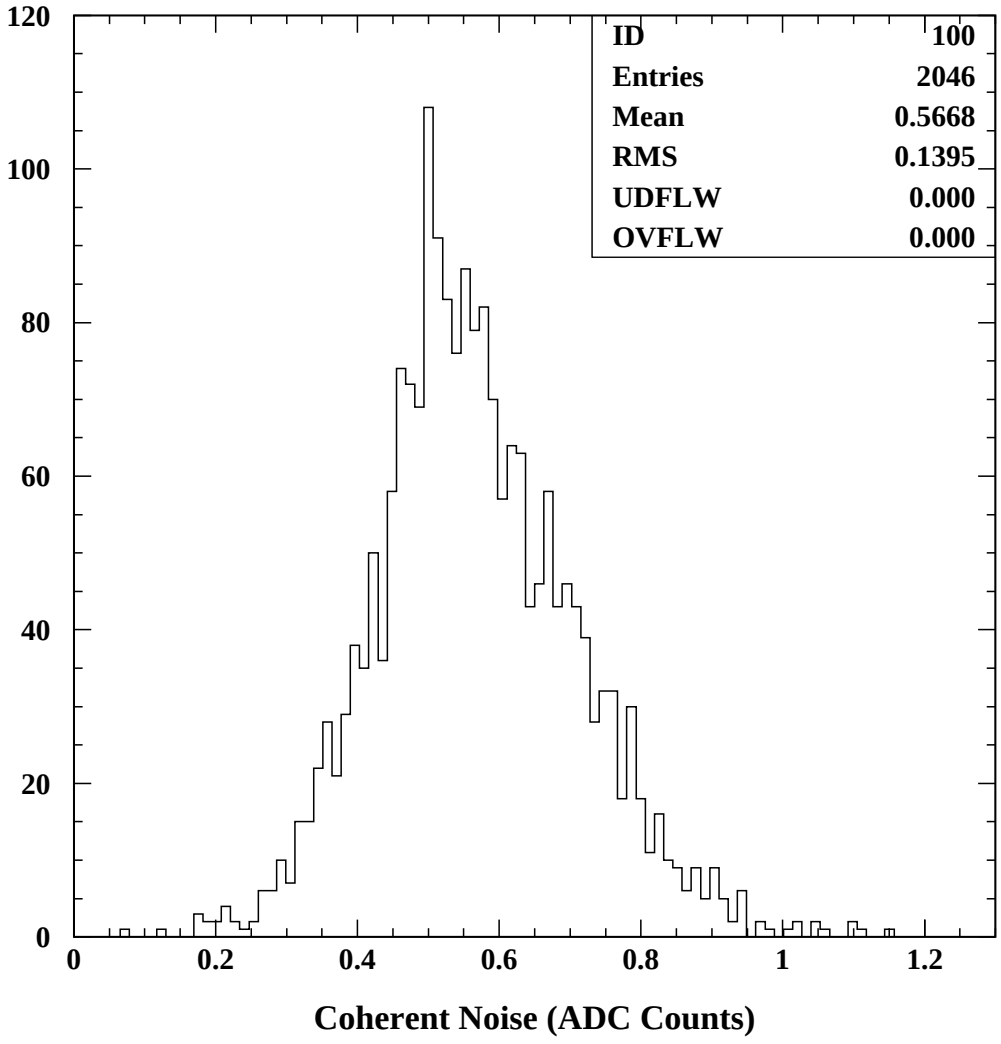

Figure 4.8: The coherent noise across channels for the entire system (all five boards). The data was taken from a run with forced high gain readout.

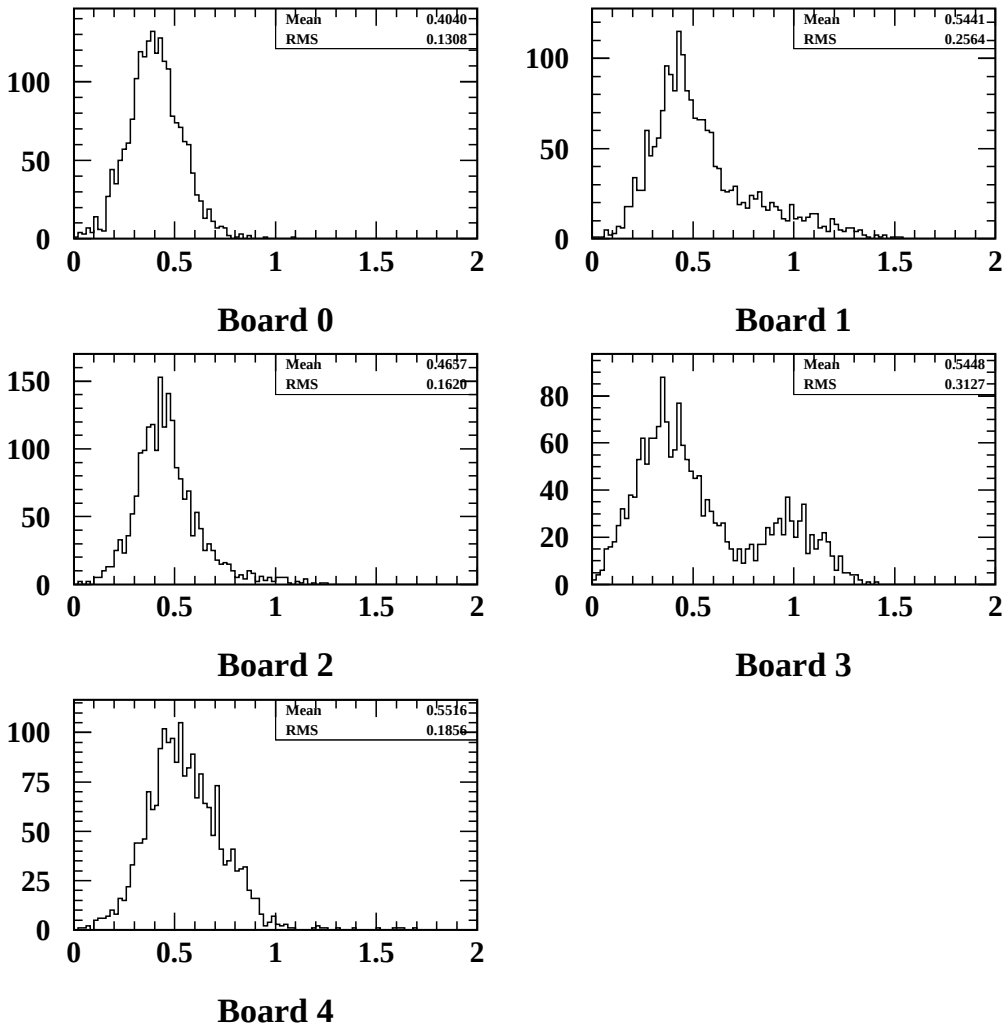

Figure 4.9: Coherent noise (in ADC Counts) across channels for each of the five boards. The data was taken from a run with forced high gain readout (Run 32689).

noise distribution above the primary peak. The peak remained for runs where low gain readout was forced. The coherent noise did not exhibit any capacitor or sample dependence (Figure 4.10). Removing the data for the noisier capacitors from the calculations, had no measurable effect on the coherent noise across the system or on individual boards. A summary of the coherent noise for the baseline runs (runs with no changes made to the run parameters) can be found in Appendix B.

4.5 Effect of Different Operating Conditions on Noise

The system tests included a study of the effect of three operating settings which were varied between the runs. The three parameters were the write clock, readout time, and the reference subtraction circuit. The write clock was used to allow simultaneous read and writes to the SCA. If the clock was disabled there was no writing during the time it took to read out the 8 samples of an event. The clock was disabled for baseline (original run parameters used) runs and during tests of other parameters. The readout time was reduced to 2 μs from 4 μs (the 4 μs was used for the majority of the runs - including all baseline runs) to observe the effect. The longer readout time was used for the majority of the test period. The reference subtraction circuit described in section 3.4.3 was also disabled for test purposes.

The trigger delay, or time between a write to the SCA and a trigger, was also varied. This parameter should not affect the noise. The effect of the trigger delay is discussed in later sections.

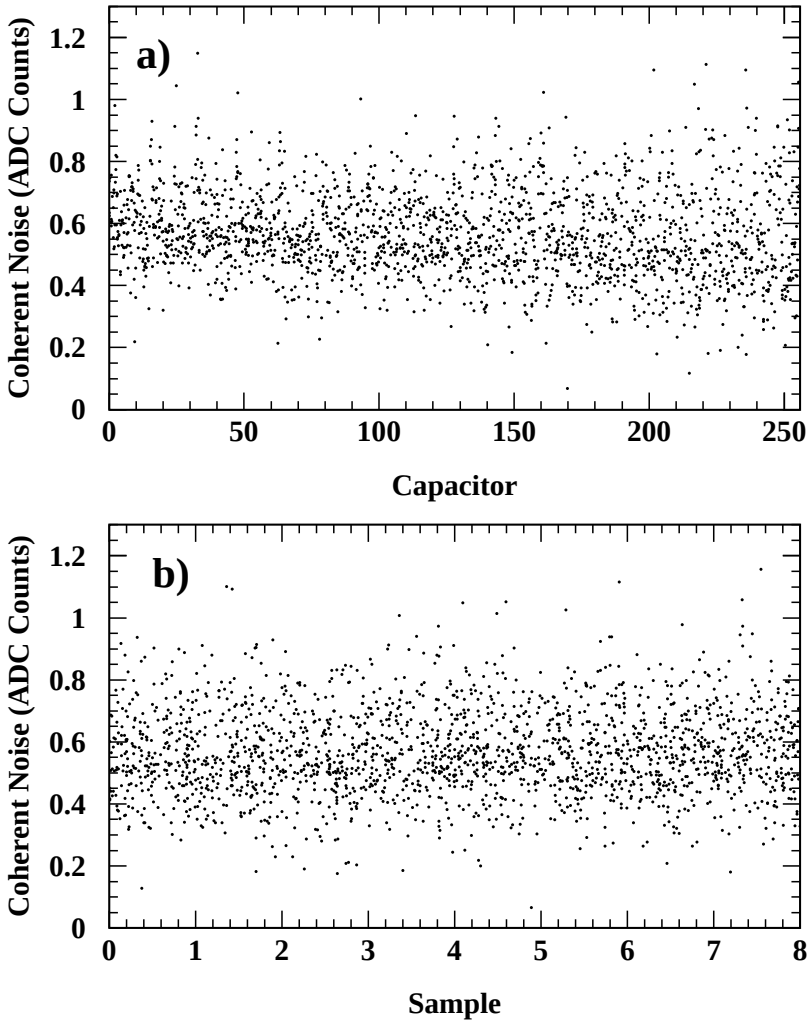

Figure 4.10: The coherent noise as a function of capacitor (a) and sample (b). The data was taken from a run with forced high gain readout (Run 32689).

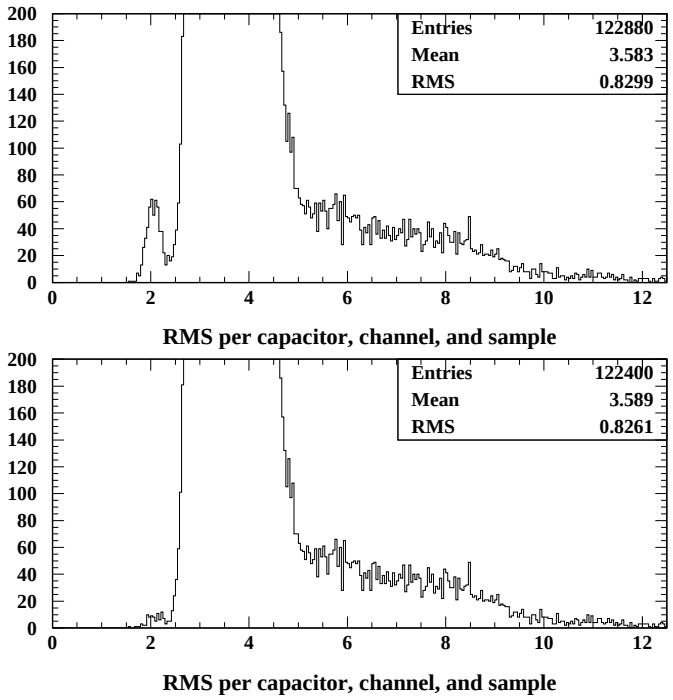

Figure 4.11: RMS noise with write clock enabled. Top: All data contained in calculations. Bottom: Data from first capacitor in pipeline (for all channels) removed from calculations. The data was taken from a run with forced high gain readout.

4.5.1 Write Clock

The write clock was enabled for two pedestal runs, one with forced high gain readout and one with forced low gain. There was no significant difference in the amplitude measurements with the data when the clock was enabled or disabled. The noise, both RMS deviation and coherent, remained consistent with the baseline data as well, with the exception that there was a higher tail on the RMS deviation distribution. One noticeable effect of the enabling of the write clock was that the first capacitor in the SCA pipeline became noisy (Figure 4.11). When the data from the capacitor

was removed from the calculations, the small bump to the left of the RMS deviation peak vanished. The low gain run demonstrated the same behaviour. There was no observable relationship between the RMS deviation for capacitor 0 and channel, sample, or event number.

4.5.2 Readout Time

The measurable effects of reducing the readout time was an increase in both coherent noise and RMS noise. The results are tabulated in Table 4.1, along with baseline data to illustrate the comparison.

Readout Time μs	*Gain*	*Mean RMS (ADC counts)*	*Mean Coherent Noise (system) (ADC counts)*
4	High	3.4 ± 0.3	0.6 ± 0.1
4	Low	2.9 ± 0.3	0.6 ± 0.2
2	High	3.6 ± 0.4	0.7 ± 0.2
2	Low	3.6 ± 0.9	0.8 ± 0.3

Table 4.1: Summary of noise values for the two runs with the short readout time (Runs 32697 and 32698). The data for the long readout time came from the baseline noise runs taken just prior to the short readout runs (Runs 32689 and 32690).

4.5.3 Reference Subtraction

The most interesting parameter change was the reference subtraction circuit. For the high gain runs there were three cells (193, 223, and 238) with anomalous amplitude values in addition to the original three (31, 73, and 178 (refer to section 4.2)) for the data with the circuit enabled (Figure 4.12). For the low gain data, one cell, 136, behaved anomalous in addition to cell 84 from the baseline data. The mean of the

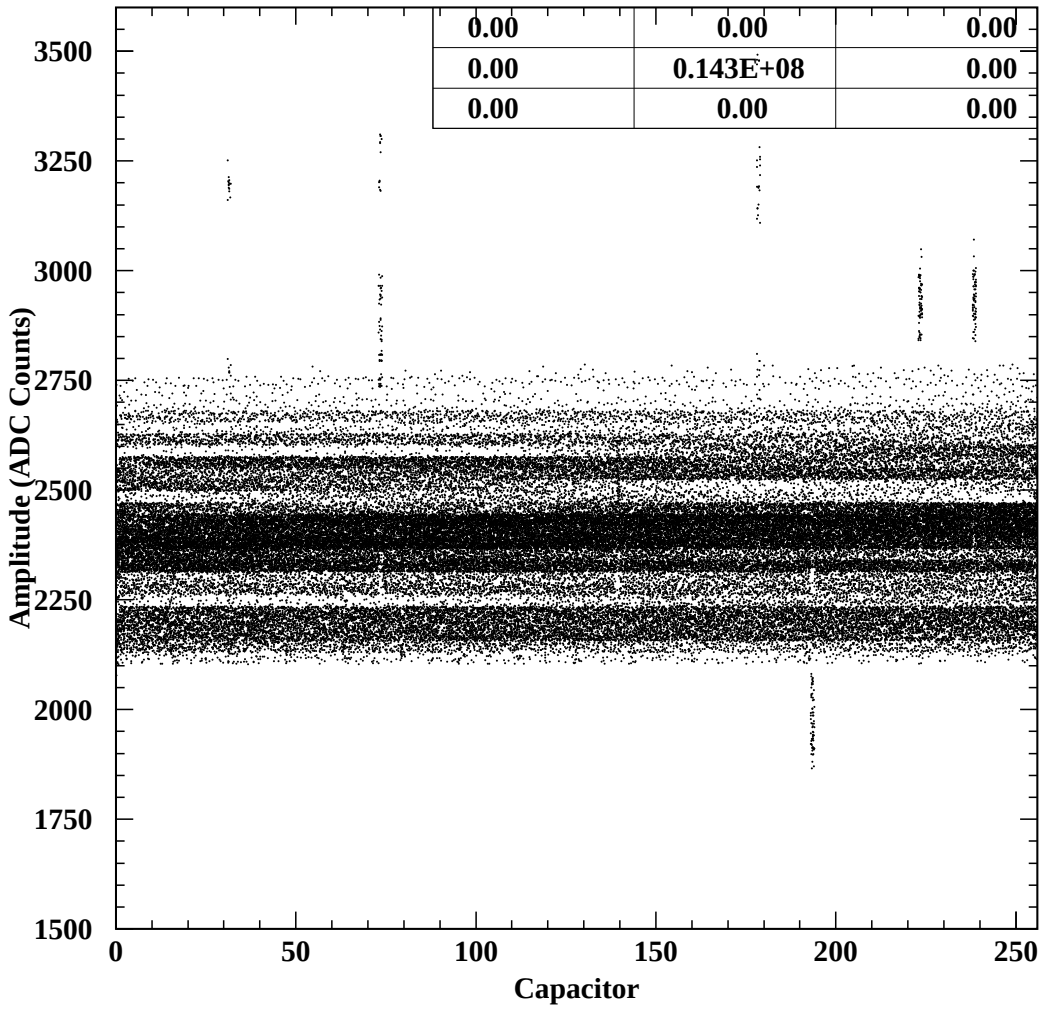

Figure 4.12: Amplitude (in ADC counts) vs cell number. The data was taken from a run with forced high gain readout.

average (over events) amplitude distribution was slightly lower, at (2390 $\pm$ 50) ADC counts (Appendix B), than the baseline runs at (2550 $\pm$ 40) ADC counts. Figure 4.13 illustrates the mean amplitudes plotted against each variable (channel (a), capacitor (b), and sample (c)). The plot of average amplitude versus channel (Figure 4.13 (a)) shows that the average amplitude increased with channel number. This behaviour was not observed for the data taken with the reference subtraction circuit enabled (Figure 4.4 (a)). The pattern of average amplitude decreasing with capacitor for data with the reference subtraction enabled (Figure 4.4 (b)) was not present for the data with the circuit enabled (Figure 4.13 (b)). A trend where the amplitude increased with capacitor number was however observed. The alternating average amplitudes for different samples (Figure 4.13 (c)) varied by more than twice as much as the case with the reference subtraction circuit enabled. Section 4.7 contains a discussion of the effects of this parameter.

Figures 4.14 and 4.15 show that a significant amount of noise was measured when the reference subtraction circuit was disabled. The additional noise did not depend on capacitor or sample but a board dependence was observed. The five highest points in the average noise versus channel corresponded to the last channel on each board. The trend of reduction in average noise as a function of capacitor number, which was observed for the data taken with the reference subtraction circuit enabled, (Figure 4.7 (b)) was not present in the data taken with the reference subtraction circuit disabled. The coherent noise across channels demonstrated no dependence on capacitor or sample and exhibited a similar secondary peak as was observed in the total noise distribution (Figures 4.16 and 4.17). When the dispersion* was summed for each event, it was evident (Figure 4.18) that approximately 3% of the events accumulated ADC counts which formed a distribution about 4500 ADC counts

*While dispersion is defined as the square of the difference between a measurement in a distribution and the mean value of the distribution, it refers to simply the difference here.

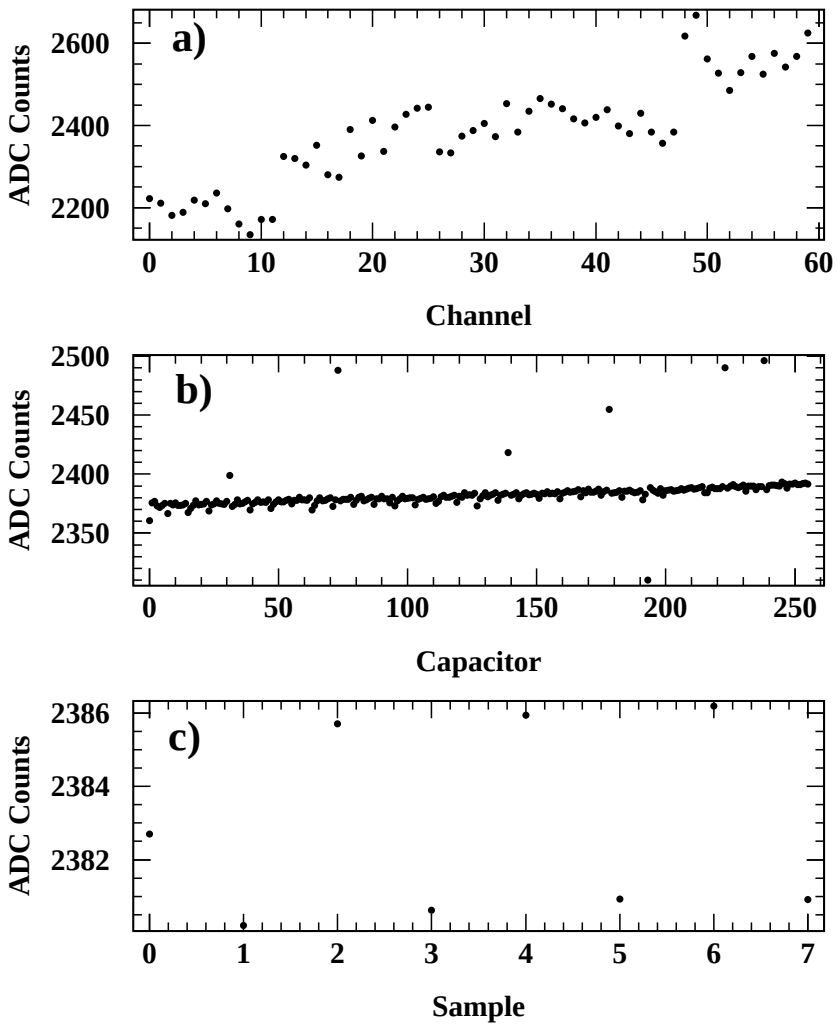

Figure 4.13: Average RMS noise plotted against the three independent variables, channel (a), capacitor (b), and sample (c). The data was taken from a run with forced high gain readout and reference subtraction circuit disabled (Run 32883).

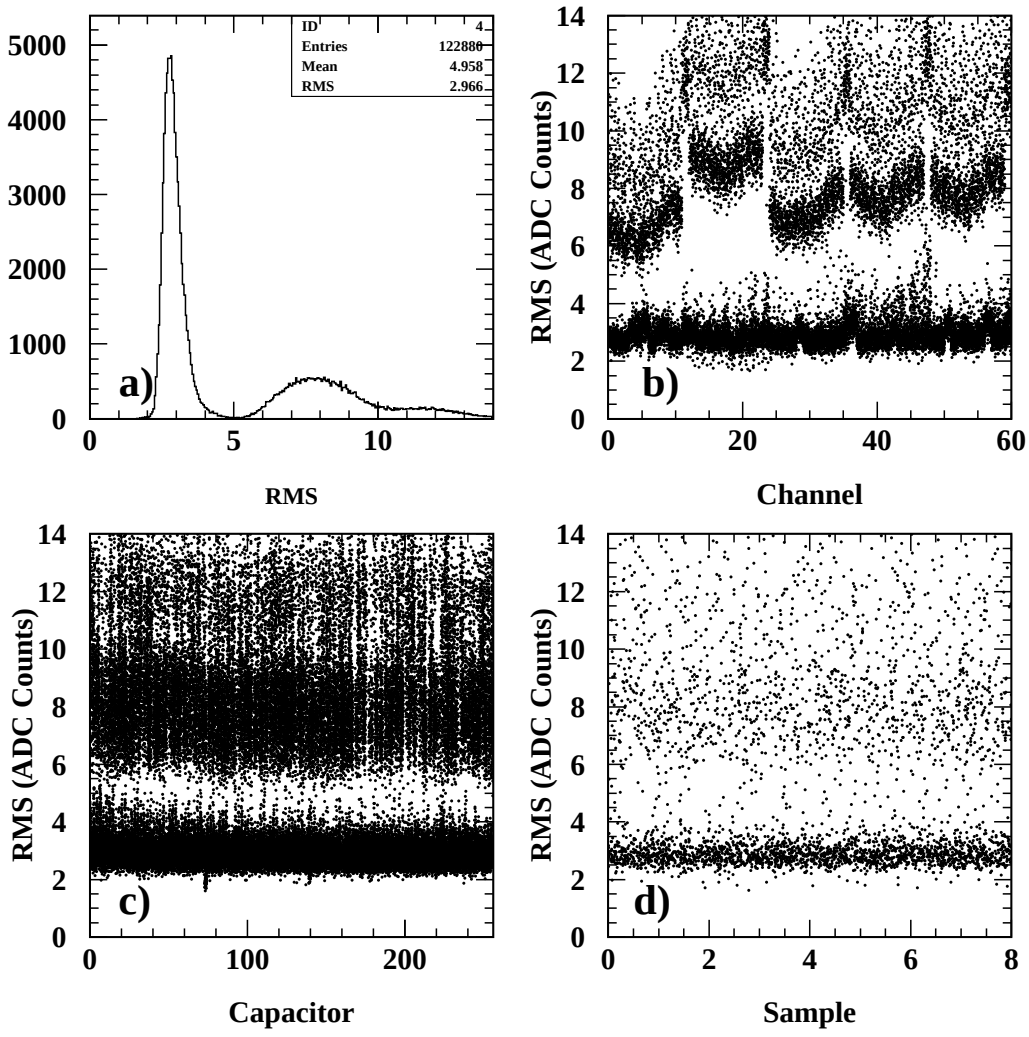

Figure 4.14: RMS noise plotted against channel (b), capacitor (c) and sample (d) for data with the reference subtraction circuit disabled. The data was taken from a run with forced high gain readout (Run 32883).

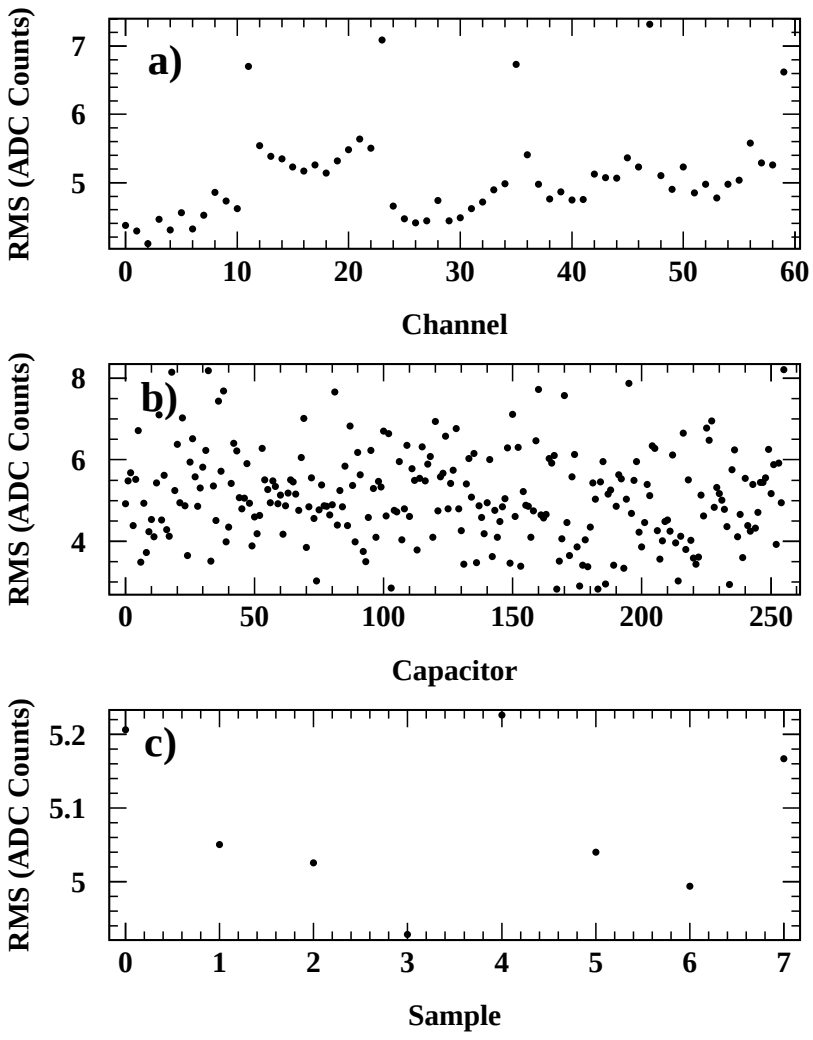

Figure 4.15: Average RMS noise plotted against the three independent variables, channel (a), capacitor (b), and sample (c). The data was taken from a run with forced high gain readout and the reference subtraction circuit disabled (Run 32883).

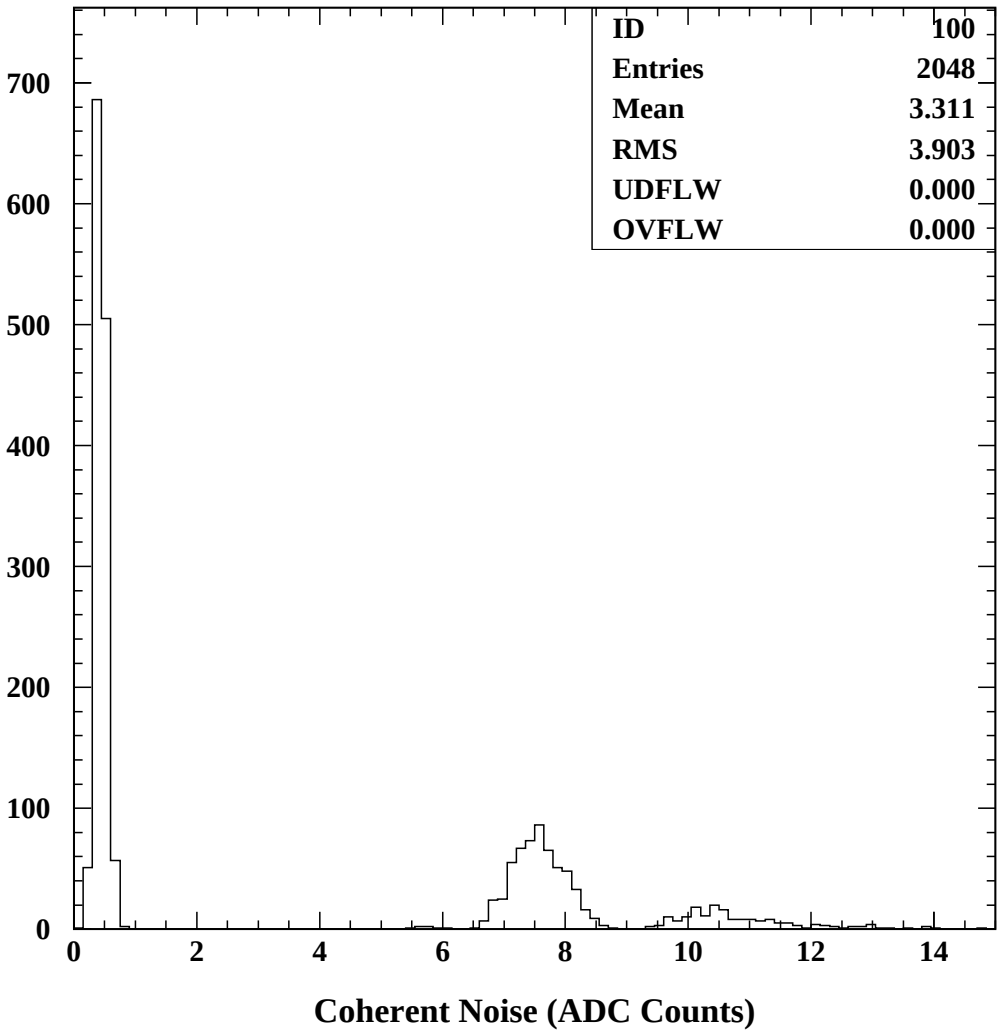

Figure 4.16: The coherent noise across channels for the entire system (all five boards) with the reference subtraction circuit disabled. The data was taken from a run with forced high gain readout (Run 32883).

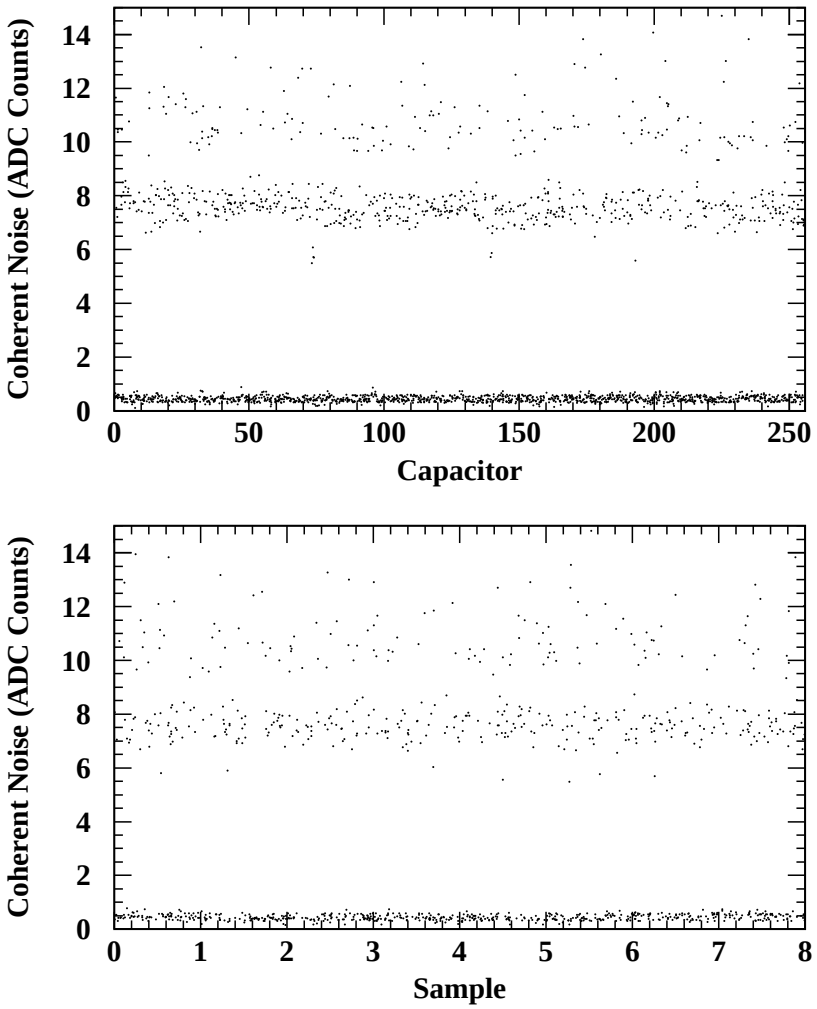

Figure 4.17: The coherent noise as a function of capacitor and sample with the reference subtraction circuit removed. The data was taken from a run with forced high gain readout (Run 32883).

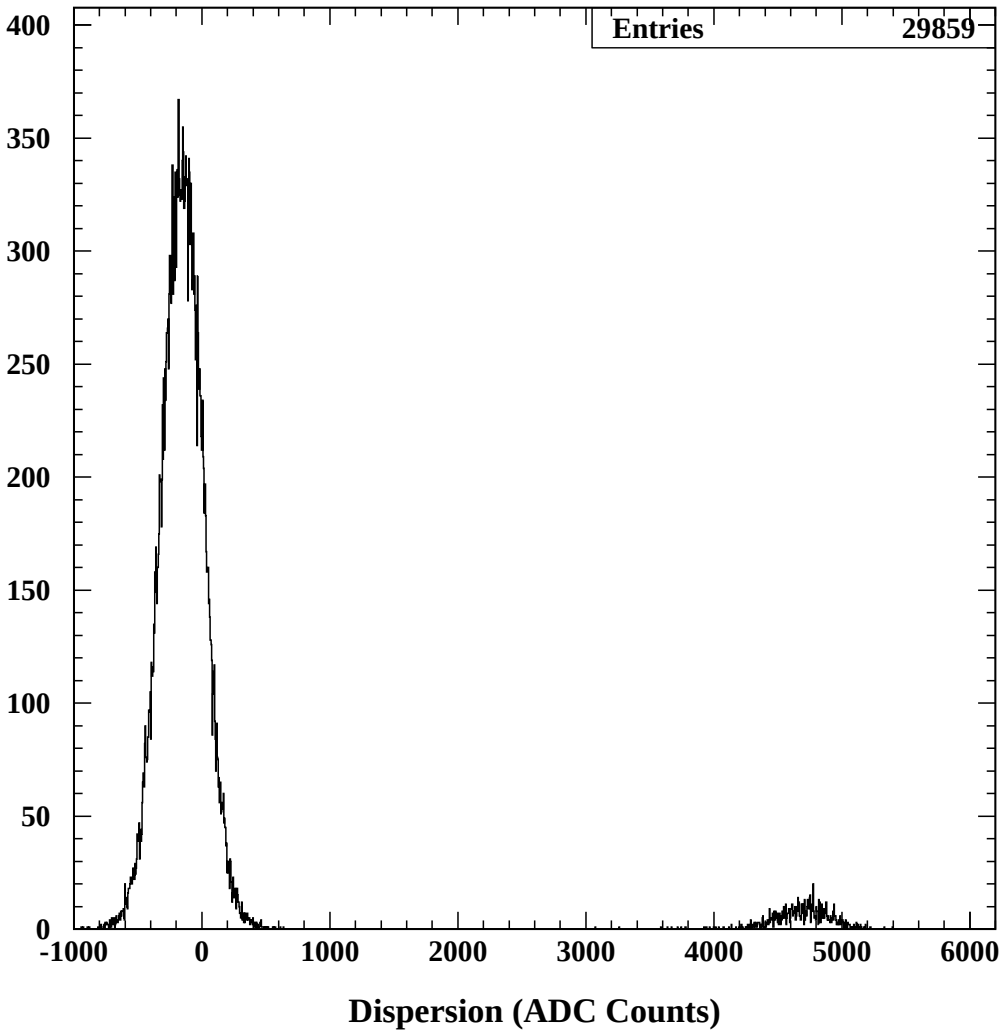

Figure 4.18: Total dispersion summed for each event with the reference subtraction circuit disabled. The data was taken from a run with forced high gain readout (Run 32883).

higher than the distribution centered near zero. The widths of the two peaks were similar (164.2 ADC counts for the left peak and 217.2 ADC counts for the right). When the 3% of the events which caused the second peak in Figure 4.18 were not used in noise calculations the second peak vanished in both the RMS and coherent noise plots, as shown in Figure 4.19. The analysis of the data taken with the forced low gain readout produced similar results. All of the noise values for the data taken with the reference subtraction circuit disabled can be found in Appendix B.

4.6 Data Taken at a Single Gain Scale

The analysis for the mono-gain data was performed in precisely the same manner as that of the bi-gain data. There were four mono-gain noise runs taken. For each run the operating conditions were set as follows: readout time of 4 μs, reference subtraction enabled, and write clock off. All data was read out after a 575 ns trigger delay.

The ADC counts were examined and the distribution had a mean of (2560 ± 40) counts. The noise was slightly higher than either the high or low gain runs at (4.0 ± 0.4) ADC counts compared to (3.4 ± 0.3) ADC counts for the high gain data and (3.0 ± 0.3) ADC counts for the low gain data. The coherent noise also increased to (0.8 ± 0.1) ADC counts. The mono-gain runs are summarized in Appendix B. As there was additional multiplexing used to read out both the high and low gain channels at the same time, additional noise could have been added. There could have been noise associated with the different preamplifiers and shapers used in that portion of the calorimeter as well.

For the mono-gain data the same capacitors and channels were considered

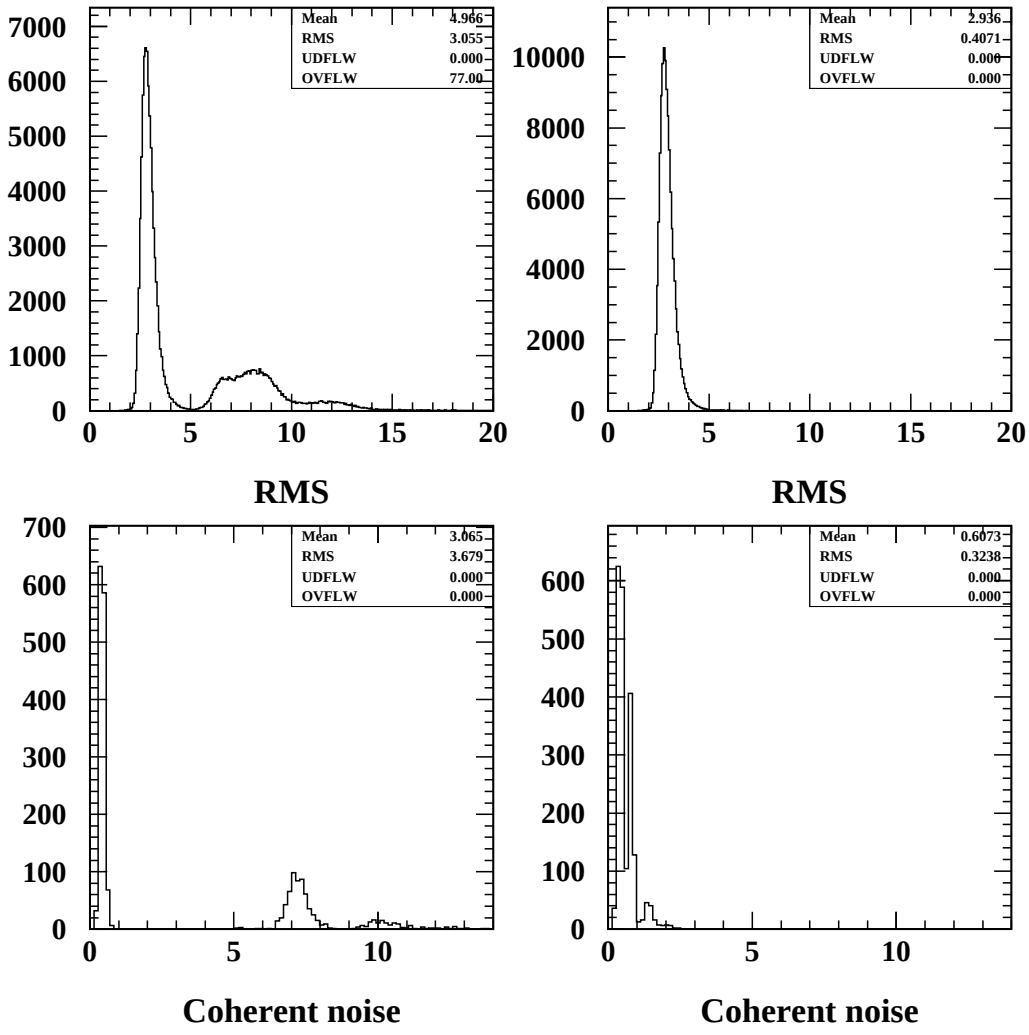

Figure 4.19: Noise for no data where the reference subtraction circuit was disabled. Top: RMS before and after removing events. Bottom: Coherent noise before and after removing events (Run 32883).

noisy as for each of the high and low gain runs. There was little variation in either amplitude or noise measurements between the four runs.

4.7 Discussion of System Noise Studies

4.7.1 Basic System Operation

There were no permanent system malfunctions to prevent a complete analysis of the data. The few capacitors which gave measured amplitudes that differed significantly from the others did so in each channel. These capacitors did not exhibit higher RMS or coherent noise than the other capacitors. If the amplitude measurements from the capacitors was lower than expected, it can be imagined that they weren't completely discharged during readout. The additional ADC counts measured on the few anomalous capacitors could not be explained. The last channel on each board was characteristically "noisier" than the others (Figure 4.7). These channels were located on the edge of the ADC chip nearest to the addressing lines where digital addressing noise could have been introduced. The data corresponding to the noisy capacitors and channels were removed from the calculations and produced no measurable improvement on the average noise values. All results presented in this thesis contain all data unless explicitly stated otherwise.

While there were fluctuations in both amplitude and noise values between different capacitors and channels, there was no significant variation in either amplitude or noise with time sample. The trend of average amplitude and average total noise oscillation with time sample was observed for all data. One plausible explanation was that the oscillations were caused by the two sample and hold circuits illustrated in Figure 3.8. Each channel shared a pair of the sample and hold circuits and any

variation between the two circuits could have caused the observed difference.

Since the average amplitudes did not fluctuate beyond an ADC count for different samples, the pedestal files, or files containing mean amplitude values for each channel, cell, and sample, (described in the next section), could be reduced in size by the number of samples by averaging over the sample. While it was not an issue in the analysis performed for this thesis, and in fact $60 \times 256 \times 8 = 122880$ pedestals were made for each pedestal file, it could make a difference at ATLAS where the number of channels will be great and file size may become a factor. For example, the electromagnetic barrel calorimeter will consist of 110208 channels and thus a pedestal calibration file for 5 samples (assuming 14 bits per pedestal) would be approximately 20 megabytes in size. If there was no pedestal fluctuation between samples, this file size could be reduced to 4 megabytes.

The study of coherent noise across boards (Figure 4.9) showed that significant tails in the coherent noise distributions occurred for boards 1 and 3. The RMS noise across boards showed no similar behaviour. An additional peak in coherent noise can be seen for board 3. The data from the low gain readout contained the same features for the two boards. As the different gain readout channels did not share SCA chips (section 3.4), the coherent noise could not have been introduced in the SCA chips.

4.7.2 Variation in Operating Conditions

Disabling the reference subtraction circuit had the greatest effect of the three operating conditions which were varied, although there were smaller effects from the other two operating conditions. Enabling the write clock introduced a tail on the high side of the RMS distribution and caused the first capacitor in each pipeline to become noisy. As the capacitor was noisy for all channels on both the high and low gain

electronics chains, the problem could have been with the addressing circuitry which was shared between chips. It was also possible that the additional clock could have illuminated a problem common to the SCA chips.

The additional noise introduced with the reduced readout time could be explained as follows. Reading out a capacitor involved charging an operational amplifier up to the voltage across the capacitor. The response of an operational amplifier is such that following the rise of input voltage there is an overshoot followed by damped ringing [21][23]. The reduced readout time of 2 μs could conceivably have caused the readout to occur at the point where there was ringing, causing an increase in measured noise.

The data taken with the reference subtraction circuit disabled contained a number of events (approximately 3%) which on average had total noise values more than twice those of the other 97% of the events. The coherent noise values for these events was an order of magnitude higher. As these events were scattered throughout the data in no particular pattern, no conclusions about their existence could be drawn. When the events were removed the mean amplitudes and RMS values were reduced (Appendix B), while the coherent noise was slightly increased. The increase in coherent noise was to be expected as without subtraction of the reference channels there would be coupling between channels. The reduction in mean amplitude was likely due to the changing of the reference voltage from that in the reference channels to voltage provided directly at the subtraction part of the circuit as described in section 3.4.3. The lower values of RMS noise seem to indicate that the reference subtraction circuit itself introduced noise into the system.

4.7.3 Mono-gain System

The data taken with a single gain scale had mean amplitude values which differed from the bi-gain system. The gain applied to the signals prior to the FEB were not precisely the same for the two systems. The RMS and total noise increased which could be attributed to either the multiplexing of the data into the ADCs or the mono-gain preamplifiers and shapers.

4.8 Studies Using Calibration Data

The noise studies thus far have involved the system operating with no input signals. It was also beneficial to study the system as it was pulsed with well defined signals, in both time and amplitude. This procedure allowed an examination of the response of the front-end electronics to voltage signals as well as a cross-talk study*.

4.8.1 Determination of Pedestals

Pedestals (average ADC counts with no input signal) for each channel, capacitor, and sample and for each set of operating conditions were required for the analysis of calibration and electron data. The pedestals would be subtracted off of the ADC values, leaving only the signals. When the pedestals were calculated, the main concern was to have a suitable mean for each channel, capacitor and sample which was not skewed by out-liers†. To achieve this, any tails on the individual ADC count distributions were truncated. Each of the $60\times256\times8$ distributions had a different mean and the

*Cross-talk is the noise caused in one channel due to the signal in another channel in close proximity to the first.

†An out-lier is a measured value which lies several standard deviations from the mean value and is clearly not part of the distribution.

dispersion was used to truncate all mean amplitude distributions simultaneously. Examining the dispersion distribution, centred on zero, provided a guide for cutting the tails. Once a cut was imposed, events contributing to the distribution out of the cut range were discarded. The cut was adjusted until roughly 3% (or 1000) of the events were discarded. The importance of this value was that it maintained good statistics for the pedestals. A typical reduction in the mean of hits per capacitor (refer to Figure 4.1) was from 120 to 110 hits (or 8%).

4.8.2 Method of Calibrating the System

For calibration, pulses with well defined shape were injected into the calorimeter onto the electrodes as described in section 2.3.6. As outlined in Appendix C, channels were pulsed in 12 specific groupings, or patterns, of channels (4 groups for the mono-gain data). This was to allow an analysis of the cross-talk. The runs used in the calibration studies, and the settings for each, are included in Appendix A.

The procedure for analyzing the pulser data follows in the next section. The calibration pulses were generated by a 16-bit digital to analog (DAC) pulse generator, or pulser. The error in a particular pulser output setting was then taken to be 2^{-16} DAC units (or essentially negligible). Gain selection in the calibration runs included, along with forced high gain and forced low gain, and automatic gain selection (as described in section 3.4).

In order to measure the voltage of each pulse, a parabolic fit was made to the ADC count versus sample data. This parabola was a good approximation to the pulse and the maximum of this fit was then taken to be the voltage of the pulse. A full explanation and description can be found in section 5.2.1.

4.8.3 Description of Calibration Data

The calibration data was divided into 20 discrete pulser voltage settings. Within each of the 20 settings, each of the channel patterns was pulsed for 50 events. As each calibration run contained 12000 events, the pulser voltage changed every 12000/20, or 600 events. One event immediately preceding and immediately following each voltage change was discarded as there appeared to be noise associated with the pulser at these points.

The pulsing of the mono-gain shapers used only 4 patterns (Appendix C) as opposed to the 12 for bi-gain shapers. There were still 20 DAC settings and 50 events per pattern, however, only one third of the events contained pulses.

The data taken at the beginning of the running period was not used as the calibration pulser was improperly set. No data was therefore analyzed with the 2 μs readout time. The pulser was incorrectly set for the low gain data for a longer period and as the problem was not discovered until after the test period, no low gain data was analyzed with the write clock enabled.

4.9 Linearity and Dynamic Range of the System

As the physics at the TeV energy scale gives a wide range of energies and the system described in this thesis was based on the ATLAS readout system, it was important to measure the dynamic range of the system. The dynamic range described here refers to bit resolution. This is slightly different than the range of energy measured (which is described in the following chapter). Dynamic range in bits gives a measure of the range and resolution of the system. This value can then be compared with the maximum size in bits of the ADC's used. The linearity of the system was equally

important and also determined. As can be seen by Figure 4.20* the linearity and dynamic range were not independent of each other. There was a tradeoff between dynamic range and linearity. The majority of the channels did not show nonlinear behaviour beyond 0.3%. There were 8 channels however, (37 - 43) which were non-linear in the low gain chain and 3 (16, 18, and 19) in the high gain chain. Gain switching (described in section 3.4.2) occurred before the full dynamic range could be covered and the non-linear regions of the high gain system were never used in either the measurement of electron energy (the 300 GeV electrons utilized only approximately 50% of the dynamic range of the high gain system prior to switching gain) or pulser data in automatic gain switching mode.

The linearity of a channel was determined by examining residuals (deviations of the data points from a linear fit to the data) of the output versus input of the system. The non-linearity, which was defined as

$$L = \frac{\Delta V}{V_{\mathrm{MAX}}} \cdot 100, \tag{4.10}$$

where ΔV was the maximum residual for a particular channel, and V_{MAX} was the maximum range of the output signal (9.17 V). There was a linearity measurement for each channel, but the average value of all channels was used here to describe the entire system.

4.9.1 Gain Switching

To determine the dynamic range of the system, the amplitude where the gain switched was determined. At the amplitude where the gain changed, the output dropped and

*Because the plots used in this section refer to amplitudes of the signals prior to digitization, they are entirely positive. The actual signal range going into the analog to digital converters was -4.36 V to 4.81 V as shown in Figure 3.9. It should also be noted that the pedestals have been subtracted from the data.

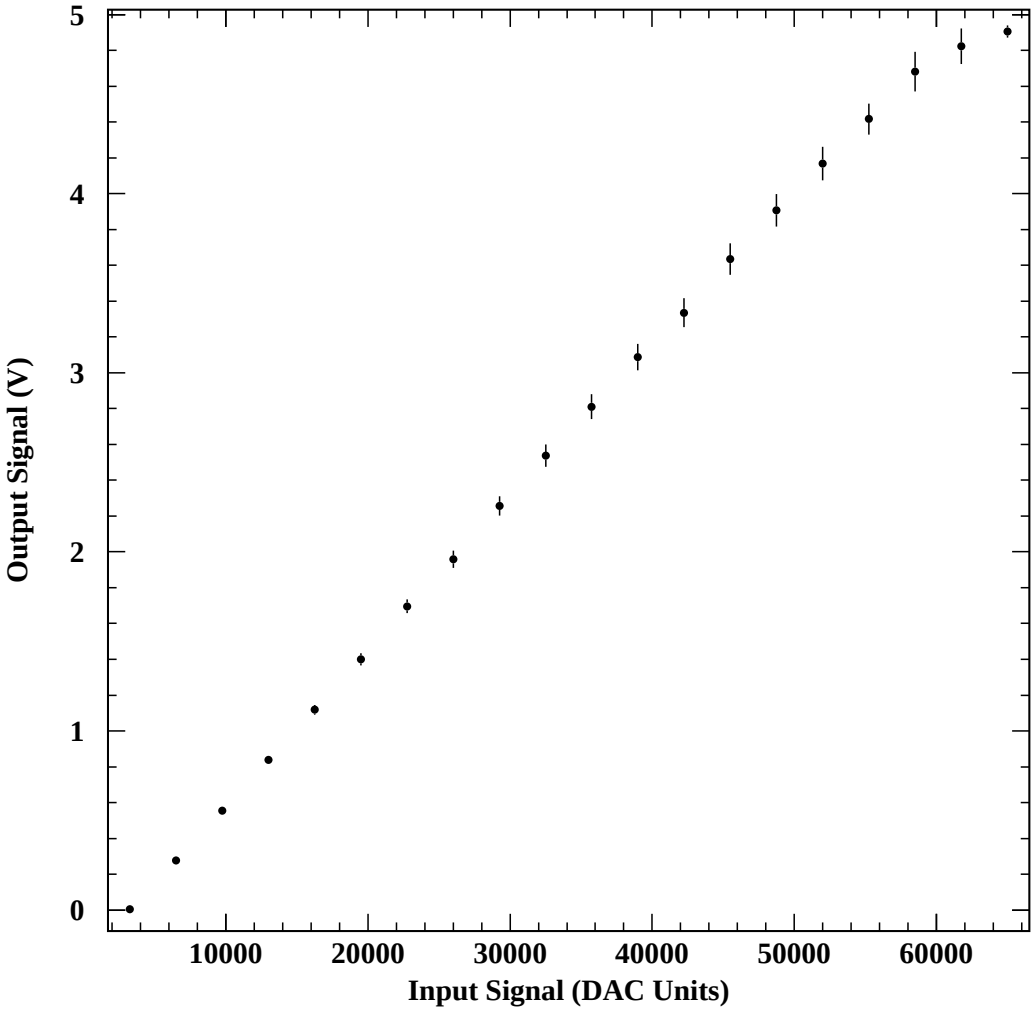

Figure 4.20: System response to calibration signals (for channel 39). Non-linear behaviour appears for last few settings. Data taken with forced low gain readout (Run 32869).

the slope of the plot changed as shown in Figure 4.21.

Ideally, the gain switch would have occurred in a single discrete jump at the voltage threshold. As can be seen by Figure 4.21, the switching process was not a single jump. The large error bar on the fourth setting was due to a combination of high and low gain data being selected throughout the DAC setting (Figure 4.22). The top plot in Figure 4.22 shows the output signal for the setting following the gain switch while the bottom plot shows the output for the DAC setting where the gain switched. Figure 4.23 demonstrates that there was no single point during the DAC setting where the gain switch occurred. A possible cause of the problematic gain switching was a time jitter in the pulses from the calibration pulser, as illustrated in Figure 4.24. The time jitter could have caused the pulses to "slide" backward and forward in time. This would cause the maximum amplitude measured at the fixed sample point to increase or decrease depending on the direction of the time jitter. If the original amplitude (prior to jitter) was close to the threshold voltage, it would have moved above or below the threshold causing the observed gain switching. Unfortunately it was not possible to work back to determine the amount of time jitter which existed, as there was insufficient information. The data taken with a 575 ns trigger delay had more than one DAC setting switching due to the 25 ns shift of the pulse.

The dynamic range of the bi-gain system was taken to be that of the low gain system with the understanding that prior to the gain switch the resolution would be slightly worse. The dynamic range for a channel, R_{Chan}, was defined as:

$$R_{Chan} = \frac{V_{\mathrm{MAX}} - V_{\mathrm{MIN}}}{V_{\mathrm{RMS}}}, \tag{4.11}$$

where V_{RMS} was the measured RMS noise (in volts) of the system. Any amplitude measurement was only accurate to within the RMS of the measurement and thus the

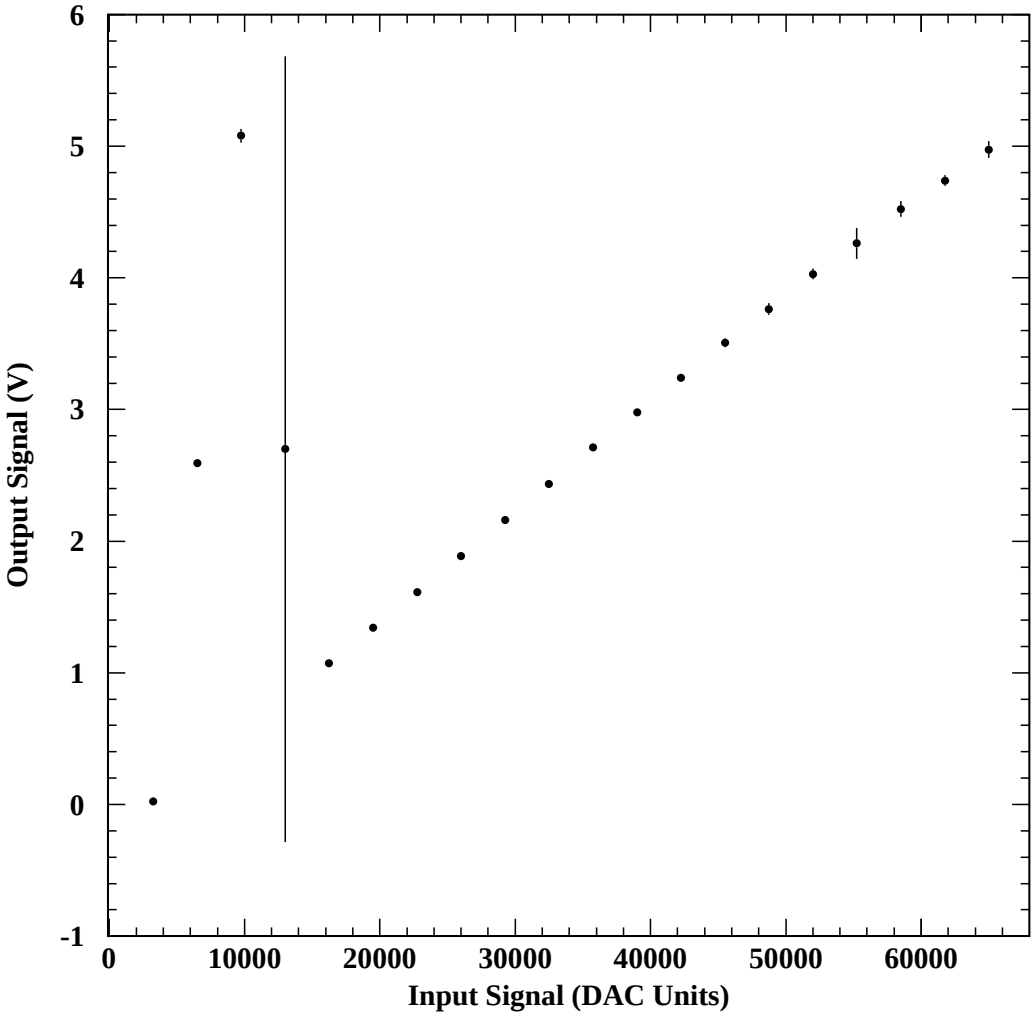

Figure 4.21: Response plot for automatic gain switching data run (32909 - Channel 5). The large error bar on the fourth data point was due to gain switching at the fourth DAC setting.

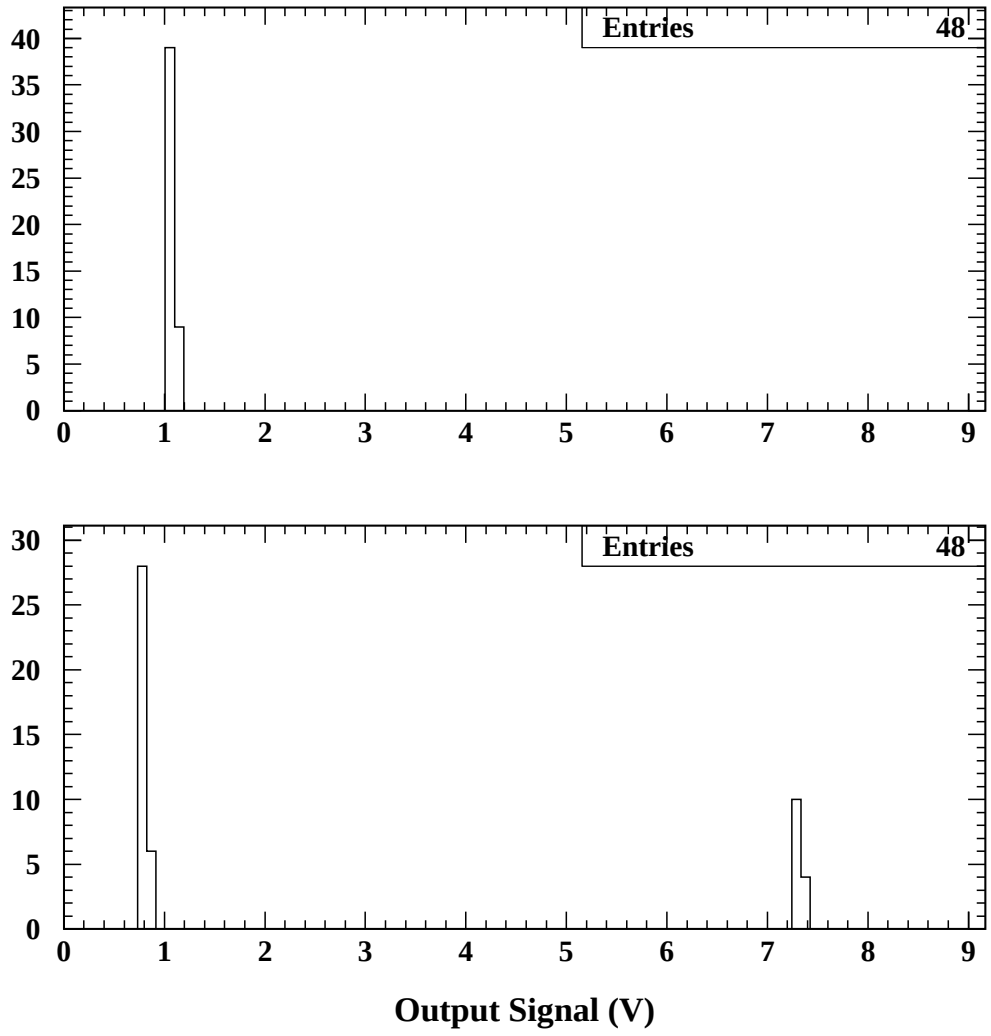

Figure 4.22: Output signals for the fifth (top) and fourth (bottom) DAC settings. Gain switching occurred during the fourth setting. The data was taken from run 32909 and channel 5.

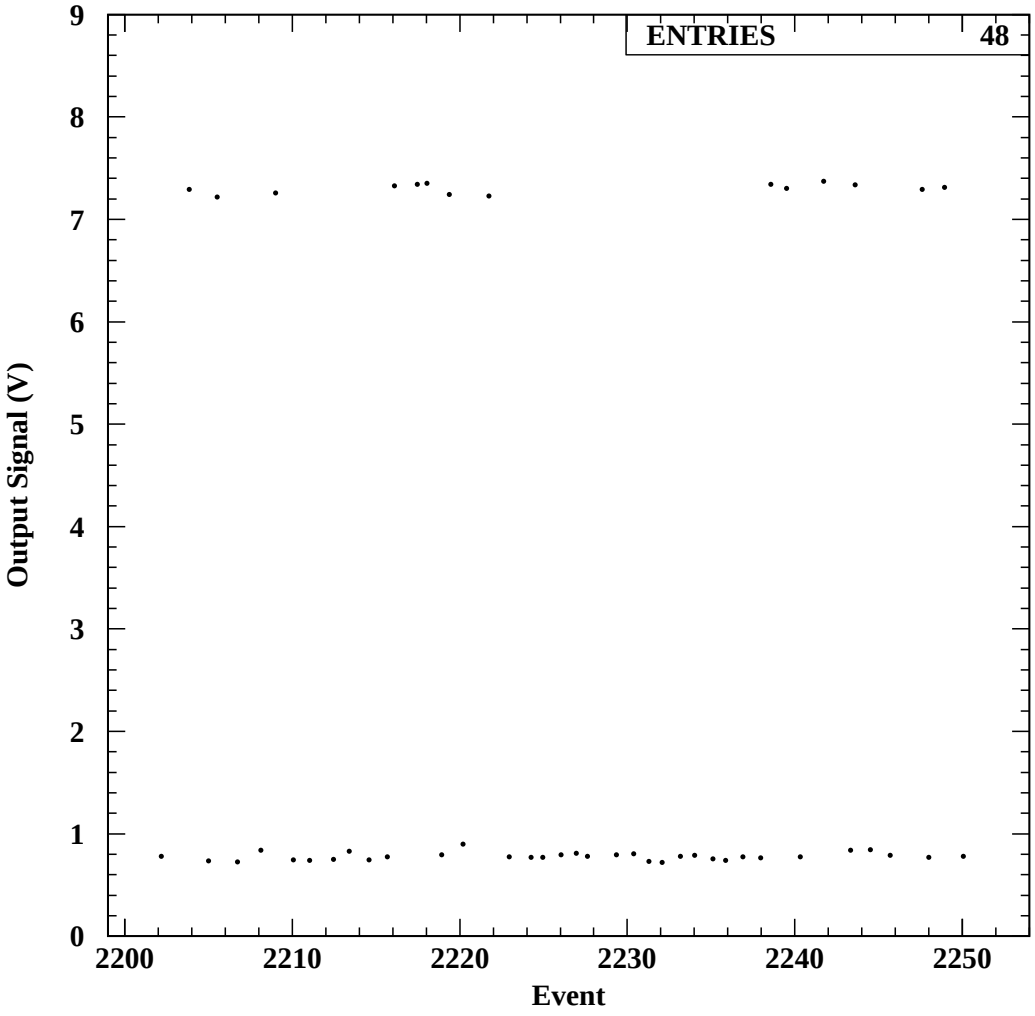

Figure 4.23: Output signals for each event in the fourth DAC setting. The data was taken from run 32909 and channel 5.

dynamic range was reduced by a factor of $\frac{1}{V_{\mathrm{RMS}}}$. All references to the system dynamic range in this thesis are made to the channel with the smallest dynamic range. The channel with the smallest dynamic range was 1% to 2% lower than the mean dynamic range of all channels.

Tables 4.2 and 4.3 contain the linearity and dynamic range measurements for the high and low gain pulser data respectively. Three dynamic ranges were tabulated for the high gain data, the full range, the range ending just above the maximum energy (12 DAC settings), and the range ending where the gain switched (3 DAC settings). The data taken with the reference subtraction circuit disabled was as linear as the other data, but the dynamic range was noticeably less. This was due to (as described in section 4.5.3) the high RMS noise of this data (2.8 mV as opposed to 2.0 mV for data with the circuit enabled).

The low gain data was examined over the entire dynamic range and the output versus signal curve truncated to allow measurement of linearity with reductions in dynamic range (Figure 4.25).

The dynamic range was less for the low gain channels but the resolution was better as it was defined by

$$\lambda = \frac{ADC_{MAX} - ADC_{RMS}}{g}, \tag{4.12}$$

where ADC_{MAX} was the maximum ADC value of the system, ADC_{RMS} was the RMS, and g was the relative gain*. This demonstrated the trade-off between obtaining a wide range of measurement and losing resolution in the process.

*The low gain system had a unit gain while the high gain system had a gain greater than one. This is the convention that is used in the discussion of quantities involving g.

Run	*Clocks*	*Reference Subtraction*	*Settings Cut*	*Dynamic Range* (Bits)	*Linearity (% Full Range)*
32687	Off	Yes	0	11.71 ± 0.07	1 ± 1
			8	10.94 ± 0.08	0.1 ± 0.1
			17	8.40 ± 0.09	0.010 ± 0.003
32728	Off	Yes	0	11.71 ± 0.07	1 ± 1
			8	10.94 ± 0.08	0.1 ± 0.1
			17	8.40 ± 0.09	0.012 ± 0.004
32738	Off	Yes	0	11.70 ± 0.06	1 ± 1
			8	10.94 ± 0.08	0.2 ± 0.2
			17	8.40 ± 0.09	0.013 ± 0.003
32695	On	Yes	0	11.71 ± 0.06	1 ± 1
			8	10.94 ± 0.08	0.1 ± 0.1
			17	8.41 ± 0.09	0.011 ± 0.003
32870	Off	Yes	0	11.59 ± 0.09	1 ± 1
			8	10.9 ± 0.1	0.2 ± 0.2
			17	8.3 ± 0.1	0.018 ± 0.006
32912	Off	Yes	0	11.60 ± 0.09	1.0 ± 0.7
			8	10.8 ± 0.1	0.2 ± 0.2
			17	8.3 ± 0.1	0.019 ± 0.006
32764	Off	No	0	11.19 ± 0.07	1 ± 1
			8	10.44 ± 0.08	0.12 ± 0.09
			17	7.8 ± 0.1	0.011 ± 0.004
32884	Off	No	0	11.08 ± 0.09	1.0 ± 0.6
			8	10.3 ± 0.1	0.2 ± 0.2
			17	7.7 ± 0.1	0.018 ± 0.006

Table 4.2: Summary of dynamic range and linearity for data taken with forced high gain readout (Run 32912). Settings cut refers to the number of voltage settings truncated off of the upper end of the range.

Run	*Reference Subtraction*	*Settings Cut*	*Dynamic Range* (Bits)	*Linearity (% Full Range)*
32726	Yes	0	11.27 ± 0.07	1.1 ± 0.9
		1	11.23 ± 0.06	0.7 ± 0.7
		2	11.20 ± 0.06	0.4 ± 0.4
		3	11.12 ± 0.06	0.2 ± 0.3
		4	11.04 ± 0.06	0.1 ± 0.1
32739	Yes	0	11.30 ± 0.07	1 ± 1
		1	11.23 ± 0.06	0.8 ± 0.8
		2	11.21 ± 0.06	0.4 ± 0.5
		3	11.13 ± 0.06	0.2 ± 0.2
		4	11.04 ± 0.06	0.11 ± 0.08
32869	Yes	0	11.3 ± 0.1	0.9 ± 0.5
		1	11.2 ± 0.1	0.8 ± 0.4
		2	11.1 ± 0.1	0.6 ± 0.3
		3	11.0 ± 0.1	0.4 ± 0.2
		4	10.9 ± 0.1	0.3 ± 0.2
32911	Yes	0	11.3 ± 0.1	0.9 ± 0.5
		1	11.2 ± 0.1	0.6 ± 0.4
		2	11.1 ± 0.1	0.5 ± 0.3
		3	11.0 ± 0.1	0.3 ± 0.2
		4	10.9 ± 0.1	0.3 ± 0.2
32885	No	0	10.8 ± 0.1	0.9 ± 0.6
		1	10.7 ± 0.1	0.8 ± 0.4
		2	10.6 ± 0.1	0.6 ± 0.3
		3	10.5 ± 0.1	0.4 ± 0.2
		4	10.4 ± 0.1	0.3 ± 0.2

Table 4.3: Summary of dynamic range and linearity for data taken with the forced low gain readout (Run 32911).

4.9.2 Data Taken at a Single Gain Scale

The four mono-gain data files were analyzed for linearity and dynamic range in the same manner. The linearity is shown in Figure 4.27.

The non-linear behaviour occurred for all channels, as opposed to the few for the bi-gain data. When the four highest DAC settings were removed, the majority of the channels were linear to better than 0.3%. Eleven channels (80, 82, 83, 88, 89, 90, 91, 92, 93, 94, and 95), still exhibited non-linear behaviour after these truncations. Only after truncating 5 more DAC settings (9 total) did the system as a whole achieve the linearity comparable to the bi-gain system. For the last few DAC settings, from the 13th onward, the measured output signal distributions began to fragment (Figure 4.27). There was no pattern, in time, to the deviating values causing the wider distributions. All four of the mono-gain calibration files exhibited the same behaviour, which ruled out the possibility of an anomalous run.

4.10 Estimation of Cross-talk

Cross-talk can occur in circuits which use high density printed circuit boards when signals in one trace produce smaller signals in nearby traces. A signal in one trace on a circuit board can cause smaller, yet significant, signals in a neighbouring trace. On the front-end board a signal in one channel could cause the channels in close proximity to carry a cross-talk signal due to the mutual inductance and capacitance. The same is true for adjacent cells in the calorimeter. Driving electrodes in the calorimeter with well defined signal pulses allows the measurement of cross-talk.

The cross-talk was measured by looking at the neighbouring channels* during the events where a particular group of channels was continuously pulsed (Appendix C). The cross-talk between channels caused a pulse to appear as pulses in the other channels. The pulses did not however have the same shape as those generated by the pulser. As can be seen in Figure 4.29, the majority of pulses, due to cross-talk, had their maximum amplitudes in the second time sample, which was the same sample which contained the original pulse maximum. The majority of the pulses with maxima in sample two also had negative amplitudes (compared with the positive amplitude of the pulser signals), while those with a maximum in other samples had, for the most part, positive amplitudes. The cross-talk values used in this thesis were the maximum amplitudes of the cross-talk pulses regardless of the particular sample the maximum was in.

Three different patterns were examined for a high gain baseline run and the results tabulated. Table 4.4 contains the cross-talk amplitudes for the channel pattern where 2 cells in the back layer of the calorimeter were pulsed. Appendix D, contains the maximum cross-talk amplitudes of the three channel patterns discussed in this thesis. No channel patterns were pulsed in either the front or middle layers separately.

When the back layer of the calorimeter was pulsed, a cross-talk amplitude above RMS (Table 4.5) was found for a channel, 11, in the front layer (and on a different board) for input signals above 5 V. A similar result was observed for other channels as well as the low gain data. For all of the data with the reference subtraction circuit enabled, the neighbouring cell(s) in the layer behind or in front of the pulsed cell had a positive amplitude while cells neighbouring in the same layer could have cross-talk with positive or negative amplitudes. There seemed to be no cross-talk

*Neighbouring channels could refer to neighbouring electronics channels on the front-end board, or neighbouring calorimeter cells. The calorimeter cells were mapped to electronics channels such that neighbouring calorimeter cells were also neighbouring electronics channels.

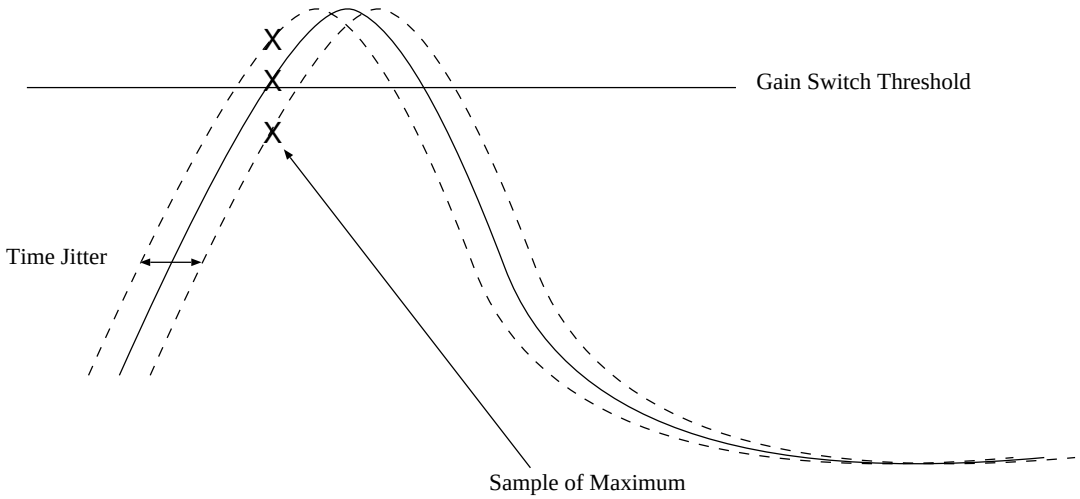

Figure 4.24: The time jitter from the calibration pulser caused erratic gain switching when a maximum lay close to the switching threshold.

$\phi\backslash\eta$	*1*	*2*	*3*	*4*	*5*	*6*
14	-0.0172	-0.0189	-0.0128	-0.0275	-0.0154	-0.0197
13	-0.0183	-0.0209	-0.0126	-0.0341	0.0167	-0.0198
12	-0.0080	-0.0078	-0.0081	-0.0098	-0.0074	-0.0077
11	-0.0099	-0.0077	-0.0086	-0.0081	-0.0072	-0.0057
Front Layer						
14	-0.0054	-0.0000	0.0479	0.0482	-0.0254	-0.0125
13	-0.0069	-0.0082	0.0463	0.0507	-0.0159	-0.0173
12	-0.0028	-0.0033	-0.0007	-0.0010	-0.0005	-0.0027
11	-0.0012	-0.0035	-0.0027	-0.0017	0.0010	-0.0005
Middle Layer						
14	-0.1119		6.9631		-0.1767	
13	-0.1482		7.1014		-0.1477	
12	-0.0144		-0.0303		-0.0192	
11	-0.0134		-0.0297		-0.0171	
Back Layer						

Table 4.4: Cross-talk (volts) in η and ϕ for the bi-gain shapers. Channels 55 ($\eta = 2$,$\phi = 14$) and 57 (2,13) in the back were pulsed (pattern 0).

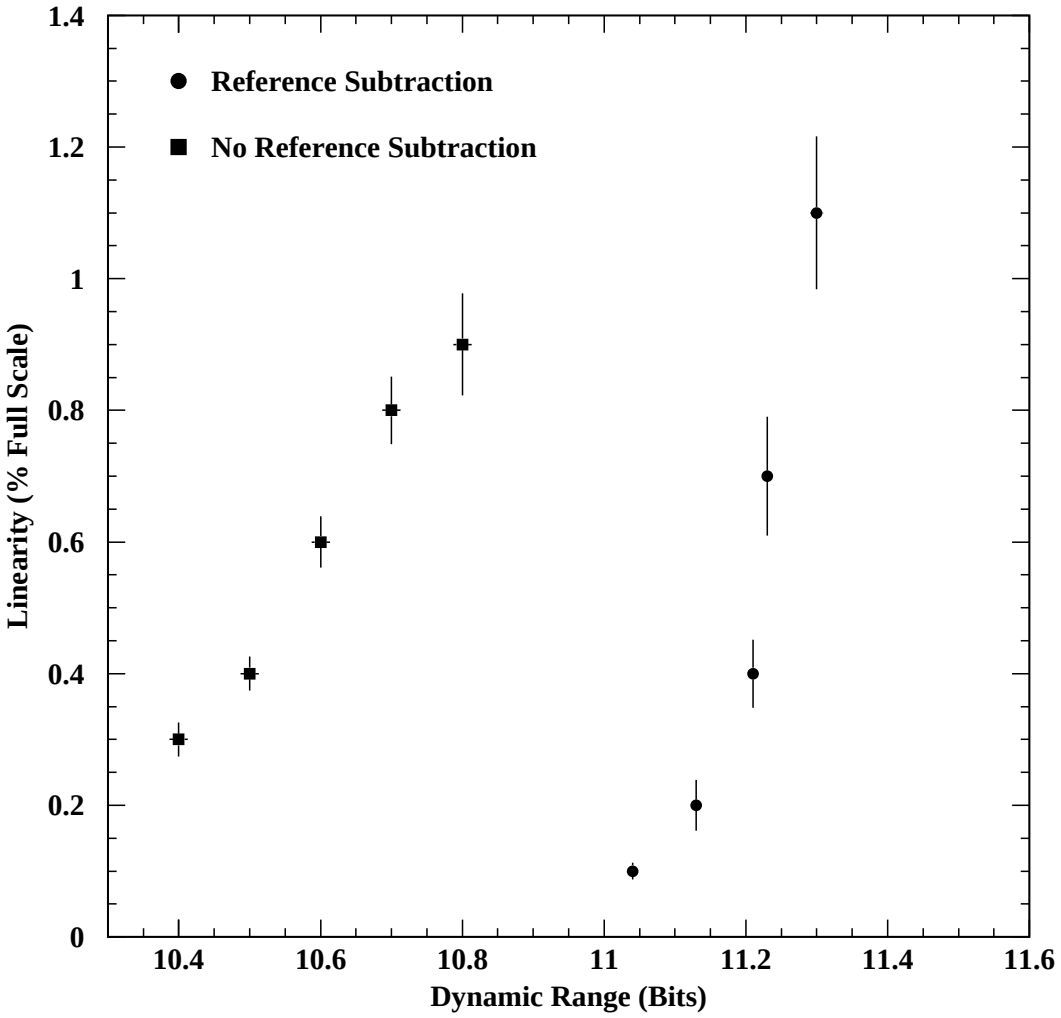

Figure 4.25: The linearity of the system as a function of dynamic range, which was being truncated from the upper range.

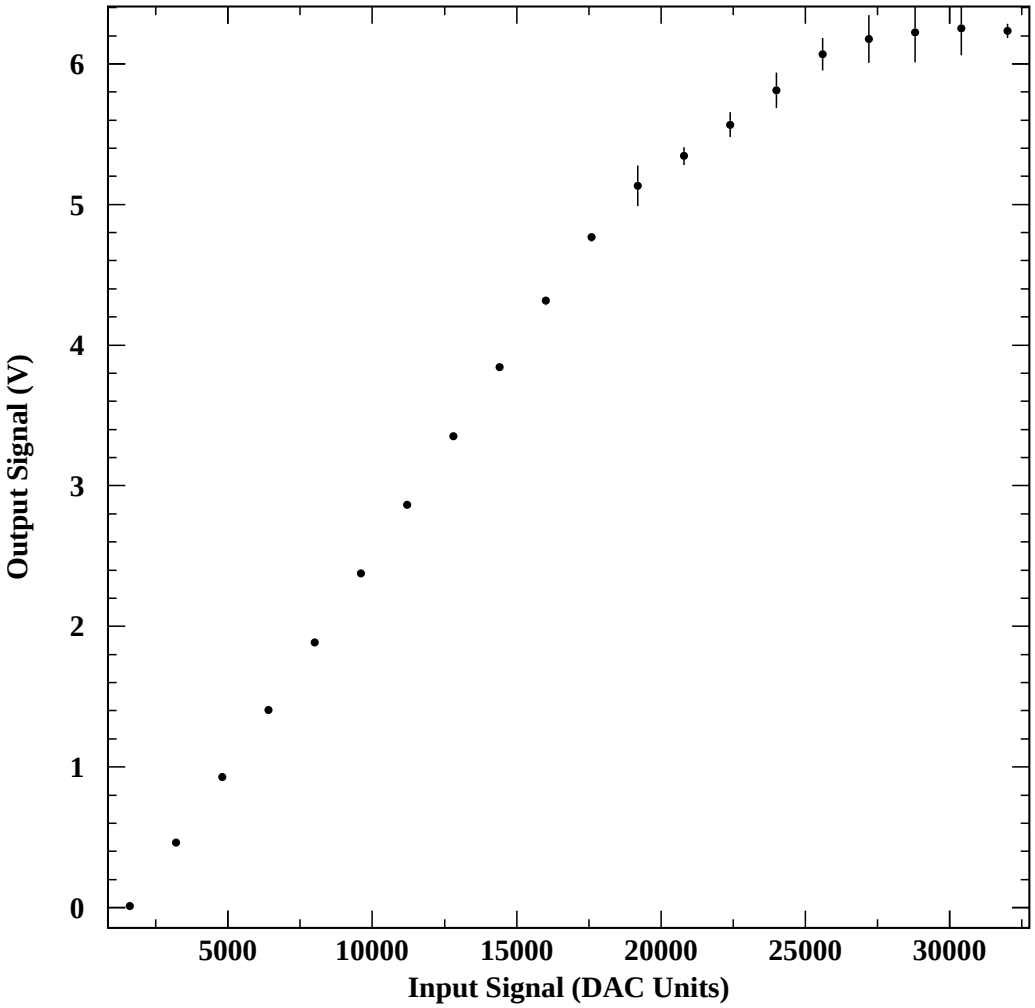

Figure 4.26: The response of the mono-gain system (channel 94) demonstrating the severe non-linearity exhibited by 11 channels (Run 32809).

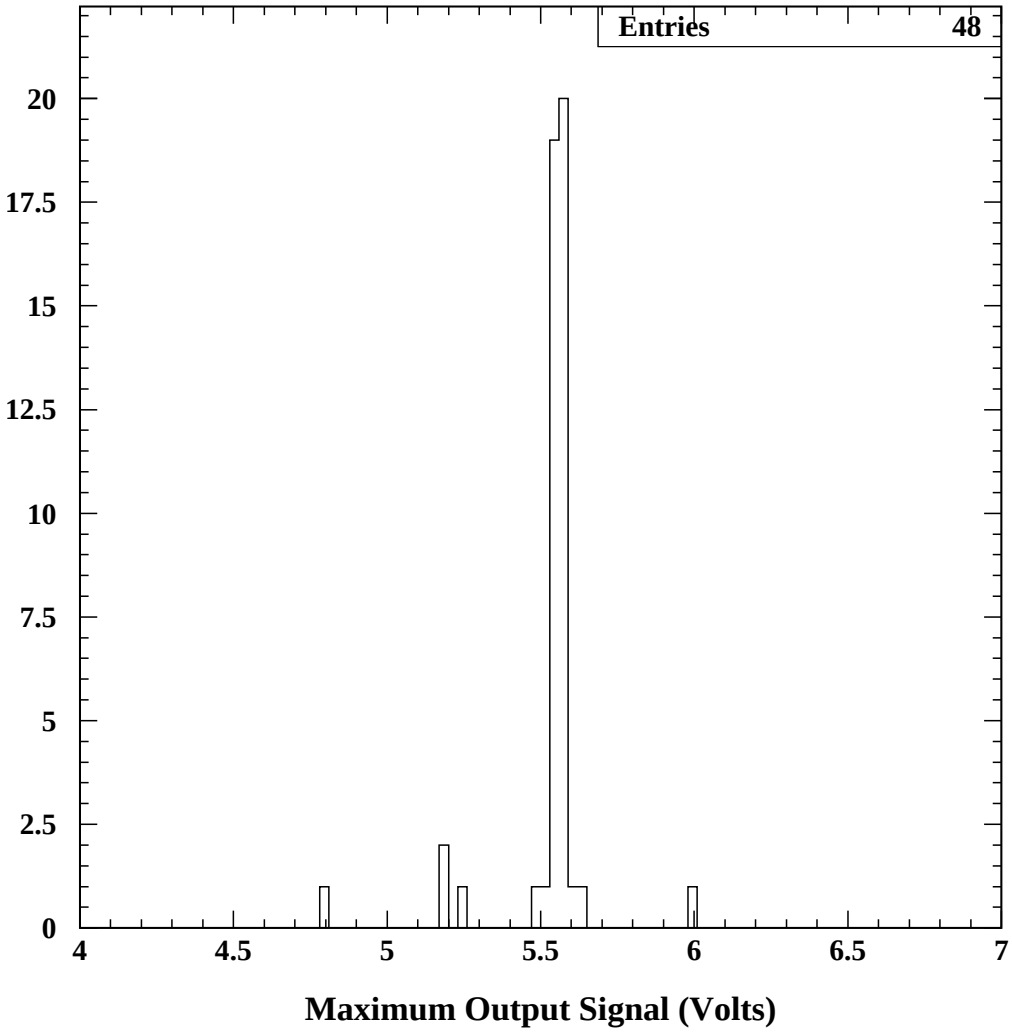

Figure 4.27: The distribution of maximum output signals for the first badly non-linear DAC setting (13th) of channel 94 (Run 32809).

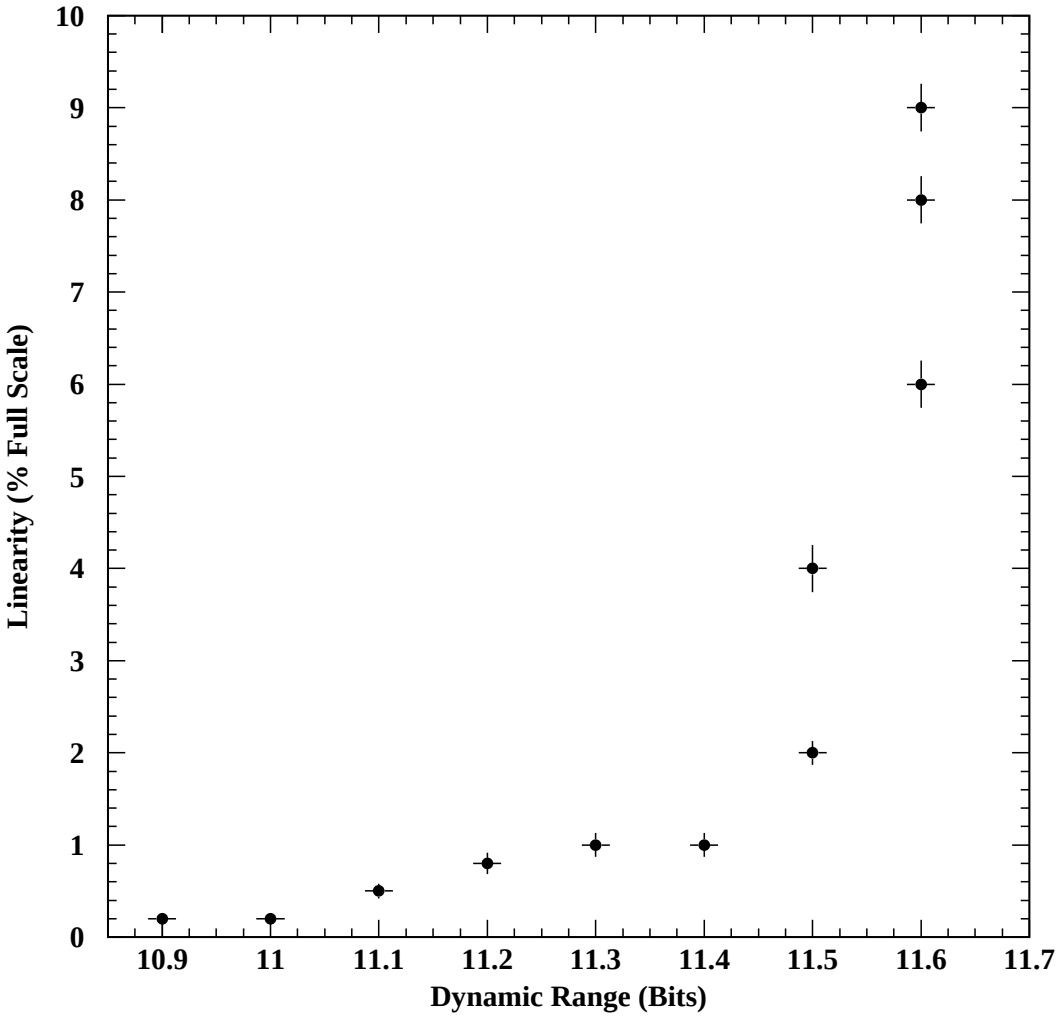

Figure 4.28: The linearity of the system as a function of dynamic range, which was being truncated from the upper range. The data was taken with the mono-gain shapers (Run 32809).

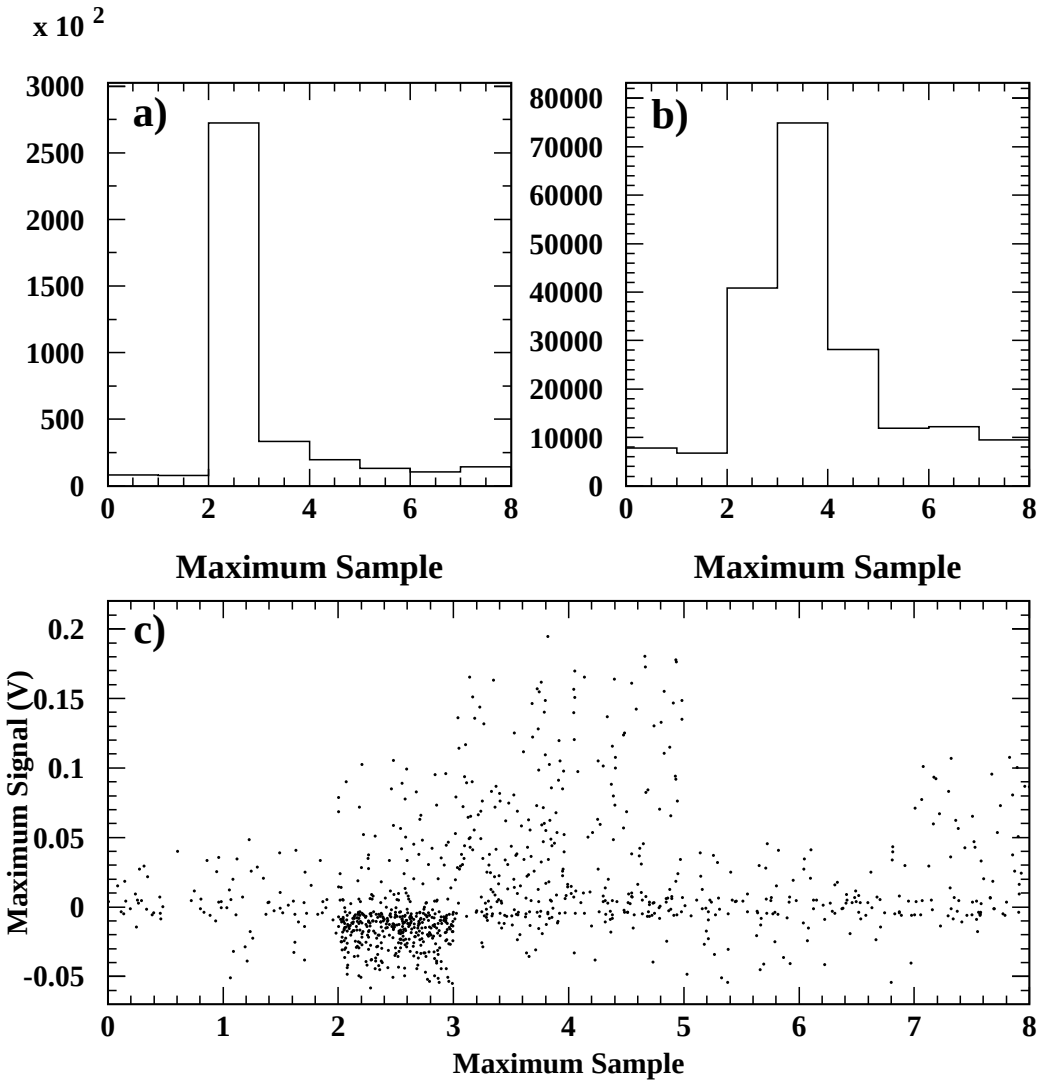

Figure 4.29: Sample dependence on cross-talk signal maxima. Plot (a) illustrates the sample containing the maximum cross-talk amplitude for negative amplitudes; plot (b) illustrates the same for positive amplitudes. The maximum signals (cross-talk) are plotted against the sample they occur in (c) (Run 32687).

$\phi\backslash\eta$	*1*	*2*	*3*	*4*	*5*	*6*
14	0.002	0.002	0.002	0.002	0.002	0.002
13	0.002	0.002	0.002	0.002	0.002	0.002
12	0.002	0.002	0.002	0.002	0.002	0.002
11	0.002	0.002	0.002	0.002	0.002	0.003
Front Layer						
14	0.002	0.002	0.002	0.002	0.002	0.002
13	0.002	0.002	0.002	0.002	0.002	0.003
12	0.002	0.002	0.002	0.002	0.002	0.002
11	0.002	0.002	0.002	0.002	0.002	0.002
Middle Layer						
14	0.002		0.002		0.002	
13	0.002		0.002		0.002	
12	0.002		0.002		0.002	
11	0.002		0.002		0.002	
Back Layer						

Table 4.5: Average RMS noise (volts) in η and ϕ for the bi-gain shapers.

between a pulsed cell and the cell which was situated above or below it in the same layer.

The cross-talk amplitudes increased (with positive or negative polarity) linearly (Figure 4.30) with input pulse amplitude after the first few settings. Channel 36 in Figure 4.30 increased at a rate of -66 mV/DAC unit while channel 45 increased at 59 mV/DAC unit. Calorimeter cells which were not situated next to pulsed cells also had amplitudes which increased linearly.

Varying the operating parameters, with the exception of the disabling of the reference subtraction circuit, caused no significant difference in the cross-talk. When the reference subtraction circuit was disabled (refer to Appendix D), the most noticeable effect was that the amplitude polarity on the nearest cells flipped. The amplitudes of the cross-talk signals were greater than the corresponding RMS values

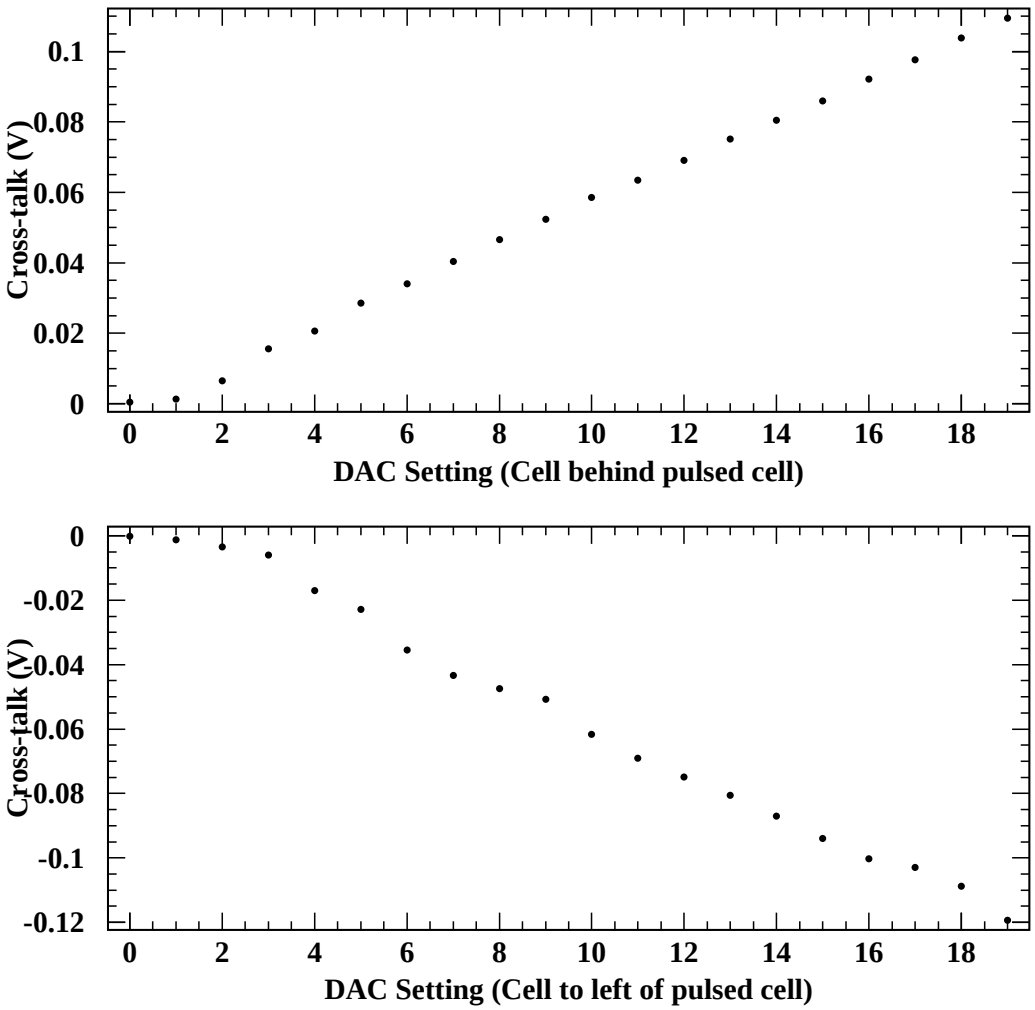

Figure 4.30: Cross-talk amplitudes for the cell immediately behind (channel 45) a pulsed cell and for a cell to the left (channel 36) of another pulsed cell.

within the first few settings (greater than 40 mV), as opposed to greater then 5 V for the data where the reference subtraction circuit was enabled. This result demonstrated that the reference subtraction circuit reduced cross-talk by about a factor of 100.

4.11 Summary of Calibration Studies

The bi-gain system was linear (no deviations from the output versus input curve greater than 0.3% of full range) over a voltage range of 0.0 V to 4.5 V, or a dynamic range of 11.2 bits. The bi-gain data, taken with the reference subtraction circuit disabled (Figure 4.25), was linear over a dynamic range of about 10.4 bits. The reason for the lower dynamic range was that the RMS for this data was significantly higher than with the baseline data. The mono-gain system performed linearly (0.8% of full range) in the region of 0.0 V to 4.8 V which corresponded to a dynamic bit range of 11.4 bits.

The problems encountered with the gain switching could have been caused by a time jitter in the calibration pulser and not with the readout board. The time jitter caused a strong dependence on the trigger delay as the shifting of the pulse by 25 ns caused gain switching to occur over more than a single DAC setting.

The largest cross-talk was measured in the channels corresponding to calorimeter cells adjacent in η as well as the layer in front or behind the cell. No significant cross-talk was measured in the cells neighbouring in ϕ in the same layer. The cross-talk signals had distorted shapes compared to the calibration pulses. They were often inverted. When the back layer was pulsed there appeared cross-talk with amplitudes 10 times larger than RMS. This was not expected and could not be explained. When

the reference subtraction circuit was disabled the main effect on the cross-talk signals was a polarity change.

CHAPTER 5

Electron Energy Resolution

5.1 Introduction and Description

A reconstruction of the electron beam energy was performed to determine the performance of the calorimeter and readout system. There were four energies of electrons used during the study: 100, 150, 200 and 300 GeV. As in the noise and calibration studies, the data was taken with different conditions to observe the effect on the results. Mono-gain data was also recorded. The bi-gain runs were taken with low gain forced and in automatic gain switching mode. The automatic gain switching runs were actually high gain runs as the energy required to switch the gain was never achieved. All of the data used, bi-gain and mono-gain, is summarized in appendix A.

The measured energy in an electromagnetic calorimeter will fluctuate due to several factors [22]. These factors include fluctuations in the energy sampling*, leakage out of the calorimeter boundaries, pile-up, electronic noise, etcetera. If the calorimeter is detecting a beam of electrons of energy E, the variance of the distribution of detected electron energy can be expanded in a power series of the form:

$$\sigma^2(E) = b^2 + a^2 E + c^2 E^2 + \cdots \tag{5.1}$$

*The calorimeter described in this thesis is a sampling calorimeter meaning that active (measuring) layers of the calorimeter are placed between layers of inactive material, copper for example, and thus the energy measured is a "sampling" of the shower as it traverses the detector

which can be re-written, after dividing through by E^2 and dropping the argument of σ, as:

$$\frac{\sigma}{E} = \sqrt{c^2 + \frac{a^2}{E} + \frac{b^2}{E^2} + \cdots}. \tag{5.2}$$

We are only concerned with the three leading terms, as higher powers of $1/E$ become negligible, so after dropping the higher order terms, equation 5.2 can be written in the following simplified form:

$$\frac{\sigma}{E} = c \oplus \frac{a}{\sqrt{E}} \oplus \frac{b}{E} \quad , \tag{5.3}$$

where a, b, and c are constants and the terms are added in quadrature*. The constant term, c, dominates at high energies. This term is due to the calibration, mechanical assembly, and detection medium [10] [22]. The $\frac{a}{\sqrt{E}}$ term describes any Poisson fluctuations such as sampling fluctuations, or in the case of a tile calorimeter, the fluctuations in the number of photoelectrons liberated at the surface of a photo-multiplier tube. This term is dominant over the majority of energies measured. The last term, $\frac{\mathrm{b}}{\mathrm{E}}$, is referred to as the noise term. The noise term is dominant at low energies (10's of MeV).

The electromagnetic calorimeter is required to make lepton energy measurements in the energy range 10-100 GeV for the rare decays $\mathrm{H} \rightarrow \gamma\gamma$ and $\mathrm{H} \rightarrow \mathrm{ZZ} \rightarrow 4\mathrm{e}$. All three of the terms described above would thus contribute to the energy resolution. For these decays it has been determined [4] that a sampling term of less than $\frac{10\%}{\sqrt{\mathrm{E}}}$ and a constant term of less than 1% would suffice. The constant term, although dominant at high energies (TeV range), does significantly contribute to the energy resolution

*The $\oplus$ symbol refers to the square root of the sum of squares, or quadrature addition.

down to an energy of around 40 GeV. A goal for this term has thus been set at 0.7% (over a nonet tower illustrated in Figure 5.1).

5.2 Electron Energy Reconstruction

The electron energy reconstruction involved applying calibration corrections (calibration constants) to the raw data in order to minimize the value of $\sigma(E)/E$. There were three basic types of calibration constants applied, gain, timing corrections, and pedestals. The gains were applied to account for inherent gain differences between channel. The timing constants were applied to account for the approximate pulse shape used in the analysis, and the timing differences between layers of the calorimeter. The pedestals were subtracted from the ADC count distributions.

5.2.1 Reconstruction Procedure

The reconstruction of the energy took two distinct steps, not including the application of the corrections mentioned above. The first step was to scan the cells to find the cell containing the maximum energy. This cell was then determined to be the "seed" cell of the electromagnetic shower. The front layer of the calorimeter contained the seed cell for approximately 72% of the seed cells, while the middle and back layers contained 18% and 10% of the seed cells respectively. Once this was accomplished, a "tower" was built which would contain the deposited energy of the electron beam.

5.2.2 Tower-building Methods

The key to the most accurate energy measurement was the size of the tower. If it was too small it would not contain all of the deposited electron energy, while if it was too large, the additional noise would affect the measurement. As the (bi-gain) calorimeter was $4\times6 = 24$ cells in the first two layers and 12 in the back, three different tower sizes were investigated. The first of these was a tower containing three cells, one from each layer (in line with the impact cell). The second was the entire calorimeter, all 24+24+12=60 cells. The last tower was built by summing 24 cells surrounding the seed cell (nonet tower), 9 in the front layer, 9 in the middle layer, and 6 in the back layer (Figure 5.1).

It was found (for 200 GeV electrons using the high gain system) that the best resolution came from the nonet tower as illustrated in Figure 5.2. It has been determined that this tower (for the prototype calorimeter used in this experiment) contains approximately 94% of the electron energy [17]. The same group found that increasing the cluster size to a 5×5 tower in the first two layers had the disadvantage of contributing 40% more electronics noise, which would be critical at low energies. The energy for the tower for the maximum sample, the sample before the maximum, and the sample following the maximum were then fitted to a parabola*. From the parabolic fit, the actual maximum energy of the pulse, as well as the time which this maximum occurred, could be calculated.

*A parabolic fit was found to work best for the pulses. A correction was made to the data to account for the shape difference between the parabolic fit and the actual more complex pulse shape.

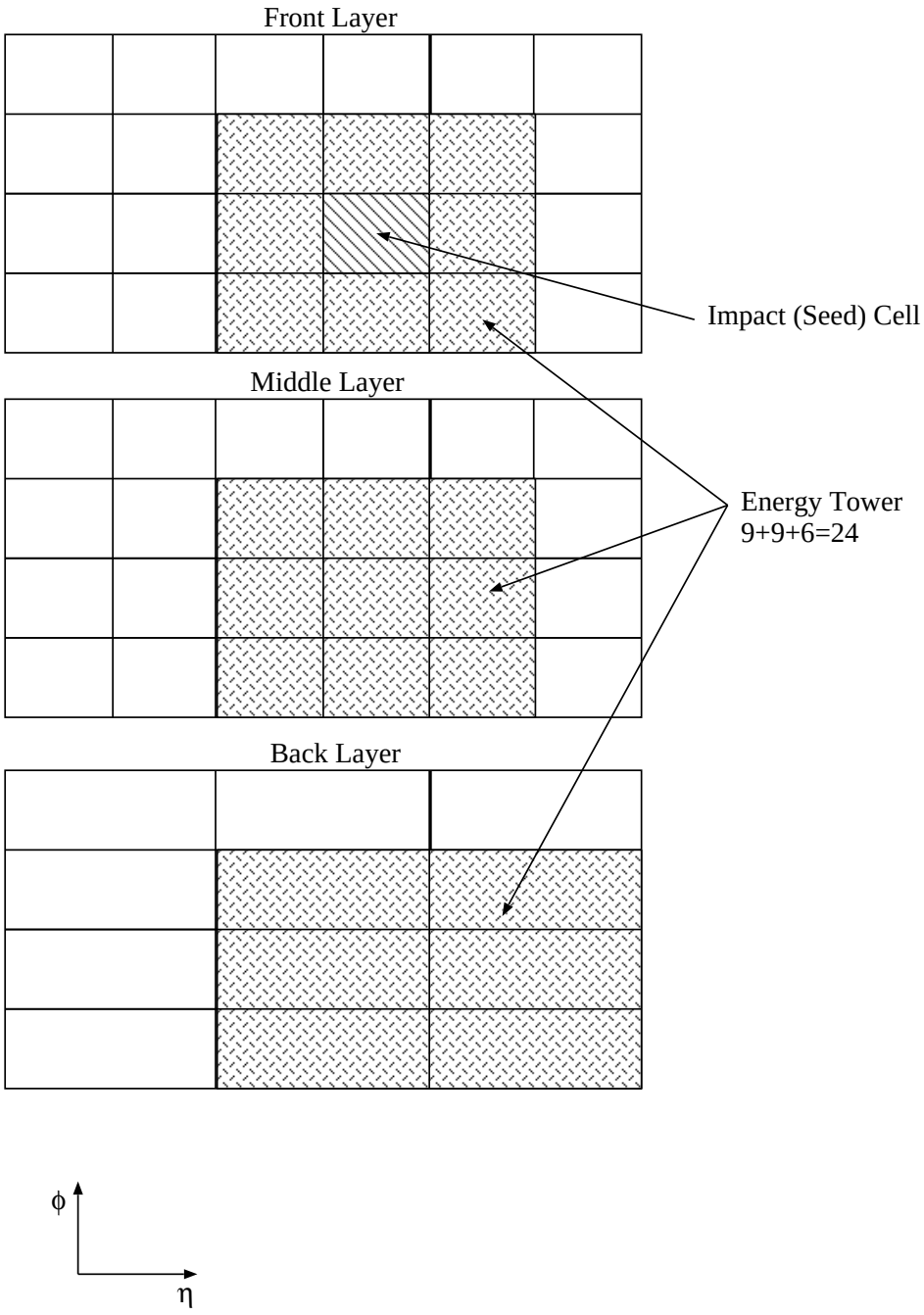

Figure 5.1: Construction of energy tower showing the impact cell and summed cells in all three layers.

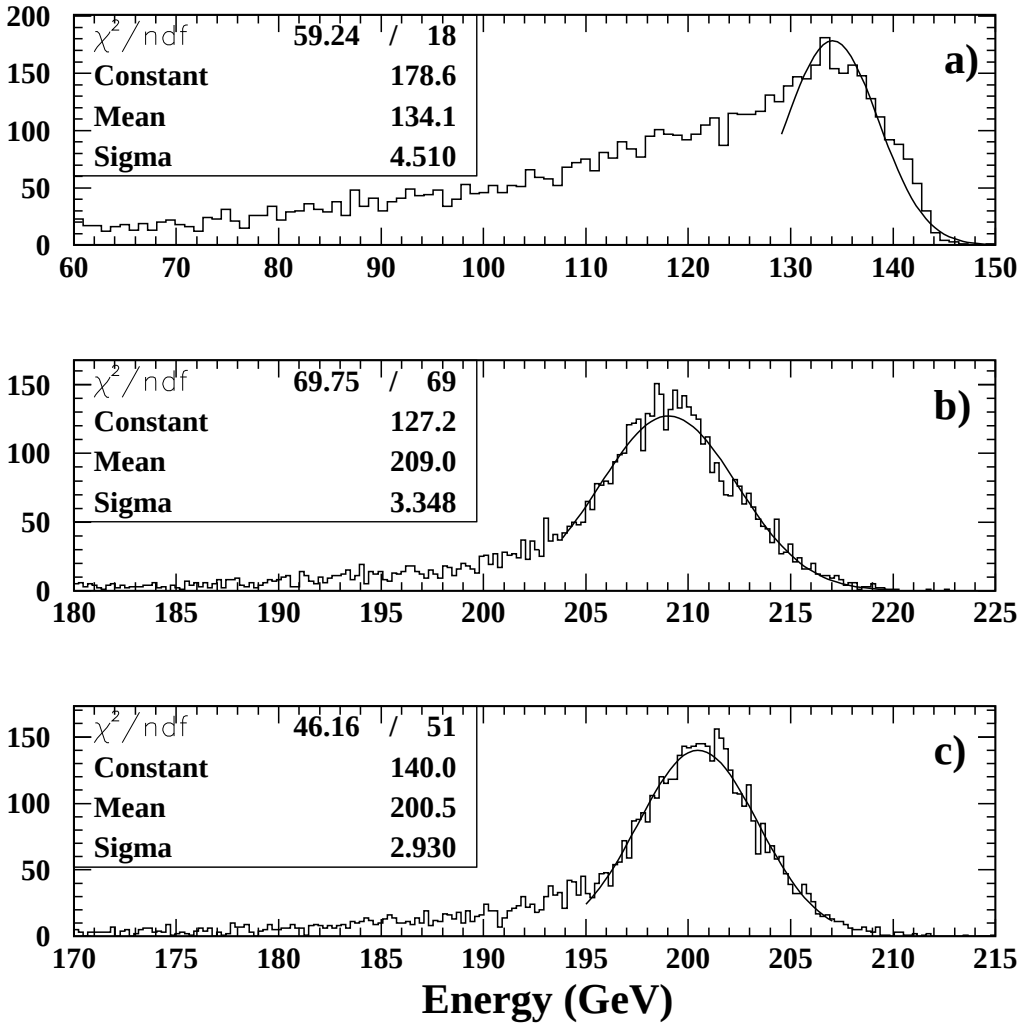

Figure 5.2: Resolution (σ/E) for 3 calorimeter cells in line (depth) with the impact cell (a), the sum of all calorimeter cells (b), and the nonet tower (c). The resolutions were 3.363%, 1.602%, and 1.461% respectively. The data was 200 GeV electrons taken with the baseline high gain system (Run 32685).

5.3 Corrections to Measured Energy Resolution

The energy resolution was measured after the pedestal subtraction and then again after the application of additional calibration constants.

5.3.1 Application of Calibration Constants

Each channel had a gain which differed from the others as pictured in Figure 5.3. A determination of how best to apply a correction to account for gain differences involved fitting the output signal versus input signal pulser data for each channel and then using the parameters from the fit for the correction. A linear fit, with non-fixed intercept, would have implied a perfectly linear system and the first derivative would correspond to the gain used for the correction. A quadratic fit was also tried where the coefficient of the quadratic term corresponded to the non-linearity of the system and the coefficient of the linear term was the gain, thus giving two parameters to apply to the data. To determine which fit was best, the "goodness of fit" was compared between the two. The reduced χ^2, variance squared over the number of degrees of freedom, was used for this purpose. The percent improvement, in terms of the χ^2, for the quadratic fit over the linear fit was (50 ± 10) %, and thus the quadratic fit was used in the gain corrections. The correction for each channel was

$$E_{Corr} = AE + BE^2, \tag{5.4}$$

where E_{Corr} was the actual energy in a cell, E was the measured energy in a cell, A was the gain, and B was the non-linearity. The gains were calculated using the data in the region where the output versus input signal curve was linear, i.e. the last 8 points were removed from the analysis.

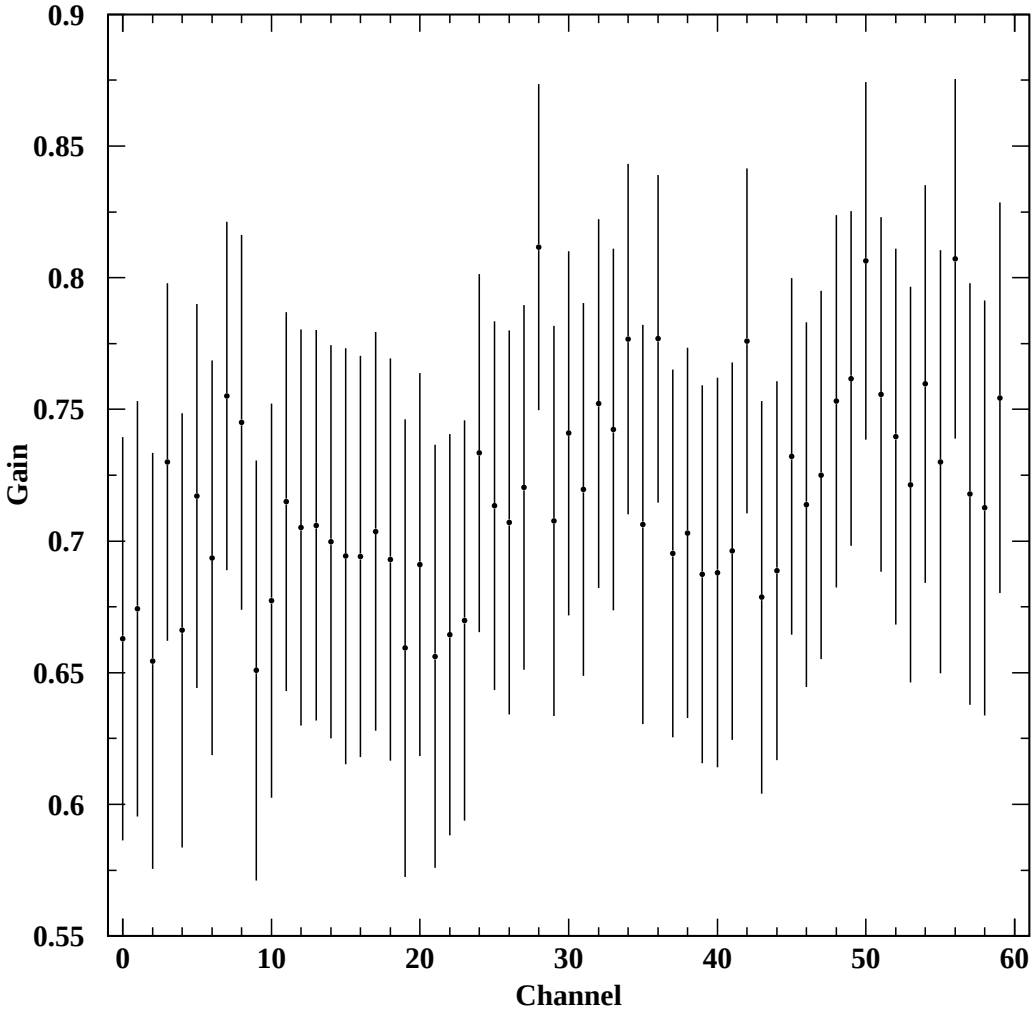

Figure 5.3: Gains (slope of input signal versus output signal plots) averaged over all 20 settings for each channel, for the high gain baseline data (Run 32687).

For the purpose of describing the procedure for determining and applying the corrections*, a bi-gain data run at 200 GeV was used (Run 32685). With no corrections, except pedestal subtraction, the measured energy resolution ($\frac{\sigma(E)}{E}$) was $(6.69 \pm 0.08)\%$. Application of the gain corrections improved the energy resolution to $(2.46 \pm 0.01)\%$.

5.3.2 Time of Pulse Maximum Correction

The pulse shape was approximated by fitting a parabola to the three samples with the highest ADC values. As described in section 5.2.1, there was a slight dependence between the time where the actual maximum of the pulse occurred and where the maximum of the parabolic fit occurred. The energy was plotted against the relative time of maximum, or the difference between the maximum sample and the time where the pulse maximum was estimated to be located (Figure 5.4 (a)). A polynomial was fit through the data. The polynomial was used to obtain the following correction

$$E_{\mathrm{Corr}} = E\frac{P_{\mathrm{n}}(0)}{P_{\mathrm{n}}(t_{\mathrm{max}})}, \tag{5.5}$$

where E was the energy before the correction and $P_{\mathrm{n}}(t_{\mathrm{max}})$ was a polynomial, in t_{max}, of degree n. The degree of polynomial which provided the best result, in terms of reducing the energy resolution, was a 6th order polynomial. The result of the correction using this function is shown in Figure 5.4 (b). The correction improved the resolution from 2.46% to 1.46%.

*Prior to any reconstruction studies, pedestals were subtracted from each ADC value.

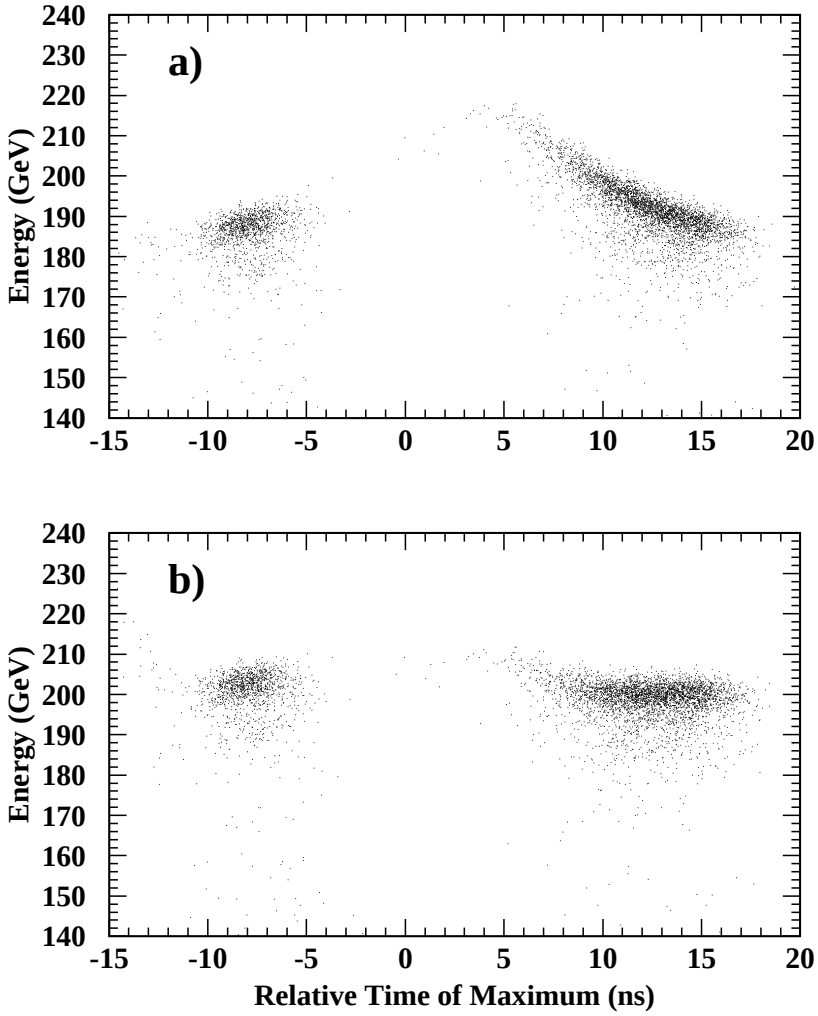

Figure 5.4: Relative time of maximum of signal pulse maximum, with respect to the maximum sample plotted against total summed energy with no correction (a), and with 6th order polynomial correction (b). The data was 200 GeV electrons taken with the baseline high gain system (Run 32685).

5.3.3 Angular Dependence on Energy Resolution

Other variables which may have had an effect on the energy resolution were η and ϕ. The energy weighted cell positions were plotted (Figure 5.5) in the η-ϕ plane. Within the beam region (boxed region in Figure 5.5) there was negligible variation in energy. Outside of the beam region the approximate mean energy (for 200 GeV electrons) was 50 GeV. Only the data inside of the beam region was used in determining the resolution. The data outside of the box in Figure 5.5 accounted for approximately 30% of the total data. The omission of this data caused the energy resolution to improve to 1.43% from 1.46%.

5.3.4 Correction for Cross-talk

Without pulsing each cell individually it was not possible to apply a set of corrections for the cross-talk between channels. An approximate correction was made using the cross-talk data described in section 4.10. The correction was made to a single cell (the impact cell corresponding to channel 5). The cross-talk from the row (in the η direction) containing the cell was subtracted off of the channel. The data came from the pattern in which channel 5 was pulsed. This approximate correction provided a slight improvement (less than one tenth of a percent) to the energy resolution.

5.4 Energy Resolution

The corrections were then applied to each set of data. The energy resolution for each data sample was then tabulated in Table 5.1. For the high gain system, the energy resolution improved with energy with the exception of the 300 GeV data. The three

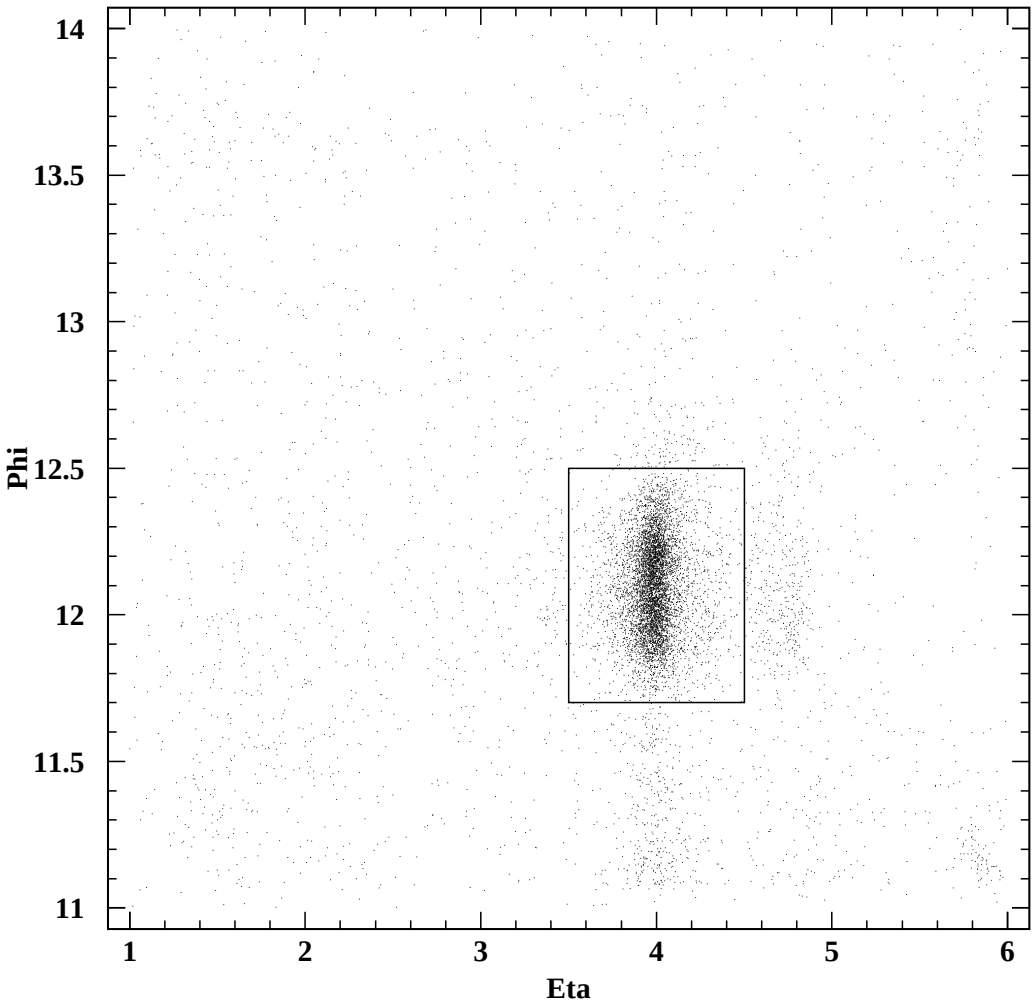

Figure 5.5: Electron impact cells in the The η-ϕ plane. The box denotes the region where the data used for calculations was taken. The data was 200 GeV electrons taken with the baseline high gain system (Run 32685).

Run	*Gain*	*Trigger Delay ns*	*Operating Conditions*	*Energy GeV*	*Resolution %*
32685	High	575	Baseline	200	1.43 ± 0.02
32703	High	575	Baseline	100	1.90 ± 0.03
32734	High	575	Baseline	150	1.63 ± 0.05
32906	High	600	Baseline	300	2.88 ± 0.03
32686	Low	575	Baseline	200	5.3 ± 0.1
32704	Low	575	Baseline	100	5.5 ± 0.1
32735	Low	575	Baseline	150	6.7 ± 0.1
32907	Low	600	Baseline	300	4.2 ± 0.1
32693	High	575	Clock On	200	1.92 ± 0.05
32761	High	575	No Ref-Sub	200	2.44 ± 0.05

Table 5.1: Summary of energy resolution values for bi-gain data.

data points from the high gain data taken with the 575 ns trigger delay are shown in Figure 5.6. The 300 GeV data was taken with the 600 ns trigger delay rather than the 575 ns trigger delay and the "time of maximum parameterization" did not improve the energy resolution. The low gain system gave a worse energy resolution than the high gain system (Figure 5.7).

The resolution measured for the data (200 GeV electrons) with the reference subtraction circuit disabled was approximately twice as large as that for the baseline data. This was likely due to the summing of additional noise in the nonet. The data taken (200 GeV electrons) with the write clock enabled had an energy resolution slightly higher than the baseline data, most probably for the same reason

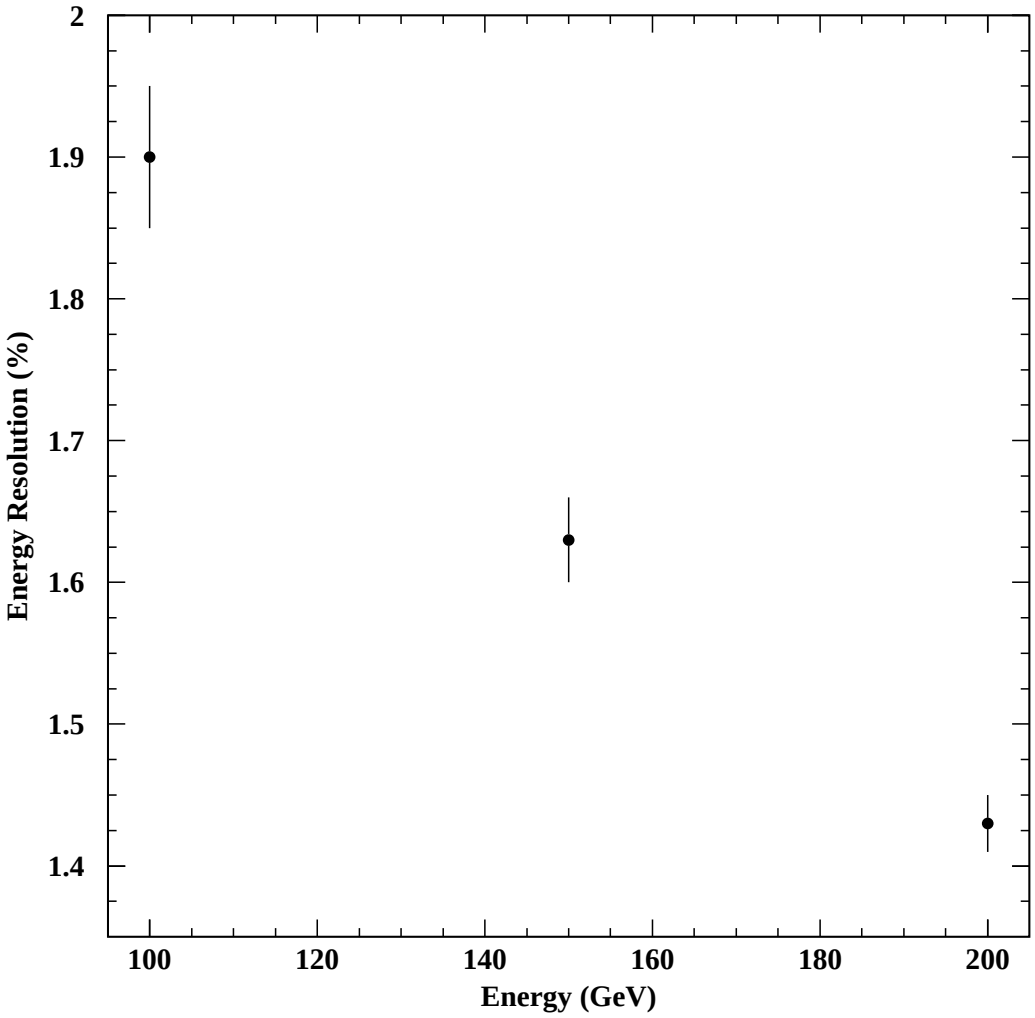

Figure 5.6: Energy resolution versus beam energy for the baseline (high gain) data.

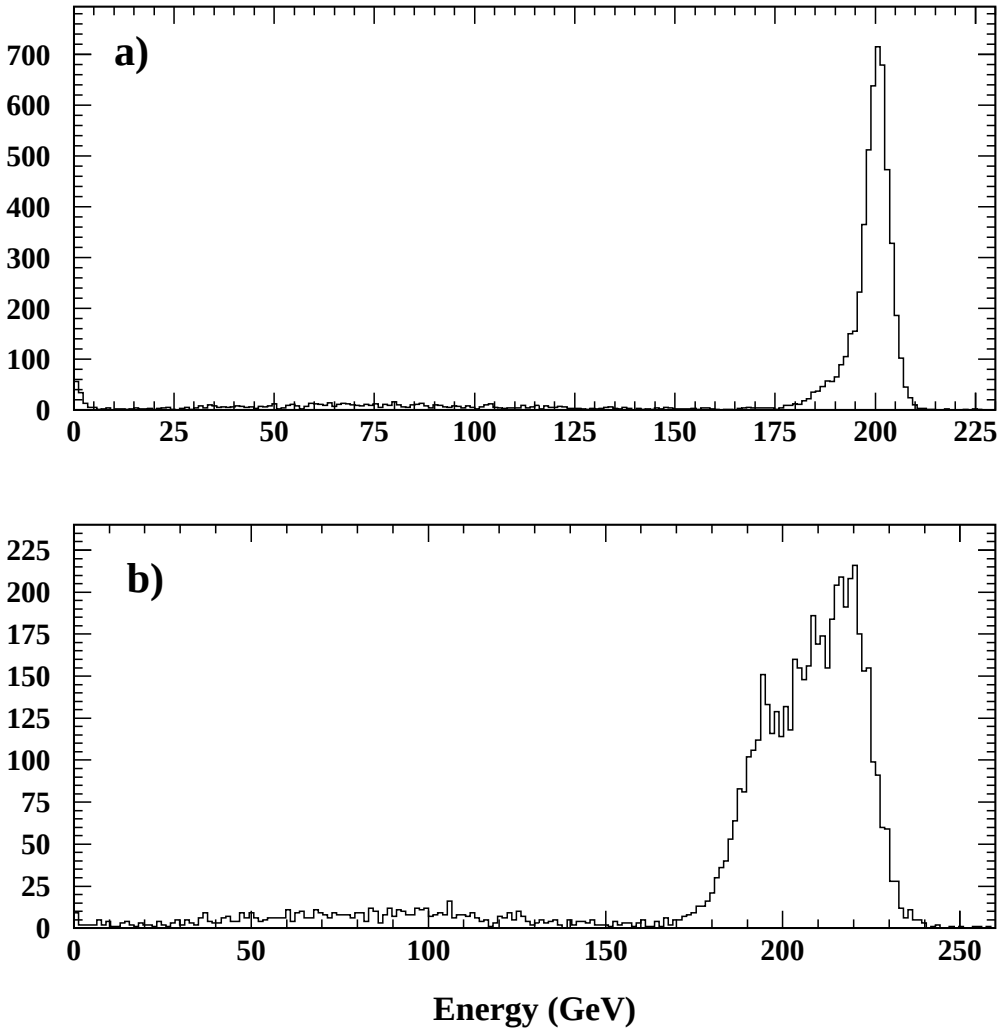

Figure 5.7: The energy resolution distributions for 200 GeV electrons. Plot (a) shows the resolution for the data taken with the high gain system while plot (b) shows the resolution for data taken with low gain system.

Run	*Gain*	*Trigger Delay ns*	*Operating Conditions*	*Noise Term MeV*
32689	High	575	Baseline	550 ± 80
32697	High	575	Clock On	580 ± 80
32667	High	600	2μs Readout Time	630 ± 140
32883	High	575	No Reference Subtraction	550 ± 100
32690	Low	575	Baseline	480 ± 80

Table 5.2: Total noise summed through a nonet energy tower.

5.5 Determination of Noise Term in the Energy Resolution

The noise term $\frac{b}{E}$ in the energy resolution expansion (equation 5.3) was estimated using three methods: a sum of the noise in an energy tower, reconstructing signals of zero amplitude (noise data), and by using the resolution measured in the section 5.4 along with *a priori* knowledge of the sampling term and constant term of the resolution expansion. The first method used was to sum the total noise (incoherent and coherent described in equation 4.5) in a nonet or energy tower; in the same manner as described previously. The average energy over capacitor and time sample for each channel was used in the sum. This sum represented the best achievable value for the energy resolution due to the limit imposed by the electronics noise in the system. For the baseline high gain system the total noise was found to be (550 ± 80) MeV. Results with different run parameters is compiled in Table 5.2.

The second method used for estimating the noise term in the energy resolution expansion was to use the reconstruction algorithm for the electrons on the noise data where no pulses were present. The width of this distribution represented the best resolution which could be achieved with the system. It would represent the low

Run	*Gain*	*Trigger Delay* *ns*	*Operating* *Conditions*	*Noise Term* *MeV*
32689	High	575	Baseline	580 ± 30
32697	High	575	Clock On	600 ± 40
32667	High	600	2μs Readout Time	850 ± 80
32883	High	575	No Reference Subtraction	490 ± 30
32690	Low	575	Baseline	510 ± 30

Table 5.3: Reconstruction of noise data using the same algorithm used for electron energy reconstruction (note that for the data taken with the short readout time no gain corrections were used).

energy limit of the resolution expansion. For the high gain baseline data, the noise term estimate was (580 ± 30) MeV, which was consistent with the total noise summed in the tower. Table 5.3 contains the resolution values for the remaining data. There was good agreement between the two methods. The one exception being the data taken with the 2 μs readout time. For this data, a gain correction was not possible as no usable calibration data was available for this run condition. It was found, by examining the baseline data with and without gain corrections, that approximately a 13% improvement could be obtained. This would put the two values for the 2 μs readout time in agreement.

The last method for approximating the energy resolution was to use the energy resolutions measured in section 5.4 to estimate the electronics noise term. Ideally a fit would have been made to the energy resolution versus energy data to find the parameters. As no 50 GeV data was taken and data with the same run conditions was only taken for 3 energies, the values of the sampling term and constant term were fixed using values obtained by Auge *et al* [24]. Using these fixed values, an approximate fit could be made. The values used were $\frac{(10.03\pm0.30)\%}{\sqrt{E}}$ for the sampling term and (0.00 ± 0.11) % for the constant term. Using these values, a fit to the data

gave noise terms of (1.6 ± 0.1) GeV/E and (5.4 ± 0.1) GeV/E were for the high and low gain data respectively.

5.5.1 Electron Data Taken with Mono-gain Shapers

Only 200 GeV data was successfully taken with the mono-gain shapers. The resolution for the energy distribution was (2.32 ± 0.03)%. This was roughly twice that of the high gain 200 GeV data taken with the bi-gain shapers. The total energy sum made over the energy tower was used as an approximation of the noise term as was the reconstruction of the noise data. The values for these were (750 ± 80) MeV and (1400 ± 100) MeV respectively. As can be seen in Appendix C the back layer of the calorimeter used for the mono-gain shapers was not projectively in line with the other two layers and hence was not used in the estimations of the noise term.

5.6 Discussion

An estimate of (110 ± 20) MeV/channel was made for the noise term of the high gain system using a sum of the total noise per channel within the nonet tower. A second estimate of (118 ± 6) MeV/channel was made for the same system by applying the energy reconstruction algorithm to the noise data. For the low gain system, values of (100 ± 20) MeV/channel and (104 ± 6) MeV/channel were obtained using the same procedures. The noise introduced per channel by the calorimeter and shapers was between 40 MeV and 70 MeV, depending on the region of the calorimeter [16]. For the case where the only 40 MeV/channel of noise was introduced before the readout system, the readout noise was between two and three times higher.

The value for the noise term determined by an approximate fit of the resolution

versus energy data gave a significantly higher value of (330 ± 20) MeV/channel for the noise of high gain electronics. This value could be due to the approximate fit of the three data points. The low gain noise term, using the same method, gave a much higher value of the resolution of (1.10 ± 0.02) GeV/channel. The distribution had an RMS width approximately 5 times higher than that for the high gain width. As the previous methods used in this thesis gave approximations to the noise term for high and low gain electronics, which were consistent with each other, the discrepancy between the noise term for electronics chains in the fit method could not be explained.

The operating condition which caused the largest increase in the noise term (other than the low gain for the fit method) was the reduction in the readout time (roughly 15% for the summed tower noise estimate). As was explained in section 4.7 the shorter readout time could have caused the reading of the readout amplifier to be premature, causing fluctuations in measured voltages. The remaining run time condition changes were consistent with the baseline values.

The mono-gain system had values of (180 ± 20) MeV/channel and (330 ± 30) MeV/channel for the tower noise sum and reconstruction of noise respectively. The width of the 200 GeV electron energy distribution was approximately twice that of the same distribution for the high gain width. As data was only taken for a 200 GeV run, comparisons between different data were not possible.

CHAPTER 6

Summary and Recommendations

6.1 Summary of Results

The readout boards developed at the University of Alberta were studied in terms of noise, linearity, and energy resolution performance. The baseline high and low gain systems had noise values of (3.1 $\pm$ 0.3) mV/capacitor and (2.7 $\pm$ 0.3) mV/capacitor respectively. The coherent noise, across channels, was (0.55 $\pm$ 0.01) mV/capacitor and (0.55 $\pm$ 0.02) mV/capacitor for the high and low gain systems respectively.

When the write clock was enabled, the noise distribution developed a significant tail and the first capacitor became noisier. When the time for reading out data from the pipeline was reduced to 2 μs the noise increased for both the high and low gain systems. The increase in noise was about 6% for the high gain electronics chain and 25% for the low gain. The reference subtraction reduced the cross-talk but caused additional incoherent and coherent noise.

A 14% increase in noise, over the high gain system, was measured for the mono-gain system. An 33% increase in coherent noise across channels was also measured. The additional noise could have come from additional multiplexing circuitry, but as different shapers and preamplifiers were used in a different region of the calorimeter, no definitive conclusions could be drawn.

The dynamic range of the bi-gain system was determined to be 11.3 bits. The

system was linear from 0 V to 4.5 V. For the mono-gain system a dynamic range of 11.6 bits was achievable, but the system became noticeably non-linear after 11.4 bits. The mono-gain system was linear from 0 V to 4.8 V. In the bi-gain system gain switching occurred between an input signal of 5 V to 7 V. This was explained in terms of a timing jitter on the input pulses.

The cross-talk was large and extended beyond nearest neighbours. No conclusions could be drawn as the calorimeter was pulsed such that it was not possible to accurately measure the cross-talk caused by the pulsing of a single channel. It was possible to determine that the largest cross-talk occurred between cells which were in the same η-ϕ coordinate in the next layer and in cells which resided side-by-side in ϕ. When corrections were made to the electron data using the estimated values of cross-talk the results were inconclusive.

The noise term in the expansion of the energy resolution was estimated three different ways; the first two using the noise data and the third using the electron data. The first two estimates gave values for the noise of (110 $\pm$ 20) MeV/channel and (118 $\pm$ 6) MeV/channel for the high gain electronics and (100 $\pm$ 20) MeV/channel and (104 $\pm$ 6) MeV/channel for the low gain electronics. The only run time parameter which caused a significant increase in the value of the noise term was the reduction in readout time. Reducing the readout time from 4 μs to 2 μs caused an increase in the noise term of 15%. The third method used to estimate the noise term gave a value of (330 $\pm$ 20) MeV/channel for the high gain system and (1.10 $\pm$ 0.02) GeV/channel for the low gain system. The low gain electronics had an energy distribution roughly 5 times wider than the high gain electronics. No explanation was found. For the mono-gain system values were estimated for the noise term of (180 $\pm$ 20) MeV/channel and (330 $\pm$ 30) MeV/channel for the tower noise sum and reconstruction-of-noise methods. Only the 200 GeV electron data was successfully recorded with this system

and thus an estimate of the noise term using the energy resolution versus energy data was not possible.

6.2 Recommendations

A few modifications in the experimental procedure could have led to a better understanding of the system. Had time been available, bench testing before and after the CERN test would have provided a means to determine which effects were due to the board and which were due to the calorimeter, and corresponding electronics. A deeper understanding of the non-linearity at a high input voltage may have been achievable. Another experimental detail which could have been improved upon was the calibration pulsing method. If every cell had been pulsed individually, it would have been possible to carefully measure the cross-talk as well as develop cross-talk corrections to use with the electron reconstruction analysis.

In terms of design improvements to the readout system, there were two areas where improvements could have been made; first in gain switching, and second in the noise introduced by the connection between the pipeline and the first sample and hold. The switching problem could possibly be avoided in the future by using a digital comparison rather than the analog method.

The connection between the SCA pipelines and the first sample and hold was high impedance making it susceptible to any local noise from other components. This connection increased the noise and limited the measured energy resolution as well as the dynamic range. If the sample and hold was included in the pipeline chip, the noise may have been reduced.

Bibliography

[1] Aitchison I. and Hey A., *Gauge Theories in Particle Physics (2nd Ed.)*, Institute of Physics Publishing, 1989.

[2] Halzen F. and Martin A., *Quarks and Leptons: An Introductory Course in Modern Particle Physics*, John Wiley and Sons, 1984.

[3] Martin Stephen P., *A Supersymmetry Primer*, HEP-PH/9709356, 1997.

[4] ATLAS Collaboration, *ATLAS Technical Proposal for a General-Purpose pp Experiment at the Large Hadron Collider at CERN*, CERN/LHCC/94-43, 1994.

[5] Kim, Shinhong for the CDF Collaboration, *Observation of Top Quark Production Using Kinematic Techniques*, Proceedings of the "QCD and High Energy Interaction, XXXth Recontres de Moriond", Les Arcs, France, March 19th to 26th, 1995.

[6] ATLAS Collaboration, *LHC - CHALLENGES IN ACCELERATOR PHYSICS*, http://nicewww.cern.ch/lhcp/General/apchall.htm.

[7] LHC Study Group, Lefvre P., Pettersson T., Eds., *The Large Hadron Collider - Conceptual Design*, CERN/AC/95-05(LHC), 1995.

[8] Gorfine G. and Taylor G., *Particle Fluxes and Damage to Silicon in the ATLAS Inner Detector*, ATLAS Internal Note, INDET-NO-030 UM-P-93/103, 1993.

[9] ATLAS Collaboration, *ATLAS Liquid Argon Calorimeter Technical Design Report*, CERN/LHCC/96-41, 1996.

[10] ATLAS Collaboration, *ATLAS Letter of Intent for a General-Purpose pp Experiment at the Large Hadron Collider at CERN*, CERN/LHCC/92-4, 1992.

[11] ATLAS Collaboration, *ATLAS Tile Calorimeter Technical Design Report*, CERN/LHCC/96-42, 1996.

[12] Kleinfelder S.A., Levi M., and Milgrome O., *Test Results of a 90 MHz Integrated Circuit Sixteen Channel Analog Pipeline for SSC Detector Calorimetry*, Nuclear Physics B (Proc. Suppl) 23 A, p. 382, 1991.

[13] ATLAS Collaboration, *ATLAS Calorimeter Performance Technical Design Report*, CERN/LHCC/96-40, 1996.

[14] Chase R.L., *et al.*, *Transmission Line Connections Between Detector and Forntend Electronicsin Liquid Argon Calorimetry*, Nuclear Instruments and Methods in Physics Research A 330 p. 228, 1993.

[15] Collot J., *et al.*, *The LAr Tri-Gain Shaper*, ATLAS Internal Note LArg-No-92, 1992.

[16] Gingrich D.M., *et. al.*, *Performance of a Large Scale Prototype of the ATLAS Accordion Electromagnetic Calorimeter*, Nuclear Instruments and Methods in Physics Research A 364, pp. 290-306, 1995.

[17] Cravero A. and Gianotti F., *Uniformity of Response and Energy Resolution of a Large Scale Prototype of the Barrel Accordion Calorimeter*, ATLAS note CAL-NO-33, 1994.

[18] de La Taille C., *Electronic Noise in LAr Calorimetry*, RD3 Internal Note 45, Unpublished.

[19] Gingrich D.M., *et al.*, *An Analog Pipeline Readout Module for Calorimetry at LHC*, Presented by D.M. Gingrich at the Fourth Annual Conference on Electronics for Future Colliders, May 11-12, 1994, LeCroy Corporation.

[20] Kayal P., *Tests of a Switched Capacitor Array for the ATLAS Calorimeter*, University of Alberta MSc. Thesis (1996) pp. 131-133.

[21] Fortney, Lloyd R., *Priniples of Electronics: Analog and Digital*, Harcourt Brace Jonanovich Publishers, 1987.

[22] Fernow Richard C., *Introduction to Experimental Particle Physics*, Cambridge University Press, 1986.

[23] Horowitz P. and Hill W., The Art of Electronics: 2nd Ed., Cambridge University Press, 1994.

[24] Auge E., *et al*, *Analysis of Test Beam Data Taken With the OSAM Readout System*, ATLAS Internal Note, LARG-NO-82, 1997.

Appendix A

Description of Data Recorded

The following tables describe the data (including run-time parameters) used in the analysis contained in this thesis.

Run	*Gain*	*Clocks*	*Readout Time* (μs)	*Trigger Delay* (*ns*)	*Reference Subtraction*
32621	High	Off	4	600	Yes
32874	High	Off	4	600	Yes
32902	High	Off	4	600	Yes
32623	Low	Off	4	600	Yes
32876	Low	Off	4	600	Yes
32922	Low	Off	4	600	Yes
32641	High	Off	2	600	Yes
32667	High	Off	2	600	Yes
32670	Low	Off	2	600	Yes
32689	High	Off	4	575	Yes
32705	High	Off	4	575	Yes
32730	High	Off	4	575	Yes
32733	High	Off	4	575	Yes
32742	High	Off	4	575	Yes
32690	Low	Off	4	575	Yes
32706	Low	Off	4	575	Yes
32731	Low	Off	4	575	Yes
32743	Low	Off	4	575	Yes
32697	High	On	4	575	Yes
32698	Low	On	4	575	Yes
32760	High	Off	4	575	No
32883	High	Off	4	575	No
32880	Low	Off	4	575	No

Table A.1: Summary of conditions for noise data taken with bi-gain shapers.

Run	*Clocks*	*Readout Time* (μs)	*Trigger Delay* (*ns*)	*Reference Subtraction*
32787	Off	8	575	Yes
32810	Off	8	575	Yes
32826	Off	8	575	Yes
32845	Off	8	575	Yes

Table A.2: Summary of conditions for noise data taken with mono-gain shapers.

Run	*Gain*	*Clocks*	*Trigger Delay (ns)*	*Reference Subtraction*	*Maximum Setting (1000 DAC Units)*
32687	High	Off	575	Yes	10
32695	High	On	575	Yes	10
32725	Auto	Off	575	Yes	65
32726	Low	Off	575	Yes	65
32728	High	Off	575	Yes	10
32738	High	Off	575	Yes	10
32739	Low	Off	575	Yes	65
32740	Auto	Off	575	Yes	65
32764	High	Off	575	No	10
32765	Auto	Off	575	No	65
32861	Auto	Off	600	Yes	65
32869	Low	Off	600	Yes	65
32870	High	Off	600	Yes	10
32884	High	Off	575	No	10
32885	Low	Off	575	No	65
32886	Auto	Off	575	No	65
32909	Auto	Off	600	Yes	65
32911	Low	Off	600	Yes	65
32912	High	Off	600	Yes	10
32924	Auto	Off	600	Yes	65

Table A.3: Summary of conditions for calibration data taken with bi-gain shapers.

Run	*Clocks*	*Readout Time (μs)*	*Trigger Delay (ns)*	*Reference Subtraction*	*Maximum Setting (1000 DAC Units)*
32785	Off	8	575	Yes	32
32809	Off	8	575	Yes	32
32816	Off	8	575	Yes	32
32836	Off	8	575	Yes	32

Table A.4: Summary of conditions for calibration data taken with mono-gain shapers.

Run	*Gain*	*Clocks*	*Readout Time* (μs)	*Trigger Delay* (*ns*)	*Reference Subtraction*	Energy (GeV)
32668	High	Off	2	600	Yes	200
32684	Auto	Off	4	575	Yes	200
32685	high	Off	4	575	Yes	200
32686	Low	Off	4	575	Yes	200
32692	Auto	On	4	575	Yes	200
32693	High	On	4	575	Yes	200
32694	Low	On	4	575	Yes	200
32699	Auto	Off	4	575	Yes	200
32702	Auto	Off	4	575	Yes	100
32703	Auto	Off	4	575	Yes	100
32704	Low	Off	4	575	Yes	100
32720	Auto	Off	4	575	Yes	50
32722	Low	Off	4	575	Yes	50
32723	Auto	Off	4	575	Yes	50
32734	Auto	Off	4	575	Yes	150
32735	Low	Off	4	575	Yes	150
32736	Auto	Off	4	575	Yes	150
32737	Low	Off	4	575	Yes	150
32744	Low	Off	4	575	Yes	100
32745	Auto	Off	4	575	Yes	200
32761	Auto	Off	4	575	No	200
32762	Auto	Off	4	575	No	200
32857	Auto	Off	4	575	Yes	200
32859	Auto	Off	4	600	Yes	200
32906	Auto	Off	4	600	Yes	300
32907	Low	Off	4	600	Yes	300
32908	Low	Off	4	600	Yes	300
32925	Auto	Off	4	600	Yes	300

Table A.5: Summary of conditions for electron data taken with bi-gain shapers.

Run	*Clocks*	*Readout Time* (μs)	*Trigger Delay* (*ns*)	*Reference Subtraction*	Energy (GeV)
32782	Off	8	575	Yes	200
32829	Off	8	575	Yes	150

Table A.6: Summary of conditions for electron data taken with mono-gain shapers.

Appendix B

Amplitude and RMS Values

Table B.1 contains the mean amplitudes (averaged over events), RMS noise, and coherent noise for both high and low gain systems. The corresponding data with the reference subtraction circuit disabled is contained in Table B.2. The mono-gain data can be found in Table B.3.

Run	*Gain*	*Mean Amplitude (ADC counts)*	*RMS (ADC counts)*	*Mean Coherent Noise (ADC counts)*
32621	High	2550 ± 50	3.5 ± 0.3	0.6 ± 0.1
32689	High	2550 ± 40	3.4 ± 0.3	0.6 ± 0.1
32705	High	2550 ± 40	3.4 ± 0.3	0.6 ± 0.1
32730	High	2550 ± 40	3.4 ± 0.3	0.6 ± 0.1
32733	High	2550 ± 40	3.4 ± 0.3	0.5 ± 0.1
32742	High	2550 ± 40	3.4 ± 0.3	0.6 ± 0.1
32874	High	2550 ± 40	3.4 ± 0.3	0.6 ± 0.1
32902	High	2550 ± 40	3.3 ± 0.3	0.5 ± 0.1
32623	Low	2570 ± 40	2.9 ± 0.3	0.6 ± 0.2
32690	Low	2570 ± 40	2.9 ± 0.3	0.6 ± 0.2
32706	Low	2570 ± 40	3.0 ± 0.3	0.6 ± 0.2
32731	Low	2570 ± 30	3.0 ± 0.3	0.6 ± 0.2
32743	Low	2570 ± 40	2.9 ± 0.3	0.6 ± 0.2
32876	Low	2570 ± 30	2.9 ± 0.3	0.5 ± 0.2
32922	Low	2570 ± 40	2.9 ± 0.3	0.6 ± 0.2

Table B.1: Summary of results from baseline runs (coherent noise is over system).

Run	*Gain*	*Mean Pedestal (ADC counts)*	*Mean RMS (ADC counts)*	*Mean Coherent Noise (system) (ADC counts)*
32760	High	2390 ± 50	2.9 ± 0.3	0.6 ± 0.2
32883	High	2390 ± 50	2.9 ± 0.3	0.6 ± 0.2
32880	Low	2390 ± 40	2.4 ± 0.3	0.8 ± 0.2

Table B.2: Summary of results from runs with the reference subtraction circuit disabled (after bad events cut).

Run	*Mean Pedestal (ADC counts)*	*Mean RMS (ADC counts)*	*Mean Coherent Noise (ADC counts)*
32787	2560 ± 40	4.0 ± 0.4	0.8 ± 0.1
32810	2560 ± 40	4.0 ± 0.4	0.8 ± 0.1
32826	2560 ± 40	4.0 ± 0.4	0.8 ± 0.1
32845	2560 ± 40	4.0 ± 0.4	0.8 ± 0.1

Table B.3: Summary of results from runs without reference subtraction circuit (after bad events cut).

Appendix C

Pulser Pattern Description

There were two different calorimeter cell-to-channel mappings used, one for the bi-gain shapers and another for the mono-gain shapers (Figures C.1 and C.2). The patterns for these mappings were also different and described below.

For the bi-gain shapers, the calorimeter cells were pulsed such that two neighboring cells (in ϕ) were pulsed simultaneously, as shown in Figure C.3. The pulsing was also performed such that some cells in the first and second layer, occupying the same η-ϕ coordinates, were pulsed simultaneously. This allowed a comparison to be made between the layers for a cross-talk study. There was no expected crosstalk between the second and third layers and so no special pattern was designed for similar studies. There were 12 pulse patterns where between 2 and 8 cells were pulsed.

The pulsing for the mono-gain mapped region of the calorimeter was done in a much less complicated manner (Figure C.4). There were only four patterns used. Columns in η were pulsed simultaneously. For the first two layers (front and middle) every other column on the left side was pulsed while the right side was not pulsed at all. The right side was then pulsed in the same fashion. The exact same pattern was pulsed simultaneously in the middle layer. For the back layer, every other column was pulsed per pattern.

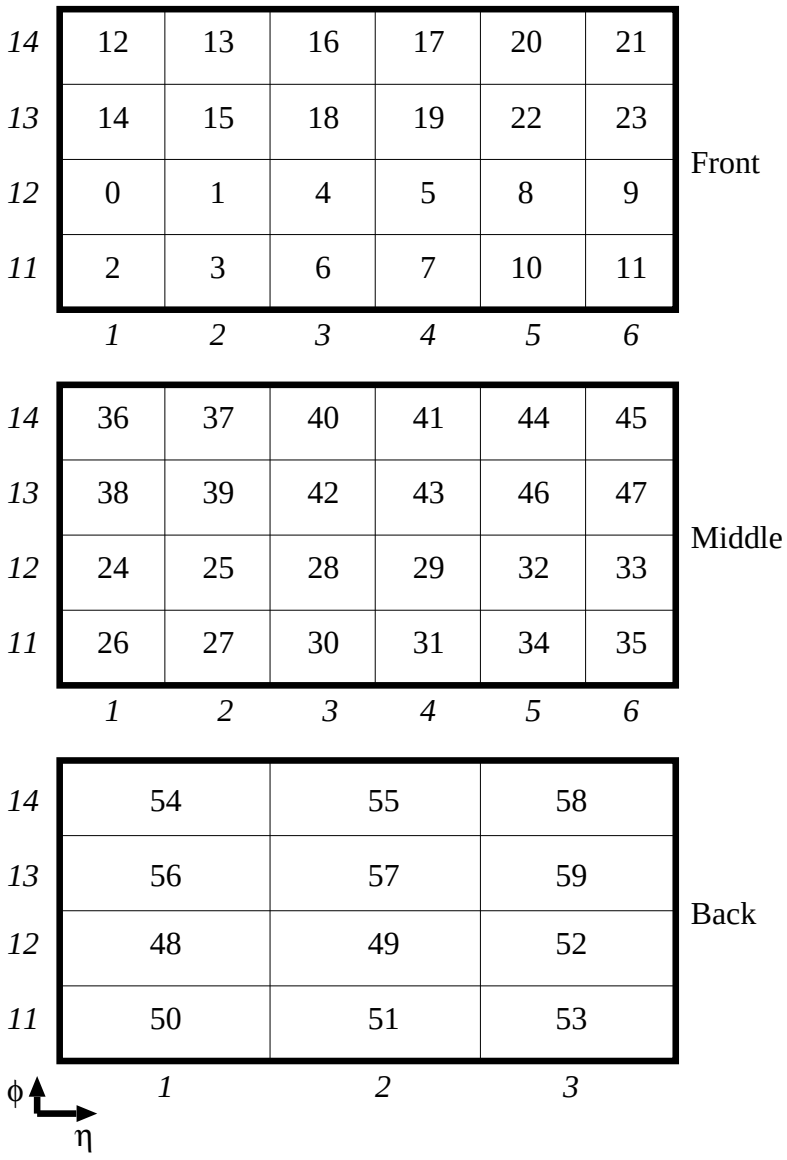

Figure C.1: Channel-to-calorimeter cell mapping for bi-gain shapers. The number at each η-ϕ location is the channel number. The η and ϕ are in arbitrary integer units.

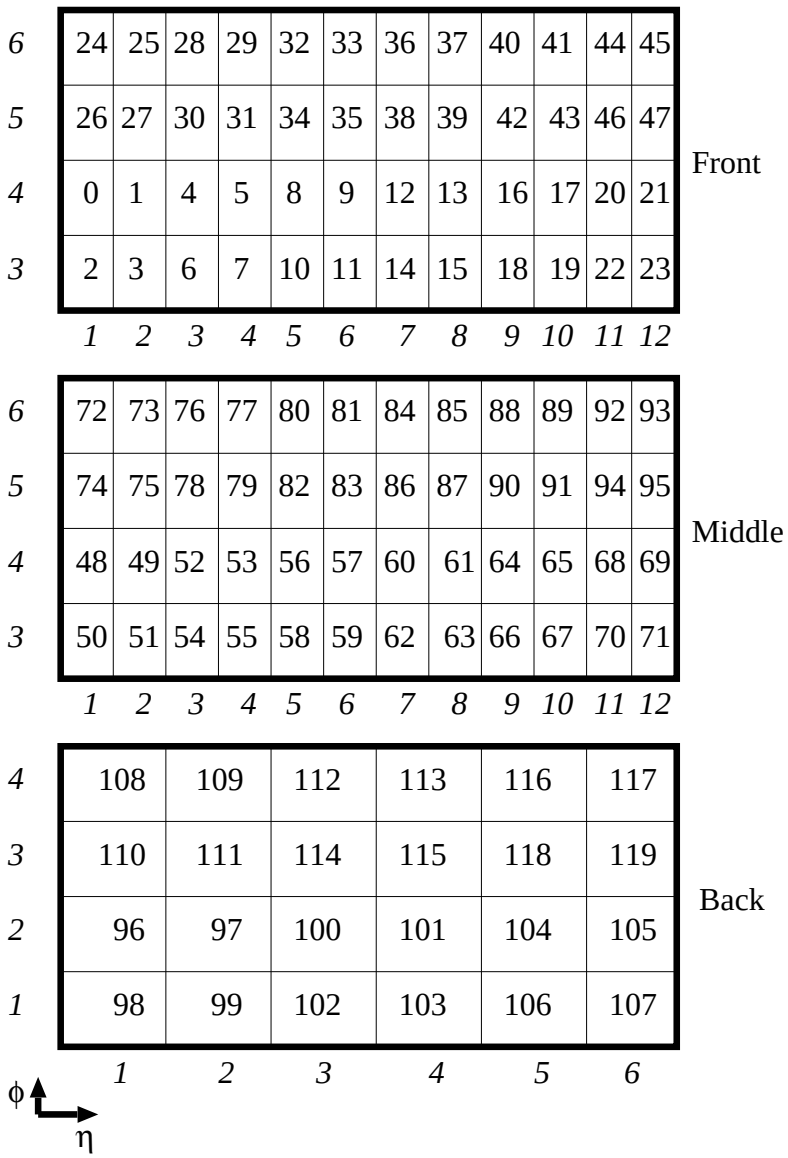

Figure C.2: Channel-to-calorimeter cell mapping for mono-gain shapers.

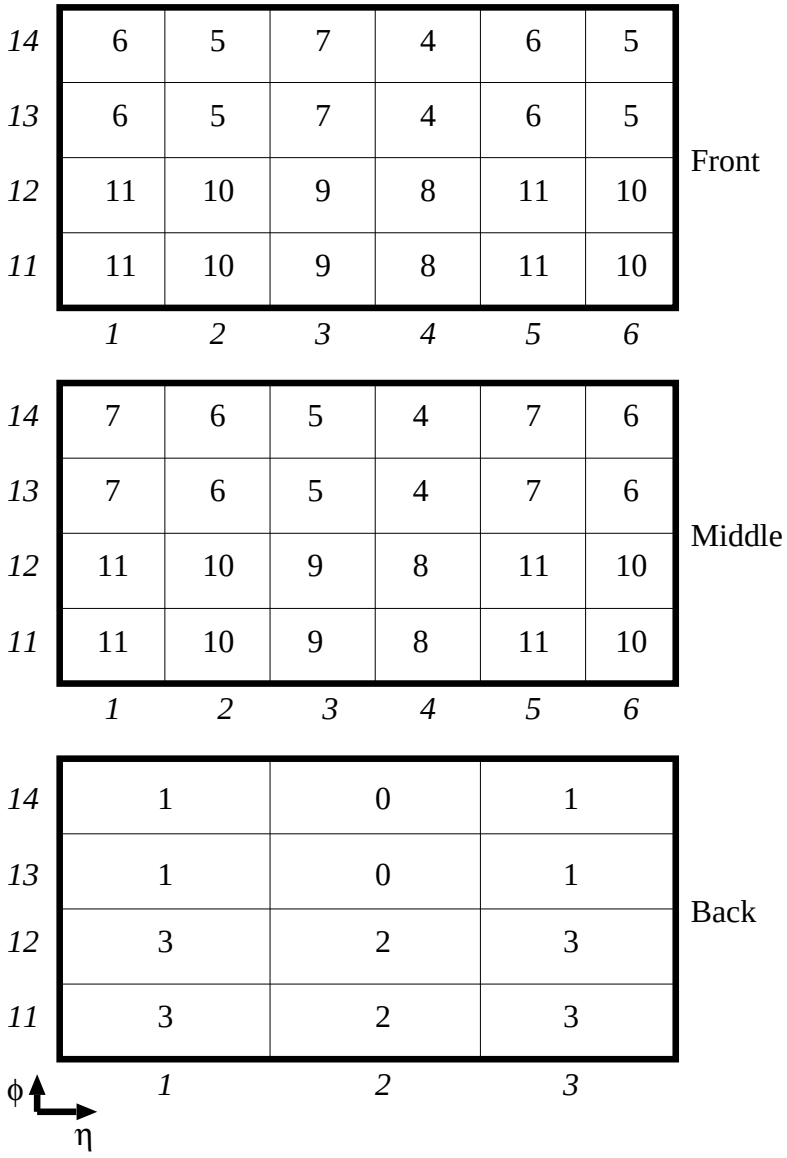

Figure C.3: Calibration pulsing pattern used for bi-gain shapers. The number at each η-*phi* location is the time ordered channel pattern which was pulsed. For example, the first pattern (0) pulsed the cells located at $\eta = 0$ and $\phi = 13$ and $\phi = 14$.

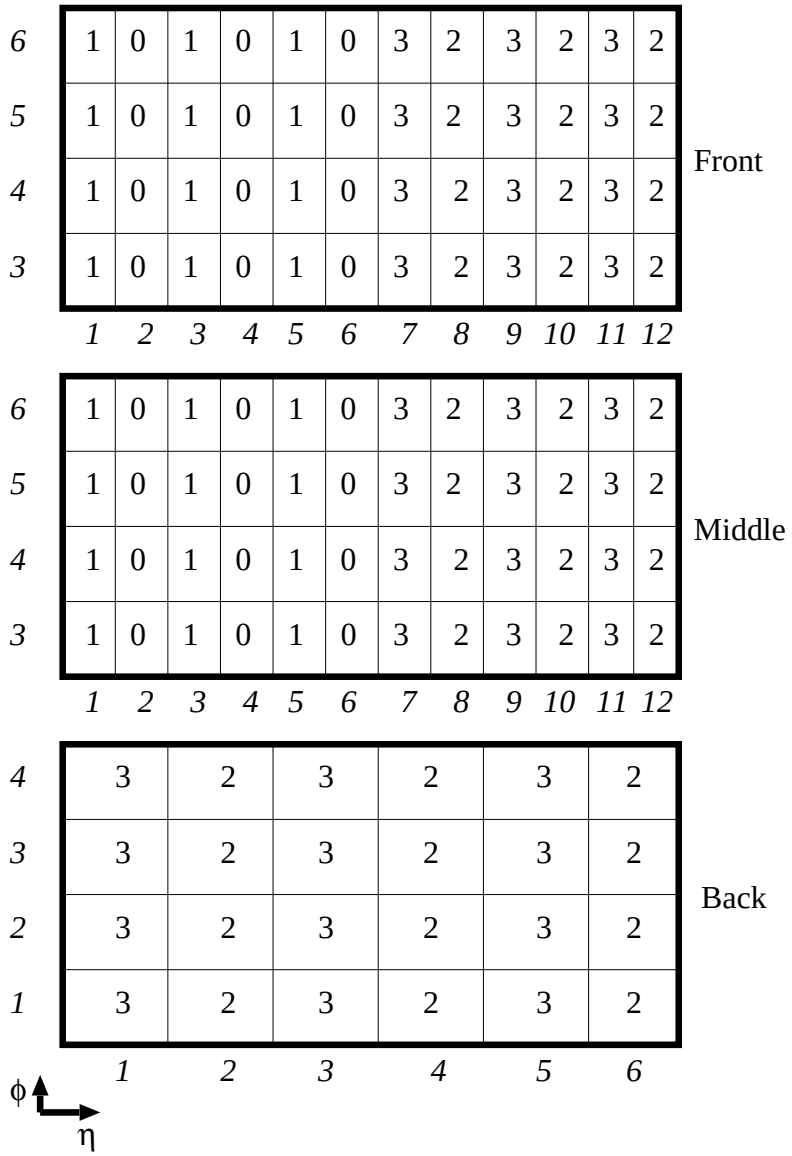

Figure C.4: Calibration pulsing pattern for mono-gain shapers.

Appendix D

Relative Crosstalk Amplitudes

Tables D.1, D.2, and D.3 contain the cross-talk amplitudes for three calibration pulse patterns (0, 5, and 10). The pulsed cells have amplitudes of greater than 6 V. Tables D.4, D.5, D.6, and D.7 contain the corresponding amplitudes for the data when the reference subtraction circuit was disabled.

$\phi\backslash\eta$	*1*	*2*	*3*	*4*	*5*	*6*
14	-0.0172	-0.0189	-0.0128	-0.0275	-0.0154	-0.0197
13	-0.0183	-0.0209	-0.0126	-0.0341	0.0167	-0.0198
12	-0.0080	-0.0078	-0.0081	-0.0098	-0.0074	-0.0077
11	-0.0099	-0.0077	-0.0086	-0.0081	-0.0072	-0.0057
Front Layer						
14	-0.0054	-0.0000	0.0479	0.0482	-0.0254	-0.0125
13	-0.0069	-0.0082	0.0463	0.0507	-0.0159	-0.0173
12	-0.0028	-0.0033	-0.0007	-0.0010	-0.0005	-0.0027
11	-0.0012	-0.0035	-0.0027	-0.0017	0.0010	-0.0005
Middle Layer						
14	-0.1119		6.9631		-0.1767	
13	-0.1482		7.1014		-0.1477	
12	-0.0144		-0.0303		-0.0192	
11	-0.0134		-0.0297		-0.0171	
Back Layer						

Table D.1: Cross-talk (volts) in η and ϕ for the bi-gain shapers. Channels 55 ($\eta = 2$,$\phi = 14$) and 57 (2,13) in the back were pulsed (pattern 0).

$\phi\backslash\eta$	*1*	*2*	*3*	*4*	*5*	*6*
14	-0.1194	6.8913	0.1091	-0.1934	-0.1110	7.5942
13	-0.0238	7.1947	0.0529	-0.2065	-0.1385	7.5440
12	-0.0150	-0.0207	-0.0296	-0.0367	-0.0129	-0.0180
11	-0.0198	-0.0192	-0.0260	-0.0331	-0.0141	-0.0175
Front Layer						
14	-0.0672	0.1245	7.7163	-0.0257	-0.1085	0.1095
13	-0.1002	0.1374	6.8224	0.1066	-0.0632	0.0853
12	-0.0076	-0.0147	-0.0178	-0.0308	-0.0121	-0.0161
11	0.0028	-0.0089	-0.0104	-0.0266	-0.0042	-0.0022
Middle Layer						
14	0.0169		0.0684		0.0132	
13	-0.0204		0.0711		-0.0263	
12	-0.0258		-0.0174		-0.0305	
11	0.0071		0.0015		0.0042	
Back Layer						

Table D.2: Cross-talk (volts) in η and ϕ for the bi-gain shapers. Channels 13 (2,14), 15 (2,13), 21 (6,14), 23 (6,13) in the front, and 40 (3,14), and 42(3,13) in the middle were pulsed (pattern 5).

$\phi\backslash\eta$	*1*	*2*	*3*	*4*	*5*	*6*
14	-0.0298	-0.0210	-0.0371	-0.0168	-0.0248	-0.0190
13	-0.0302	-0.0223	-0.0406	-0.0282	-0.0347	-0.0267
12	-0.1667	7.7594	-0.1765	-0.2429	-0.1703	7.7927
11	-0.1899	7.2417	-0.1684	-0.2370	-0.2368	7.4077
Front Layer						
14	-0.0254	-0.0205	-0.0121	-0.0079	-0.0264	-0.0166
13	-0.0259	-0.0199	-0.0091	-0.0079	-0.0268	-0.0198
12	-0.1155	7.4710	0.0954	-0.1749	-0.1375	7.1774
11	-0.1233	7.3996	0.0855	-0.1849	-0.1479	7.5428
Middle Layer						
14	-0.0015		- 0.0015		-0.0010	
13	-0.0013		- 0.0053		-0.0032	
12	0.0670		0.0069		0.0697	
11	0.0629		0.0030		0.0618	
Back Layer						

Table D.3: Cross-talk (volts) in η and ϕ for the bi-gain shapers. Channels 1 (2,12), 3 (2,11), 9 (6,12), 11 (6,11) in the front, and 25 (2,12), 27 (2,11), 33 (6,12), and 35 (6,11) were pulsed (pattern 10).

$\phi\backslash\eta$	*1*	*2*	*3*	*4*	*5*	*6*
14	0.003	0.003	0.003	0.003	0.003	0.003
13	0.003	0.003	0.003	0.003	0.003	0.004
12	0.002	0.002	0.002	0.003	0.003	0.003
11	0.002	0.002	0.002	0.003	0.003	0.004
Front Layer						
14	0.003	0.003	0.003	0.003	0.003	0.003
13	0.003	0.003	0.003	0.003	0.003	0.004
12	0.003	0.003	0.003	0.002	0.003	0.003
11	0.002	0.002	0.003	0.003	0.003	0.004
Middle Layer						
14	0.003		0.003		0.003	
13	0.003		0.003		0.004	
12	0.003		0.003		0.003	
11	0.003		0.003		0.003	
Back Layer						

Table D.4: Average RMS noise (volts) in η and ϕ for the bi-gain shapers and reference subtraction circuit disabled.

$\phi\backslash\eta$	*1*	*2*	*3*	*4*	*5*	*6*
14	-0.0165	-0.0158	-0.0110	-0.0207	-0.0130	-0.0168
13	-0.0181	-0.0182	-0.0147	-0.0260	0.0170	-0.0200
12	-0.0081	-0.0080	-0.0077	-0.0088	-0.0064	-0.0089
11	-0.0115	-0.0089	-0.0107	-0.0100	-0.0088	-0.0085
Front Layer						
14	-0.0130	-0.0120	0.0589	0.0399	-0.0309	-0.0132
13	-0.0102	-0.0114	0.0611	0.0690	-0.0044	0.0004
12	-0.0020	-0.0022	-0.0018	-0.0071	-0.0049	-0.0063
11	-0.0048	-0.0040	-0.0047	-0.0107	0.0083	-0.0038
Middle Layer						
14	-0.1955		7.0548		-0.2096	
13	-0.1959		7.1390		-0.1742	
12	-0.0269		-0.0443		-0.0307	
11	-0.0253		-0.0451		-0.0367	
Back Layer						

Table D.5: Cross-talk (volts) in η and ϕ for the bi-gain shapers and reference subtraction circuit disabled. Channels 55 ($\eta = 2, \phi = 14$) and 57 (2,13) in the back were pulsed (pattern 0).

$\phi\backslash\eta$	*1*	*2*	*3*	*4*	*5*	*6*
14	0.0941	6.5941	0.0954	-0.1188	0.0953	7.0214
13	0.1258	6.8422	0.0972	0.0672	0.1418	6.9015
12	-0.0221	-0.0227	-0.0245	-0.0298	-0.0166	-0.0238
11	-0.0189	-0.0184	-0.0216	-0.0270	-0.0139	-0.0167
Front Layer						
14	-0.0790	0.0353	6.7674	0.1397	-0.0878	0.0426
13	-0.1105	0.1143	5.9144	0.0996	-0.0599	0.0971
12	-0.0121	-0.0153	-0.0194	-0.0264	-0.0001	-0.0139
11	-0.0165	-0.0127	-0.0169	-0.0246	-0.0060	-0.0139
Middle Layer						
14	-0.0207		0.0566		-0.0100	
13	0.0007		0.0686		-0.0194	
12	-0.0498		-0.0319		-0.0527	
11	-0.0412		-0.0261		-0.0493	
Back Layer						

Table D.6: Cross-talk (volts) in η and ϕ for the bi-gain shapers and reference subtraction circuit disabled. Channels 13 (2,14), 15 (2,13), 21 (6,14), 23 (6,13) in the front, and 40 (3,14), and 42(3,13) in the middle were pulsed (pattern 5).

$\phi\backslash\eta$	*1*	*2*	*3*	*4*	*5*	*6*
14	-0.0223	-0.0160	-0.0256	-0.0145	-0.0195	-0.0149
13	-0.0244	-0.0170	-0.0305	-0.0237	-0.0283	-0.0235
12	0.1155	7.1838	0.1233	-0.1583	0.1269	7.2905
11	0.1421	6.3363	0.1078	-0.1662	0.1729	6.2813
Front Layer						
14	-0.0224	-0.0188	-0.0139	-0.0119	-0.0268	-0.0204
13	-0.0237	-0.0205	-0.0133	-0.0108	-0.0275	-0.0211
12	0.1043	6.6641	0.1066	-0.1692	0.1065	6.4770
11	0.1169	6.5551	0.0865	-0.1702	0.1241	6.8705
Middle Layer						
14	-0.0001		- 0.0002		-0.0023	
13	0.0005		- 0.0017		0.0055	
12	0.0563		0.0051		0.0673	
11	0.0563		0.0043		0.0670	
Back Layer						

Table D.7: Cross-talk (volts) in η and ϕ for the bi-gain shapers and the reference subtraction circuit disabled. Channels 1 (2,12), 3 (2,11), 9 (6,12), 11 (6,11) in the front, and 25 (2,12), 27 (2,11), 33 (6,12), and 35 (6,11) were pulsed (pattern 10).